UNIVERSITY OF TURKU

# Effect of laser beam angle of incidence on surface roughness and porosity of IN718 parts manufactured via laser powder bed fusion

Materials Engineering/Faculty of Technology
Master's thesis
Department of Mechanical and Materials Engineering

Author:
Einari Tolvanen

Supervisors:
Adjunct Professor Heidi Piili, D.Sc. (Tech.)
RDI Specialist Jarno Välikangas, M.Sc.

27.10.2024
Turku

Master's thesis

**Subject**: Materials Engineering
**Author**: Einari Tolvanen
**Title**: Effect of laser beam angle of incidence on surface roughness and porosity of IN718 parts manufactured via laser powder bed fusion
**Supervisors**: Adjunct Professor Heidi Piili, D.Sc. (Tech.), RDI Specialist Jarno Välikangas, M.Sc.
**Advisors:** Mohsen Amraei, D.Sc., Hannu Heikkinen, M.Sc.
**Number of pages**: 96 pages
**Date**: 27.10.2024

Laser powder bed fusion of metal (PBF-LB/M) is a rapidly evolving digital manufacturing technology paving the way for a new industrial revolution. It has attracted attention in industry and academia thanks to its ability to produce complex geometries, while maintaining cost-efficiency in low-volume production. The utilization of laser beam in layer-by-layer fusion of metal powder induces certain challenges related to the quality of the manufactured components. In recent years, researchers have reported variations in defect formation depending on the location of the manufactured components on the build platform. Several explanations have been provided for these variations, one of which is the laser beam angle of incidence (*LBAI*), which varies across the build platform.

The aim of this thesis is to investigate the effect of *LBAI* on surface roughness and porosity of Inconel 718 (IN718) parts manufactured via PBF-LB/M. The proposed part characterization methodology can be used as a benchmark in process development that aims to mitigate the formation of the studied defects. Experiments were conducted by characterizing the laser beam and by fabricating different geometries at different build platform locations. Surface roughness and porosity was analyzed from the fabricated test parts.

Results in the current work indicate that the laser beam spot is prone to elongation when the *LBAI* is increased, which can lead to loss of energy density at the spot periphery. Surface roughness characterization demonstrated that the effect of *LBAI* depends on the surface orientation in relation to the laser beam incidence. Based on the findings, it is anticipated that the laser beam that is aligned parallel to the fabricated surface yields the most optimal surface roughness. Porosity characterization showed that the effect of *LBAI* is negligible when using parameters that are optimized to yield fully dense parts. On the contrary, parameters that yielded lack of fusion showed distinct increase in porosity when *LBAI* was increased. Additionally, opportunities for future research were identified, which includes the effect of laser beam scanning strategy and the effect of inert gas flow conditions across the powder bed.

**Keywords**: Laser powder bed fusion, direct metal laser sintering, selective laser melting, additive manufacturing, Inconel 718, 3D printing, angle of incidence, surface roughness, lack of fusion, porosity

## Acknowledgements

I would like to express my deepest gratitude to all the people who have supported me in this endeavor and made it possible. Many thanks to Tatu Syvänen, Hannu Heikkinen and Jarno Välikangas from EOS Finland Oy for offering me this interesting research topic and for guiding me through the project. Special thanks to all the other AMazing people from EOS Finland Oy and EOS GmbH who have helped me along the way. I am profoundly grateful for Heidi Piili and Mohsen Amraei from University of Turku for their invaluable support and insightful feedback throughout the thesis. Their expertise and encouragement were essential during the writing of this thesis. Last but certainly not least, I want to thank my family and friends for their unwavering support during the last two intense years of my studies.

# Table of contents

## Nomenclature

| **Abbreviation** | **Explanation** |
|---|---|
| AlSi10Mg | Aluminum alloy |
| AM | Additive manufacturing |
| AMed | Additively manufactured |
| *BPP* | Beam parameter product |
| DSAC | Downskin facing away from the center of build platform |
| DSTC | Downskin facing towards the center of build platform |
| IN718 | Inconel 718, nickel-chromium alloy |
| *LBAI* | Laser beam angle of incidence |
| LDS | Laser diagnostic software |
| LOF | Lack of fusion |
| PBF-LB/M | Powder bed fusion of metal with a laser beam |
| PBF-EB/M | Powder bed fusion of metal with an electron beam |
| SFM | Scan field monitor |
| Ti6Al4V | Titanium alloy |
| USAC | Upskin facing away from the center of build platform |
| USTC | Upskin facing towards the center of build platform |
| VAC | Vertical surface facing away from the center of build platform |
| *VED* | Volumetric energy density (J/mm$^3$) |
| VTC | Vertical surface facing towards the center of build platform |
| 316L | Stainless steel grade |
| **Symbol** | **Explanation** |
| θ | Laser beam angle of incidence (°) |
| θ’ | Scanning mirror rotation angle (°) |
| *f* | Effective focal length (mm) |
| $W_0$ | Beam radius at beam waist (µm) |
| δ | Half angle of beam divergence (°) |
| λ | Wavelength (nm) |

| | |
|---|---|
| $Sa$ | Arithmetical mean height of a surface (µm) |
| $Ra$ | Arithmetical mean height of a profile (µm) |
| α | Build angle (°) |
| $d_\theta$ | Diameter of elongated beam spot (µm) |
| $d$ | Diameter of laser beam (µm) |
| ζ | Surface laser relation angle (°) |
| $o$ | Beam offset from optical axis at the protective window |
| $r$ | Radial distance of beam spot from the optical axis at the surface of the powder bed |
| $L$ | Distance from powder bed surface to the protective window |
| $d_e$ | Deviation of laser beam from being parallel with the part surface |

# 1 Introduction

Laser powder bed fusion (PBF-LB/M) is among the most used additive manufacturing technologies of metal materials [1]. PBF-LB/M involves fusing subsequent layers of metal powder together with a laser beam to form a solid object. The technology has proved its usefulness in many industries such as aerospace [2], biomedical [3] and automotive industry [4]. The key elements of PBF-LB/M which make it so successful in many applications include the increased design freedom, more economical production of small batches and unique components and shorter lead times of production [5].

## 1.1 Background and motivation

While PBF-LB/M offers many possibilities, it also comes with certain limitations. Components manufactured via PBF-LB/M have relatively high surface roughness [6] and lower dimensional accuracy [7] compared to traditional manufacturing methods such as machining or casting. Voids within the manufactured part, also known as porosity, is yet another challenge posed by PBF-LB/M [8]. These defects present in parts manufactured via PBF-LB/M can limit the utilization of the technology in critical components which require high quality [9]. In recent years, it has been noted that within the same PBF-LB/M process there may be variations in the number of defects, depending on the location of the manufactured part on the build platform [10]. Several location dependent factors within the PBF-LB/M process have been studied to cause variations in the part properties. For example, Chen. et al. [11] concluded, that the recoating causes some segregation of powder particles, leading to variation of surface roughness across the recoating motion axis. As the PBF-LB/M process takes place in an inert gas atmosphere to prevent unwanted chemical reactions, the uneven gas flow velocities across the powder bed can contribute to variations in the part quality as well [12]. One of the factors affecting the location dependent part properties is the laser beam angle of incidence (*LBAI*). A few studies have shown that increased *LBAI* can have negative effects on the resulting defects, such as surface roughness [6] [10] [13] and porosity [14]. The negative effects of increased *LBAI* have been explained due to the changes in projected area of the inclined laser beam [6] [15] [14] and due to melt pool extensions promoted by inclined laser beam [10] [13]. Increased surface roughness has been observed especially for inclined surfaces, which are a necessity for full utilization of the potential of PBF-LB/M [10] [11].

According to the knowledge of the author, comprehensive study about the *LBAI* induced defect formation on inclined surfaces manufactured from IN718 is yet to be conducted. Thus, *LBAI* induced defect formation for inclined surfaces manufactured via PBF-LB/M forms the research problem of this thesis and the thesis aims to fill this research gap in the academic literature. It goes without saying that it is the common interest of AM machine end-users and the machine vendors, that the part properties are uniform across the whole build volume. This enables more efficient utilization of AM machines without compromising the part quality. PBF-LB/M processes could be further optimized to yield parts with uniform quality by understanding the effect of location dependent factors on defect formation such as *LBAI*. Thus, the topic of the thesis is also relevant for the AM industry.

## 1.2 Objectives and research questions

As previously outlined, laser beam angle of incidence is location dependent, and it can have an effect on the properties of parts produced via PBF-LB/M. Thus, the objective of this thesis is firstly to provide insights into how the *LBAI* affects the PBF-LB/M defect formation with IN718 in the used PBF-LB/M system. Additionally, the thesis aims to study what kind of influence part orientation has to the formation of defects when angle of incidence is increased. Better understanding of the phenomena involved could potentially lead to optimized process parameters and better control over the PBF-LB/M process across the whole build area.

To reach the set objectives, the thesis aims to provide answers to the following research questions:

- How does the laser beam angle of incidence affect the size and shape of the laser beam spot?
- How does the laser beam angle of incidence affect part surface roughness and porosity?
- How does the part orientation in relation to the laser beam affect part surface roughness and porosity?
- How does the location of the parts affect the surface roughness?

## 1.3 Methodology and structure of thesis

The thesis consists of literature review and experimental part. The literature review is conducted by compiling relevant information mainly from recent research and review articles, as well as textbooks. The structure of the literature review aims to familiarize the reader with the relevant concepts of PBF-LB/M before proceeding to the state-of-the-art research findings. Essential optical components and the overall structure of a general PBF-LB/M system are initially introduced. Additionally, relevant process parameters of PBF-LB/M are introduced. Defects which are studied in the experimental part and their formation mechanisms are reviewed. Finally, state-of-the-art research findings about the effect of *LBAI* and scanning strategy on the defects is discussed.

In the experimental part the laser beam is characterized with different *LBAI*s to understand how the laser beam is affected by the *LBAI* in the used PBF-LB/M system. Then a set of test parts and print jobs are designed and manufactured via PBF-LB/M from IN718. Test parts are analyzed via optical microscopy and profilometry to capture the defect formation within the parts. Finally, the acquired data is analyzed and the effect of *LBAI* on the test parts is concluded. Identified future research opportunities are proposed to provide guidelines for further studies.

## 1.4 Limitations of the thesis

The thesis focused on the effect of *LBAI* with specific PBF-LB/M material and system. Thus, the effect of *LBAI* may be different with various material/machine configurations. Effect of *LBAI* on laser beam intensity profile remained unexplored due to physical limitations of the available measurement device. Surface roughness and porosity were studied in the thesis, while other important characteristics affecting part performance were excluded due to time constraints. Study mainly focused on 45° and 90° surfaces, hence the conclusions might not apply with different geometries, such as build angles below 45°. Surface roughness was characterized by using arithmetical mean height of a surface *(Sa)*, which does not precisely capture localized features such as peak and valleys and does not account for directional characteristics or textures on the studied surface. Additionally, porosity was studied by analyzing cut section of the samples, which limits the accuracy of porosity analysis as the porosity of whole volume is not analyzed. The used methods yielded adequate overview on the studied phenomena and put out guidelines for further studies despite the limitations.

# 2 Introduction to laser beam and optical system in PBF-LB/M

At the core of a PBF-LB/M machine, are the laser beam and optical system. Laser is light produced via stimulated emission and it has attributes which make it useful in material processing: it is of single wavelength (monochromaticity), waves are in the same phase (coherency) and the resulting beam spreads out very little (low divergence) [16]. Owing to those distinct characteristics, energy within the laser beam is concentrated, which enables precise delivery of high energy input [16]. The optical system guides the beam swiftly across the powder bed to facilitate computer-controlled fusion of the powder. Figure 1 illustrates the schematics of optical system in a PBF-LB/M based on the machine used in the experimental part of the thesis [17].

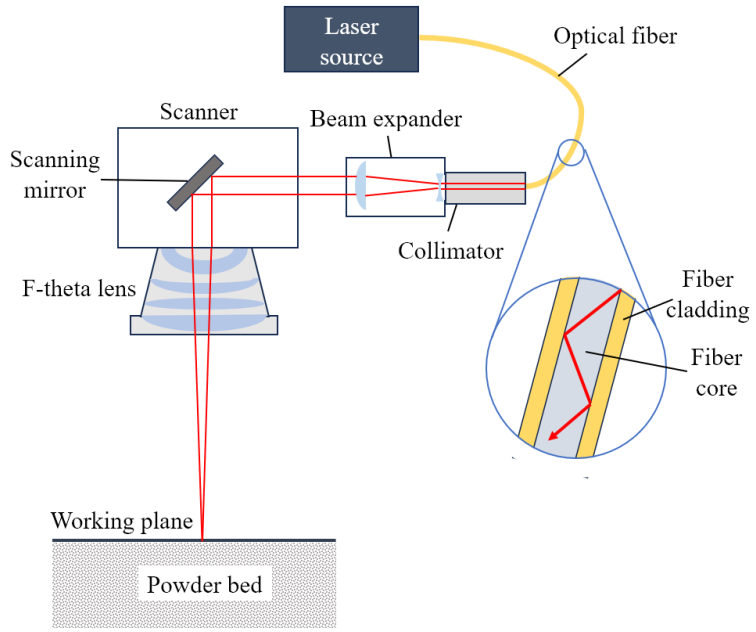


Figure 1 Schematics of optical system within a PBF-LB/M machine. Note: there is only one scanning mirror for illustrative purposes, in reality there are two mirrors in PBF-LB/M optical system. Reproduced from ref [17] and ref [18].

As can be seen from Figure 1, the PBF-LB/M optical system starts from a laser source. There are several types of lasers available, but typically in modern PBF-LB/M systems a fiber laser is used due to their reliability and low maintenance. Fiber laser is a type of solid-state laser, in which the stimulated emission is initiated inside an active optical fiber. When the laser beam has been formed, a transport fiber is used to guide the output laser beam to the other optical components of the system [19]. The transport fiber consists of fiber core which is surrounded by fiber cladding. The fiber core has higher refraction index than the cladding, enabling the

transportation of the laser beam through total internal reflection. Essentially, the beam guided into the fiber core bounces back and forth at the core-cladding interface and eventually traverses through the fiber, as demonstrated in Figure 1. [20]

Laser beam enters the collimator at the end of the fiber, as illustrated in Figure 1. When the beam reaches the end of the fiber it has large divergence, i.e. the beam diameter changes considerably over a certain propagation distance. Thus, the beam needs to be collimated with a beam collimator so that the light propagates in one direction. Beam collimator consists of a focusing lens and it is attached to the end of the fiber directly or with a connector interface. [21] [22] After the beam has been collimated the diameter of the beam is then increased by using a beam expander as shown in Figure 1. Increasing the diameter of the beam is necessary to avoid too high energy density of the beam entering the scanning optics, which could damage the components. Diameter of the focused beam on the powder bed can be adjusted with the beam expander [23].

After passing through the beam expander, the beam enters laser scanner as illustrated in Figure 1. The scanner in PBF-LB/M system controls the movement of the laser beam across the powder bed typically with two galvanometer-operated mirrors. Mirrors can be rotated so that the laser can be deflected in different directions. The other mirror controls the movement of beam in X-direction and the other mirror in Y-direction. The position precision of the scanner is one of the key factors affecting the dimensional accuracy capabilities of a PBF-LB/M system [24].

Scanner is coupled with a F-theta scanning lens, which has several essential functions. First of all, the lens focuses the laser beam into a tiny spot, usually around 70-100 µm in diameter [25] [26]. F-theta lens is a sophisticated system of several lenses, when compared to a regular spherical focusing lens. One of the key features of F-theta lens is the nearly flat focusing field, where the beam is always at focus on the working plane, rather than on a spherical surface [27]. There is always some focusing field distortion present within the lens, which can make the focusing field slightly curved [28]. F-theta lenses in PBF-LB/M systems are typically non-telecentric, which means that the laser beam is directed on the powder bed at an angle in all locations except at the optical center. This enables a larger working area where the laser beam can be scanned but also can lead to non-circular shape of the beam spot at the build platform periphery [27].

Another important aspect of F-theta lens is the near linearity of the beam displacement in relation to the angular displacement of the scanning mirror [29] [28]. Figure 2 illustrates the beam displacement in F-theta scanning lens.

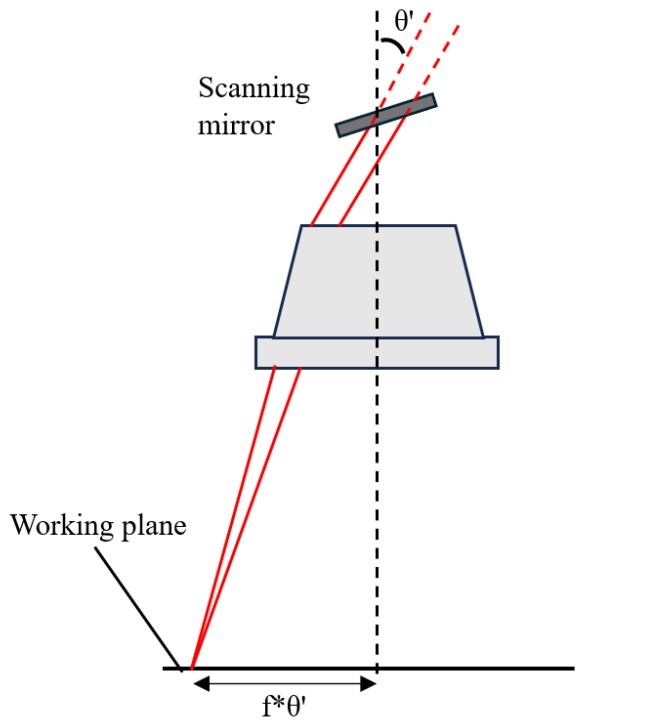


Figure 2 Linear beam displacement in F-theta lens [28].

As can be seen from Figure 2, the approximate beam displacement can be expressed as a product of effective focal length *f* and scanning mirror rotation angle *θ'*. Linear beam displacement reduces image distortion and enables constant scanning speed across the whole working area [28].

# 3 Parameters in PBF-LB/M

There is numerous process parameters involved in PBF-LB/M process, which influence the outcome of the process. Process parameters are often divided into different categories in the literature and the categorization can vary depending on the author [19] [30] [31] [24]. According to Chua et al. [30] PBF-LB/M process parameters are divided into four categories. Table 1 illustrates the categorization proposed by Chua et al [30]. As can be seen from Table 1, process parameters consist of material, laser, scan and environment parameters. In this chapter, certain parameters from laser and scan categories are introduced, as those are most relevant regarding the topic of this thesis. Additionally, concept of volumetric energy density (*VED*) is briefly introduced, as it is often used to describe the complex interplay of multiple process parameters [32] [33].

Table 1 PBF-LB/M process parameter categorization. Reproduced and modified from [30].

| Category | Process parameter |
|---|---|
| **Material** | Composition, powder density, morphology, powder size, distribution, thermal properties, flow properties, melt pool viscosity, material absorptivity |
| **Laser** | Mode, wavelength, power, frequency, pulse width, spot size, focal point position, intensity profile |
| **Scan** | Scan speed, scan pattern, layer thickness, scaling factors, hatch spacing, pulse distance |
| **Environment** | inert gas type, oxygen level, pressure, gas flow velocity, preheating temperature |

## 3.1 Laser parameters

Laser parameters have major effect on laser material interaction, which influences critical factors such as melt pool formation [30]. In this section the following laser parameters are introduced due to their relevance to the current work: laser power, focal point position and spot size and intensity profile. Additionally, beam quality is introduced, which is not included in the categorization by Chua et al. [30] but is considered relevant for the current work.

### 3.1.1 Laser power

Laser power is one of the most critical parameters for successful PBF-LB/M process. It refers to the amount of energy emitted by the laser during laser material interaction. Generally, laser

power is expressed in Watts (W). The role of laser power is crucial as it needs to be high enough to successfully melt the material to form sufficient metallurgical bond between the consecutive layers [16]. On the other hand, too high laser power can lead to excessive melt pool temperature, which can induce process instabilities such as keyholing [8] or spattering [34].

### 3.1.2 Focal point position and spot size

Focal point position in PBF-LB/M refers to the distance between the powder bed surface and the point where the beam converges to its smallest diameter. Thus, focal point position of zero means that the beam is directly focused on the powder bed [35]. Figure 3 illustrates the effect of focal point position on laser beam spot size.

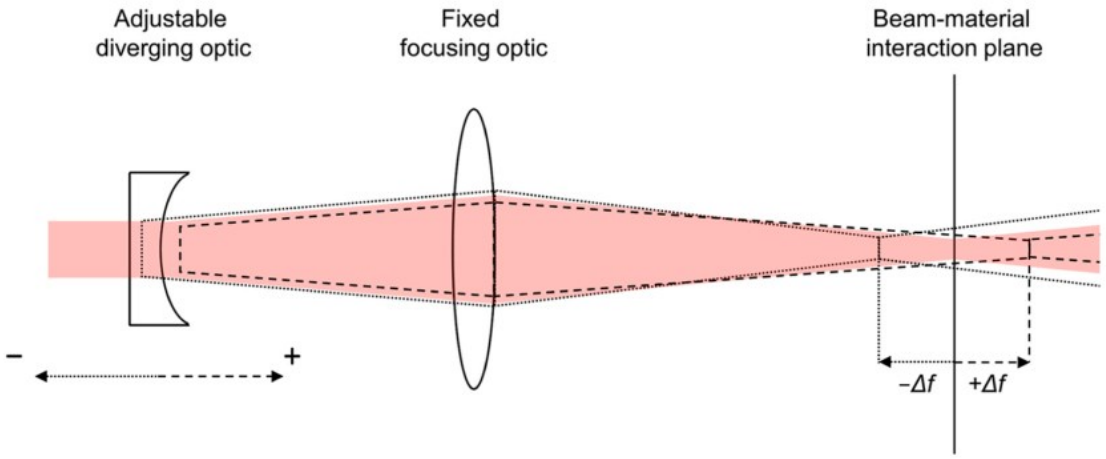


Figure 3 Effect of focal point position on the beam diameter. Red illustrates focal point position of zero, dashed line a positive and dotted line a negative position. Reproduced from [35] which is under an open-access Creative Commons CC BY license.

As can be seen from Figure 3, when the focal point position is increased or decreased the spot size will increase [35]. Increasing the spot size increases the area which the laser beam is heating, thus the energy density (J/mm$^2$) will decrease [36]. Reduction in energy density further decreases the penetration depth of the laser, leading to shallower melt pool [35]. Melt pools can be deeper when the focus position is slightly beneath the surface of processed material, as observed by Vänskä et al. [37] and Reijonen et al. [35]. However, major shift in focus to either direction decreases the melt pool depth due to decreased laser beam penetration. According to Reijonen et al. [35] both negative and positive shifts in the focal point position greater than 1 mm reduced the melt pool depth considerably. In their study, the deepest melt pool depth was acquired with focal point position which was only slightly below

the powder bed surface. Only a small increase in melt pool width was observed when the focal point position was adjusted to either direction within the range of ±5mm.

The focal point position can unintentionally shift during high power laser processing due to thermal lensing within the optical system. Thermal lensing occurs when the transmissive optical components absorb laser emission, which induces changes in the optical propagation properties of the optical system [38]. In research conducted by Goossens et al. [38] it was concluded that thermal lensing induced focus shift during PBF-LB/M of Cu alloy. It was observed that processing of consecutive parts with high laser power (>800W), caused higher porosity in the parts that were scanned last. However, the research on thermal lensing in PBF-LB/M is limited and it has not been concluded how large focus shifts are acceptable in terms of part quality [35].

### 3.1.3 Beam quality

Beam quality is an essential laser parameter that can be defined in different ways. Generally, beam quality is defined as a measure of how well beam can be focused to a small spot [39]. There are two commonly used measures to quantify beam quality: the beam parameter product (*BPP*) and the $M^2$ factor. Figure 4 shows the necessary measures for calculating *BPP*.

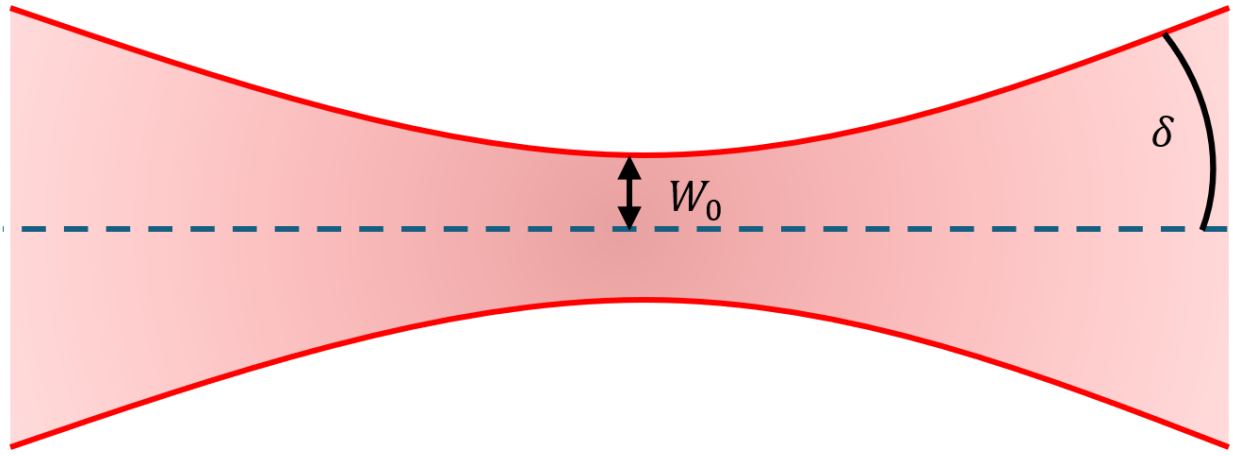


Figure 4 Measures required for calculating *BPP* [40].

As can be seen from Figure 4, $W_0$ is the beam radius measured from the waist of focused beam and $\delta$ is the half angle of beam divergence. By multiplying these values *BPP* can be obtained with equation 1.

$$BPP = W_0 * \delta \quad (1)$$

Higher *BPP* means lower beam quality [40]. $M^2$ value can be derived from *BPP* with equation 2, where λ is the wavelength [9].

$$M^2 = \frac{BPP * \pi}{\lambda} \quad (2)$$

For a Gaussian beam $M^2$ factor of one is the highest possible beam quality and higher value implies lower beam quality [9]. Poor beam quality may cause inability to produce small beam spot. As a result, the energy density of the beam is reduced as the energy is spread to a larger area, which in turn can cause insufficient melting of material [9].

### 3.1.4 Intensity profile of the laser beam

Intensity profile of the laser beam describes how the laser power per unit area is distributed across the beam cross-section. The beam intensity profile can be illustrated with a graph, where the power intensity of the beam in W/cm$^2$ is in the y-axis and beam width (µm) is in x-axis. Figure 5 illustrates three different types of intensity profiles commonly mentioned in the literature [41] [42] [43] [44], which can be utilized in PBF-LB/M: Gaussian, Donut and Flat-top distribution.

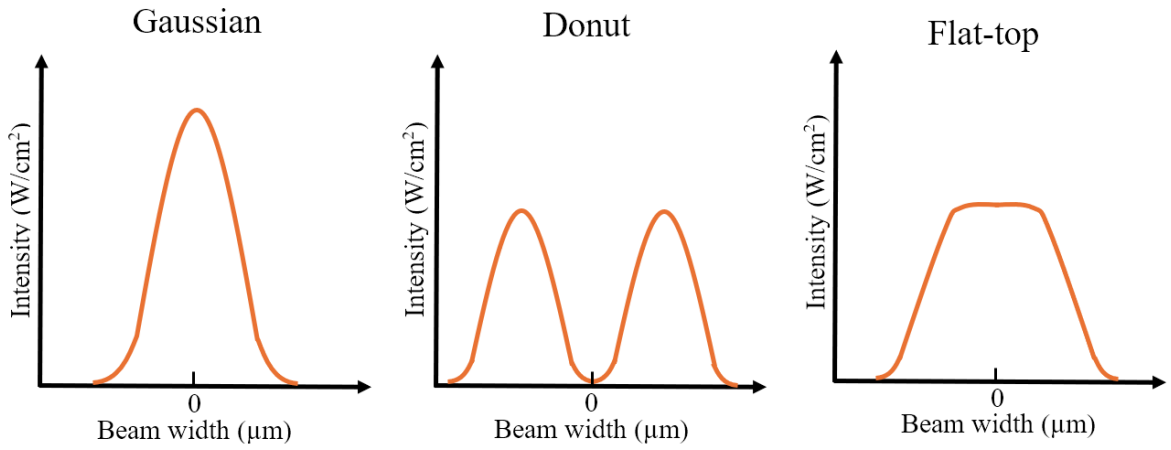


Figure 5 Illustrations of three different intensity profiles based on [41], [42], [43] & [44]. Figures are just for illustrative purposes, thus there are no exact values for variables presented.

As Figure 5 illustrates, the Gaussian beam features a high peak in beam intensity at the middle of the beam (at the beam width of zero), while the intensity decreases gradually towards the edges of the beam. Donut beam has two separate intensity peaks, while there is a reduced intensity in the middle of the beam and the overall beam width is higher compared to

Gaussian beam. Flat-top beam resembles Gaussian beam with flattened top part. This enables more even energy intensity throughout the whole beam.

The most common beam intensity profile in PBF-LB/M is the Gaussian beam [41] [42], where the laser power distribution follows approximately the Gaussian function [42]. Owing to the high beam quality, Gaussian beam has advantages such as high focusability and the potential to achieve small spot size [45]. High intensity peak of Gaussian beam induces certain challenges and sets limitations for the PBF-LB/M process, such as localized overheating in the middle of the melt pool with high laser power. The area which most effectively melts the material is located at the center in Gaussian beam. The intensity at the center of the beam may increase too much and heat the melt pool excessively when the laser power is increased [46]. Overheating can cause vaporization of material which leads to unstable melt pool and spattering [41].

As the demand for higher productivity is increasing in the AM industry, alternative beam profiles have been explored to tackle the challenges posed by the Gaussian beam [41] [42] [43] [44] [45]. Wischeropp et al. [43] demonstrated that by utilizing donut intensity profile, the processing window for AlSi10Mg increased. Stable melt pool and material with density of >99,5% was achieved with wider range of laser power and scanning speed when utilizing donut beam [43]. Wider processing window was also reported by Grünewald et al. [41] with single tracks manufactured from 316L. In both studies it was explained, that by utilizing the donut beam, keyhole formation can be avoided more efficiently, even with higher laser power [43] [41]. Larger area of the donut beam decreases the intensity of the spot, which reduces the likelihood of keyholing. However, donut beam may also lead to insufficient penetration depth with low laser power, as suggested by Grünewald et al. [41].

## 3.2 Scan parameters

Scan parameters determine how laser is scanned along the powder bed surface in each layer to consolidate the part [47]. The most relevant scan parameters for the current work are introduced: scan speed, layer thickness, hatch spacing and scan pattern. It should be noted that the scan parameters are not limited to these four, as Table 1 describes. Figure 6 illustrates scan speed, layer thickness and hatch spacing.

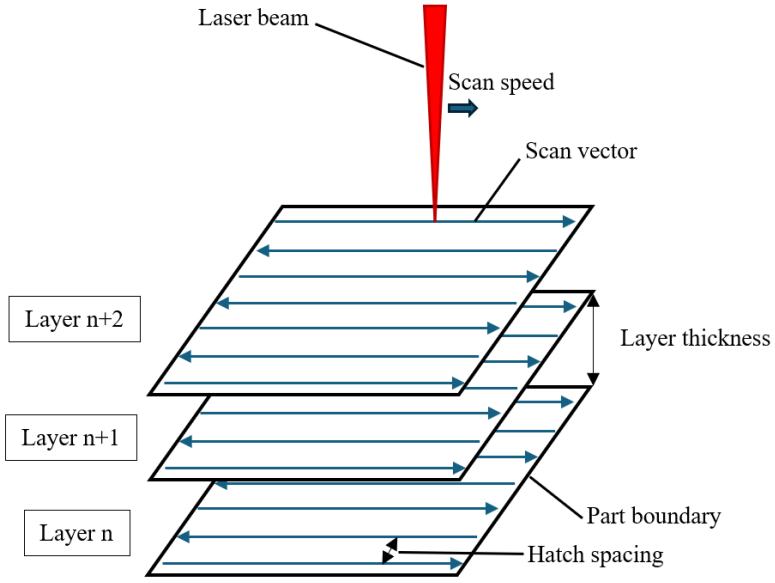


Figure 6 PBF-LB/M scan parameters [47].

As can be seen from Figure 6, scan vectors are fitted within the boundaries of the part in consecutive layers to facilitate the selective fusion of material. Hatch spacing refers to the distance (mm) between adjacent scan vectors, and layer thickness (µm) determines the thickness of powder layer that is melted during scanning of each layer. Scan speed determines the speed (mm/s) at which the beam travels across the powder bed during scanning. The melt pool needs to penetrate to previously solidified layers and adjacent scan tracks should overlap with each other to obtain dense parts. Thus, layer thickness and hatch spacing set requirements for sufficient laser power. Increasing the layer thickness or hatch spacing increases the volume of material which needs to be fused together; thus, the required laser power also increases. For scanning speed and laser power the correlation is similar. When scan speed increases, the interaction time between laser beam and material decreases. Consequently, less energy is absorbed from the laser beam to the powder to facilitate melting which leads to an increase in required laser power. [19] [47]

Scan pattern defines how the scan vectors, are fitted to the cross-section of each layer. Figure 7 illustrates four common types of scanning patterns.

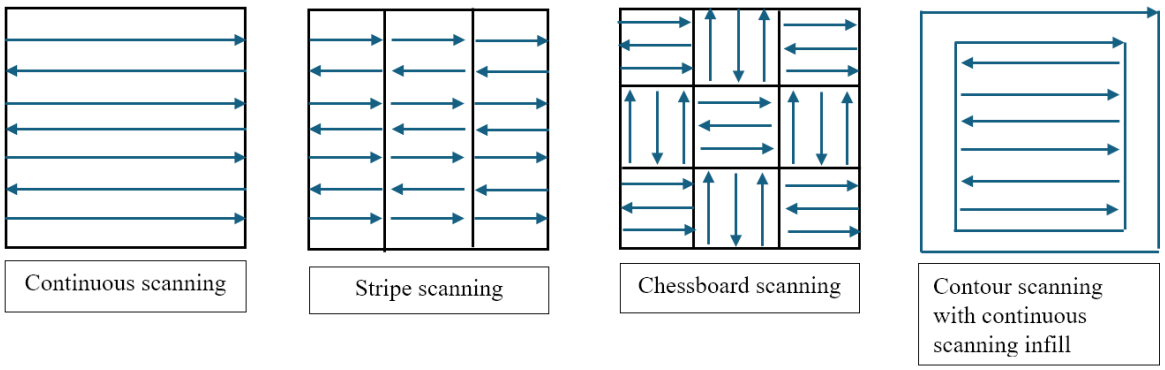


Figure 7 Four common scanning patterns in PBF-LB/M. [31] [47] [48]

As Figure 7 shows, continuous scanning pattern features adjacent scan vectors within a single layer and the length of the vectors are limited only by the part contour. Stripe and chessboard scanning patterns enable control over the maximum vector length. The layer is divided into stripes of specified width in stripe scanning, after which vectors are fitted between the stripes. Chessboard scanning pattern includes dividing the layer to squares in which vectors are fitted and the vector direction can be rotated between separate squares. Definition of stripe width or island size enables the control over maximum vector length in stripe and chessboard scanning. Contour scanning features pre-defined number of vectors that are arranged concentric to the part boundaries and the rest of the part interior can be scanned with another scan pattern. The contour scan pattern example in Figure 7 features two contour scans while continuous scan pattern is used on the rest of the layer. The overall scanning pattern can be modified also by changing the vector directions in the scanning pattern. As can be seen from Figure 7, the continuous, stripe and chessboard scanning patterns feature bi-directional vectors. However, the vector direction could be unidirectional as well, meaning that all of the vectors have the same direction. [31] [47] [48]

## 3.3 Volumetric energy density (*VED*)

It can be challenging to compare different sets of parameters in PBF-LB/M as there are many parameters which affect how much energy is delivered to melt the material. *VED* provides a standardized metric which describes the total energy input per volume unit (J/mm$^3$) to the processed material [32]. *VED* can be calculated according to equation 3, where $P$ is the laser power (W), $v$ is the scan speed (mm/s), $h$ is the hatch spacing (mm) and $t$ is the layer thickness (mm) [32] [33].

$$VED = \frac{P}{v \cdot h \cdot t} \tag{3}$$

As *VED* combines several parameters it does not accurately describe optimal process conditions. For example, Bertoli et al. [49] studied the melt track formation of 316L with multiple parameter sets resulting in the same *VED*. It was concluded that with the same *VED* value the resulting melt track morphology can differ significantly [49]. However, *VED* can be used as auxiliary value for easier comparison of different parameter sets.

# 4 Defects in PBF-LB/M produced parts

Modern manufacturing processes, like PBF-LB/M, have their advantages and potential to revolutionize the industry. However, certain limitations and challenges remain inherent to the technology. Defects like surface roughness and porosity form one of the challenges for PBF-LB/M produced parts [31] [8]. Continuous technological development efforts are made to mitigate these challenges. It is essential to understand the underlying fundamental principles to overcome the limitations.

## 4.1 Surface roughness

Surface roughness describes the condition of material surface as it is determined by topographical variations and irregularities on the surface [50]. It can be numerically quantified, and it is commonly expressed as average roughness of a profile (*Ra*) in the literature [13] [51] [52] [53] [54]. As it can be seen from Figure 8, *Ra* indicates the average deviation (µm) of the measured surface profile from the nominal surface profile [55].

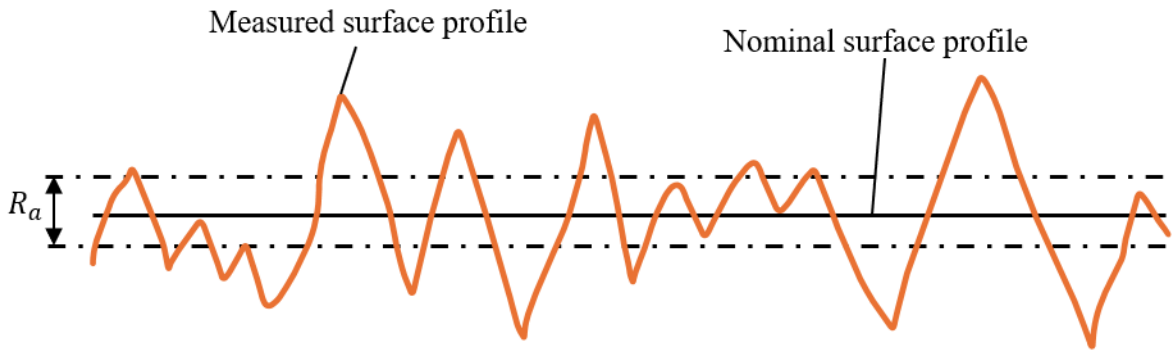


Figure 8 Average roughness of a surface profile *(Ra)*. [55]

Surface roughness is essential property to study and understand in additively manufactured (AMed) parts, because it is often higher compared to traditionally manufactured parts, thus it can limit the applicability of the technology. Surface roughness does not only affect the appearance of a part, but it can also be detrimental to the fatigue performance, as the surface irregularities can act as crack initiators [52]. In applications where the surface roughness is critical, it is often necessary to improve the surface roughness via post-processing techniques, such as machining and polishing [13].

There are several formation mechanisms for surface roughness in PBF-LB/M. The resulting roughness tends to vary for different surfaces due to different formation mechanisms. Figure 9 illustrates different types of surfaces in PBF-LB/M.

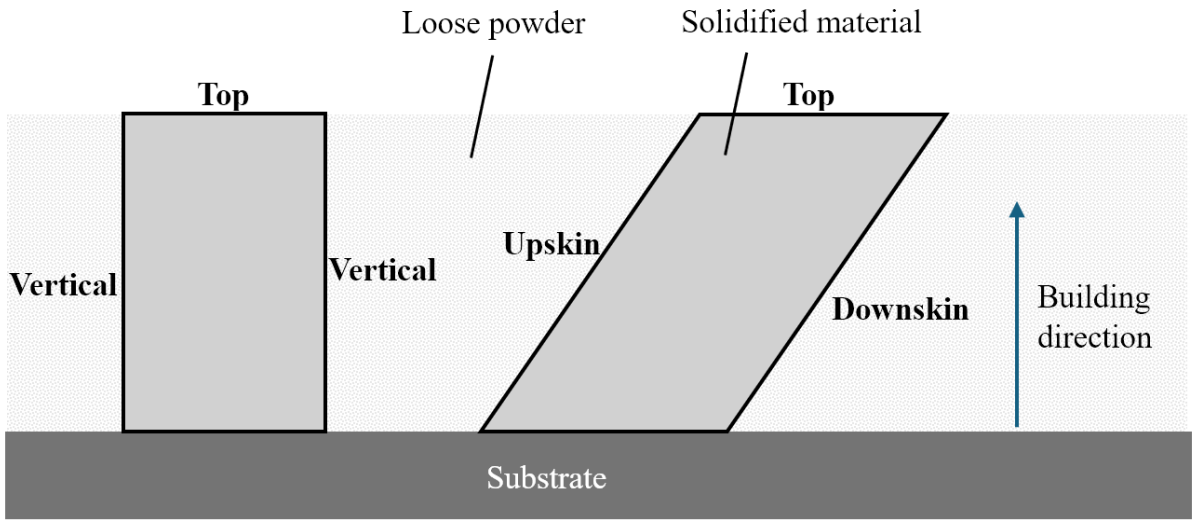


Figure 9 Different types of surfaces in PBF-LB/M. [11] [56] [51]

As can be seen from Figure 9, all the other surfaces are exposed to the loose powder, except the top surface, which is the surface of the last layer. The way how melt pool is formed and solidified is a major contributor to the surface roughness of the top surface [11]. Poor wettability of molten material can increase surface roughness through balling phenomenon in PBF-LB/M [51] [31]. When molten material has insufficient wettability, it does not spread evenly on the substrate but forms small spheres of material due to surface tension. Increasing the energy density can improve the wettability through increasing the temperature of molten material, which in turn leads to reduced surface tension [51] [31]. Zhou et al. [51] suggested that balling effect with IN718 can be caused by Rayleigh-Plateau instability. Figure 10 illustrates balling formation due to Rayleigh-Plateau instability.

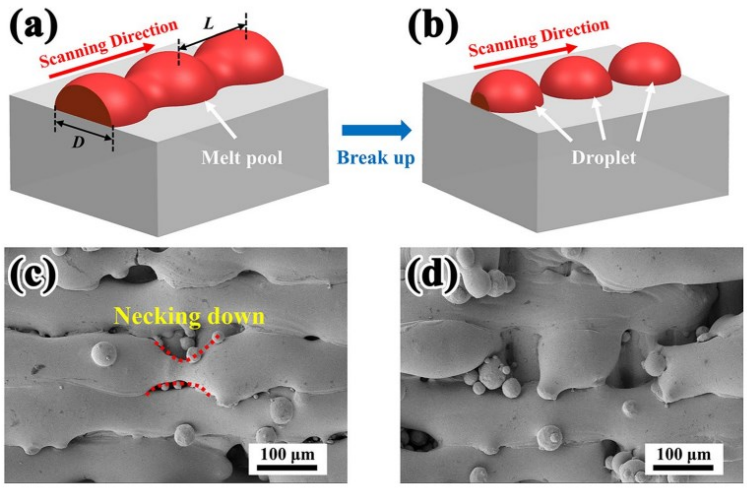


Figure 10 Balling formation due to Rayleigh-Plateau instability. Reproduced from [52].

As it can be seen from Figure 10 a, the local melt pool is assumed to be a cylinder with diameter of D with small perturbations due to surface tension. The surface tension tends to break the melt pool into droplets (Figure 10 b), when the wavelength (L) of melt pool perturbation exceeds the circumference of the cylinder (πD). Figure 10 c shows morphology of incompletely broken scan track, and Figure 10 d completely broken scan track [52]. The presence of such instabilities leads to higher surface roughness [52].

All other surfaces apart from the top surface are surrounded by loose powder during the build process, as illustrated in Figure 9. Contact with the loose powder can cause semi-molten powder particles to adhere to the surface, which will increase the surface roughness. The increase in surface roughness due to adhered powder particles is notable for vertical surfaces. Generally, the roughness of these surfaces can be improved by lowering the heat input, as the amount of adhered powder particles decrease. There are other more dominating factors affecting the roughness of inclined downskin and upskin surfaces, such as staircase effect and dross formation. [54] [11]

Staircase effect may increase the roughness of inclined surfaces. The staircase effect originates from the layer-wise slicing and fabrication of the part. Staircase effect is illustrated in Figure 11.

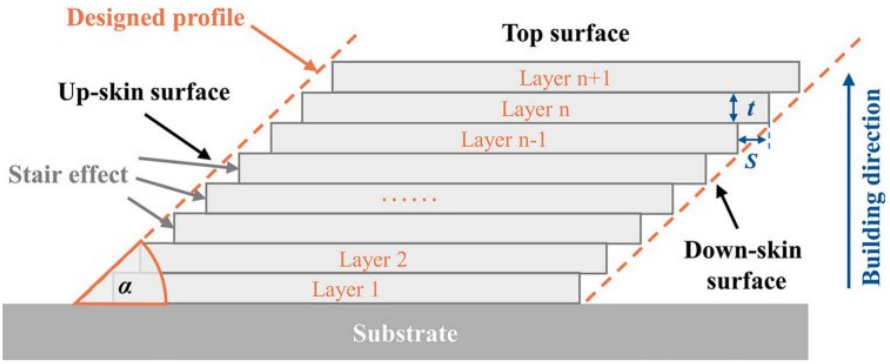


Figure 11 Staircase effect in AM. Reproduced from [51].

Furthermore, inclined downskin surfaces are more prone to high surface roughness than the upskin surfaces [51]. This is partly due to the localized heat accumulation in the downskin region, which is illustrated in Figure 12.

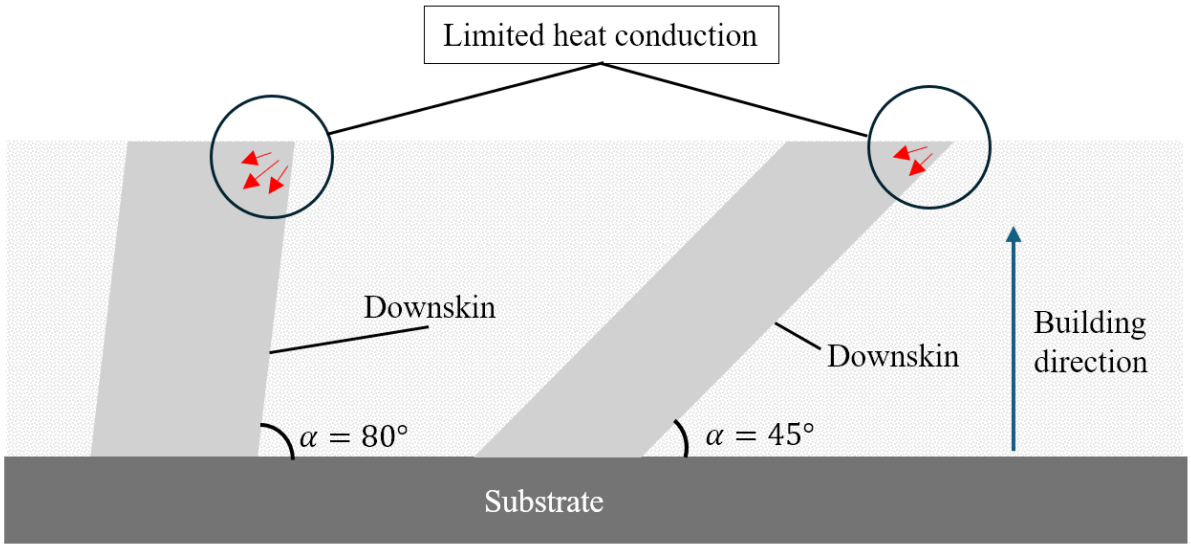


Figure 12 Limited heat conduction in downskin regions. [56] [53]

As Figure 12 illustrates, the heat conduction is limited in the corners of the downskin, as the loose powder acts as an insulator [56]. Hereby, the heat can conduct mainly through previously solidified material as illustrated with red arrows in Figure 12. The limitation in heat conduction is further increased as the build angle α is lowered (Figure 12, α=80° vs.

α=45°) as there is less material through which the heat can conduct. Heat accumulation then promotes dross formation, which is a type of defect that increases the surface roughness. Dross formation occurs when the melt pool size increases due to heat accumulation and the melt pool extends over the part contour as it is also subject to gravitational and capillary forces. This causes protruding structures to the surface which increases the roughness [53]. Viale et. al [56] suggested that there is a critical overhang angle for each PBF-LB/M material, below which dross formation starts to occur and that lower angles with less dross formation can be printed by lowering the heat input.

## 4.2 Porosity

Porosity is a common defect in PBF-LB/M, and it refers to internal voids within the manufactured part. It is often expressed as total percentage (%) of the voids within the manufactured part. Like surface roughness, porosity can impair mechanical properties of the part, such as tensile strength and fatigue performance. Pores within the part can promote crack formation and growth as they concentrate the stresses during cyclic loads. Increasing the quality of a part with porosity defects via post-processing is limited, since porosity is located inside the part. However, porosity can be decreased to a certain level via hot isostatic pressing or laser post-treatment re-melting. [8]

Pores can be formed in various ways; thus, they can be divided into different categories based on their formation mechanism. According to Du et al. [8] there are two main types of porosity: gas pores and lack of fusion. Gas pores are originating from a gas bubble entrapped within the material during solidification; thus, they are spherical in shape [9]. Most typical source of gas pores in PBF-LB/M is keyhole melting mode due to excessive energy density [8]. Melting occurs in conduction mode under optimal energy density and the melt pool is stable and typically semicircular in shape [57]. However, the melt pool enters the keyhole mode if certain energy threshold is exceeded, causing a formation of a cavity filled with metal vapor while the depth of melt pool increases significantly [57]. Melt pool is unstable in the keyhole mode as the keyhole fluctuates continuously due to complex melt pool dynamics [8] Figure 13 illustrates the formation of keyhole induced gas pore.

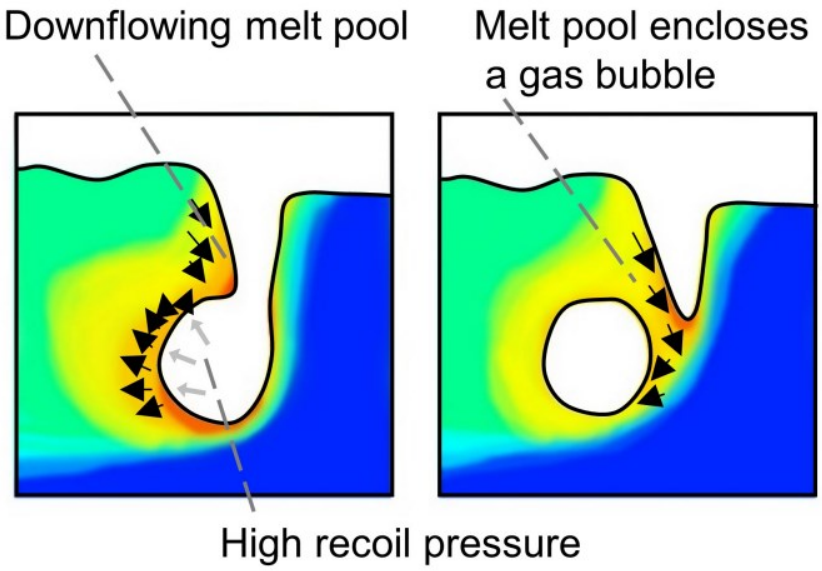


Figure 13 Formation of keyhole induced gas pore. Reproduced from [58] which is under Creative Commons CC BY-NC-ND 3.0 license.

As Figure 13 shows, high recoil pressure from vaporized metal forms a cavity within the melt pool. Surface tension in the top of the cavity is higher, which results in molten material flowing down on top of the cavity. As the keyhole collapses a gas bubble is entrapped into the melt pool [58]. The gas bubble shrinks continuously due to metal vapor condensation and when melt pool solidifies the gas bubble is retained within the material as porosity [8]. During the keyhole melting mode, the keyhole collapses and forms again continuously, causing a steady stream of keyhole pores if the process control is not regained [8]. Reducing energy density through decreasing laser power or increasing scanning speed is one of the solutions for avoiding keyhole melting mode [9].

Gas pores can also originate from the initial powder feedstock material. Metal powder used in PBF-LB/M is produced commonly via gas atomization. During the manufacturing process, a molten metal stream is broken down into small droplets with pressurized gas. Gas bubbles may get entrapped into the molten metal droplet during their formation. Droplet formation is followed by rapid cooling, which can prevent the gas bubbles from escaping before droplet solidifies into a powder particle [8]. According to Chen et al. [59] gas atomization can produce porosity of around 0.2% in the powder. It has been observed that the porosity within the powder feedstock is preserved within the AMed material with electron beam powder bed fusion (PBF-EB/M) [60] [61]. Tammas-Williams et al. [60] observed gas pores within PBF-EB/M processed material and concluded that the pores originate from the feedstock material

which had similar amount of porosity than the final parts. It was suggested that the main source of gas porosity in PBF-EB/M stems from powder feedstock, as the process takes place under vacuum [60]. Cunningham et al. [61] concluded that when the porosity within the powder feedstock material decreased, the porosity of the final AMed part also decreased to a similar extent. According to Du et al. [8] the same mechanism of feedstock originating gas porosity can be present also within the PBF-LB/M process.

Moisture in the PBF-LB/M process chamber and the feedstock material can lead to increased porosity in the form of hydrogen pores [8]. Weingarten et al. [62] studied porosity of AlSi10Mg and concluded that 96% of the gas content within the gas pores is hydrogen. It was observed that pre-drying of the feedstock material leads to reduced porosity content [62]. Huang et al. [63] suggested that the dissolved hydrogen within the melt pool can diffuse to the keyhole induced pores during cooling of the molten pool. It was explained that the molten metal can become supersaturated with hydrogen as the solubility of hydrogen decreases during the cooling of the liquid metal [63].

Lack of fusion (LOF) is a type of porosity in PBF-LB/M, which is caused by insufficient melting of the powder material leading to more irregularly shaped pores compared to gas pores. Du et al. [8] categorized LOF porosity to intertrack, interlayer and spattering induced LOF. Interlayer LOF is caused by insufficient energy density to melt the whole layer of powder, which results in incomplete merging of consecutive layers [8]. According to Panwisawas et al. [64], interlayer LOF can also form due to rapid solidification of the melt pool, which does not allow the molten material to merge into the previous layer. As can be observed from Figure 14, interlayer LOF is longitudinal with scan direction and is located between the interface of consecutive layers [65].

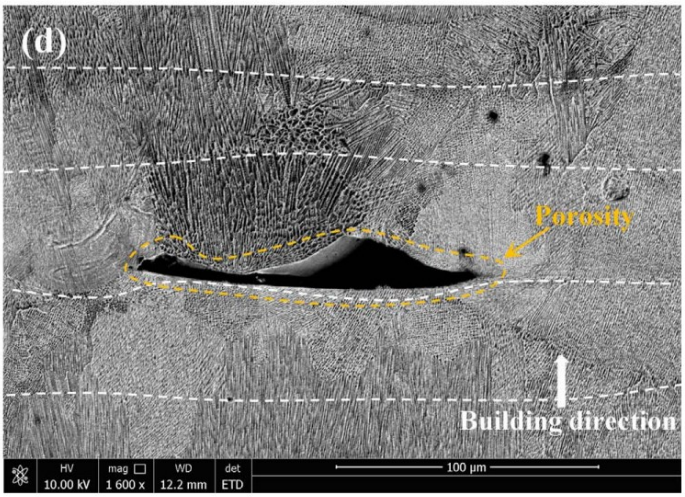


Figure 14 Interlayer LOF in PBF-LB/M produced IN718. Reproduced from [65].

Intertrack LOF is another type of LOF porosity, and it is caused by insufficient overlap between adjacent scan paths. It can occur if the melt pool is not wide enough or the hatch spacing is too high [8]. Figure 15 illustrates the formation of intertrack LOF when hatch spacing is increased according to the computational fluid dynamics simulations by Cao L. [66].

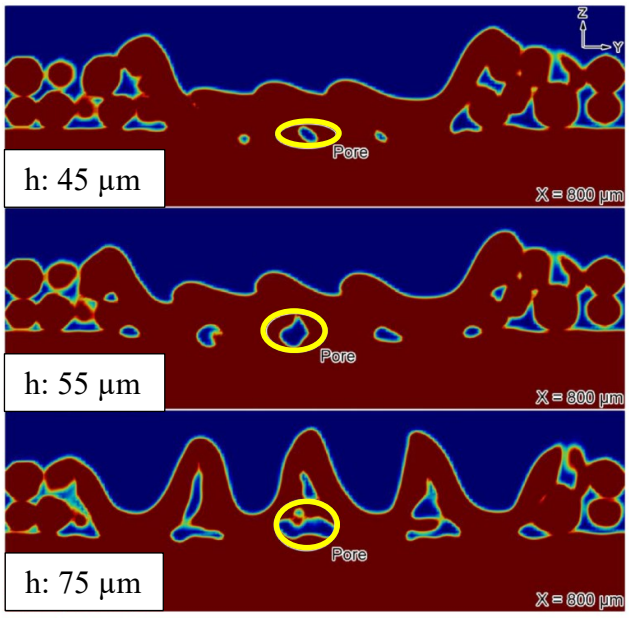


Figure 15 Intertrack LOF formation (highlighted with yellow) with different hatch spacings (h). The scan direction of the laser beam is along the x-axis which is towards the observer. Reproduced and modified from [66].

As Figure 15 reveals, hatch spacing of 45 µm caused porosity between adjacent scan tracks with the used experimental setup. Intertrack porosity was further exacerbated as the hatch spacing was increased up to 75 µm [66].

Spatters that are present in the PBF-LB/M process can also cause LOF porosity [8]. Spatter refers to the ejected molten material due to recoil pressure during the laser material interaction [67]. Spatter particles that reside on top of the manufactured part may hinder uniform spreading of powder during the recoating, which can prevent the complete melting of the powder layer as suggested by Esmaeilizadeh et al. [68] and Laleh et al. [69]. According to Schwerz et al. [65], spatter particles can absorb and scatter the energy from the laser during the processing, which can lead to LOF due to decreased amount of energy delivered to the powder bed. Ali et al. [70] studied spatter induced porosity formation by manufacturing PBF-LB/M samples near the inert gas outlet and inlet. It was concluded that spatter existed in larger quantities at the gas outlet, which led to increased porosity in the parts manufactured near the gas outlet [70].

# 5 Effect of *LBAI* and scanning strategy on defect formation

Effect of *LBAI* [14] [10] [13] [52] and scanning strategy [34] [71] [72] [73] on defect formation in PBF-LB/M has been studied separately in the literature according to the knowledge of the author. State-of-the art literature regarding defect formation for both variables are reviewed to underlie the experimental part of the thesis.

## 5.1 Effect of *LBAI*

Due to the non-telecentric scanning lens in PBF-LB/M systems, the laser beam hits the powder bed with an angle (*LBAI*) in all locations except at the optical center, as illustrated in Figure 16 [27].

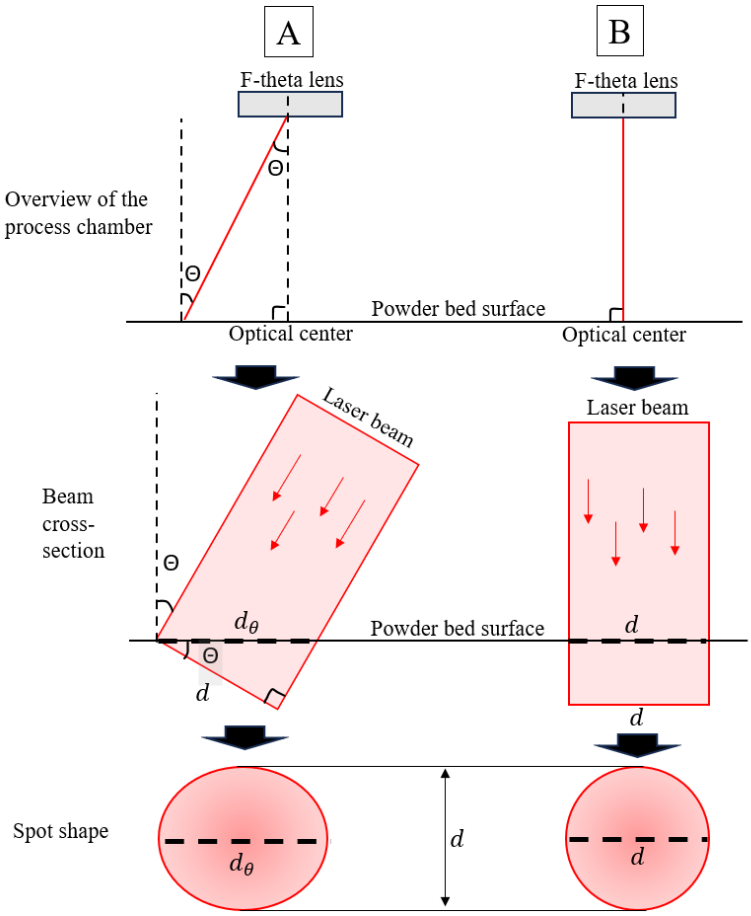


Figure 16 The effect of increased *LBAI* on the beam spot. For illustrative purposes the laser beam cross-section is depicted as rectangle. Illustration based on [6], [14], [15] & [27].

As Figure 16 A shows, the beam which is deflected away from the optical axis has *LBAI* of θ, which causes the beam to illuminate a wider area, resulting in elliptical spot shape. The spot is elongated parallel to the incidence direction of the beam. Spot diameter in the elongation

direction is $d_\theta$, while $d$ is the diameter of the beam. When the beam is deflected to the optical center (Figure 16 B), the resulting *LBAI* is zero, thus the spot remains circular. Deflecting the beam further away from the optical center increases the *LBAI*, thus the spot elongation will be more severe. In both cases the beam is the same, thus it has the same laser power. However, the elongated elliptical spot has wider interaction area thus the power density of the beam is lower, which leads to *LBAI* dependent variations in power density of the laser beam across the build platform [14].

Li et al. [15] concluded that *LBAI* of 30° decreased the power density up to 13.40% with 100 µm beam spot. In study by Fathi-Hafsejani et al. [14] it was observed that increasing the *LBAI* results in wider and shallower melt pools. The effect of *LBAI* on melt pool depth varied depending on the scanning direction of the elongated beam. Figure 17 illustrates the different scenarios where circular (a) or elliptical (b & c) spot is scanned along single vector and the resulting melt pool depths (d) [14].

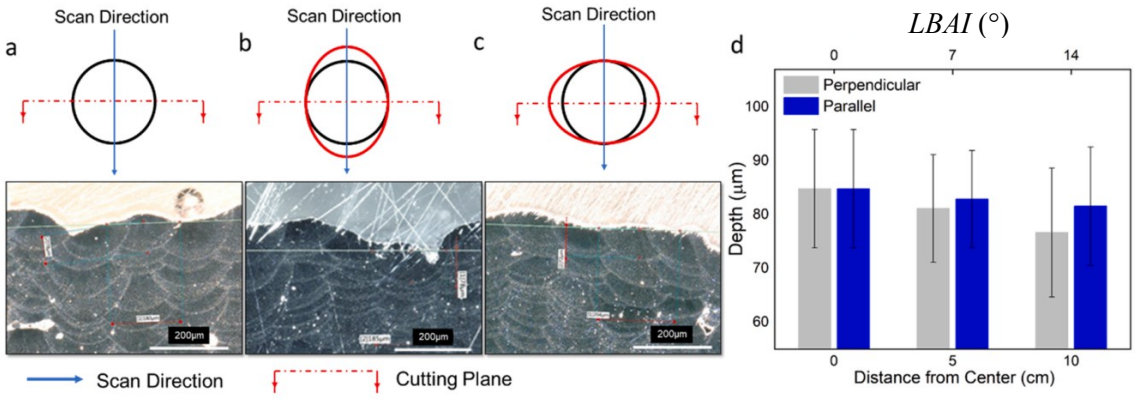


Figure 17 Different scan vector directions for elongated beam spots and the corresponding melt pool depths with different *LBAI*s (d). Reproduced and modified from [14].

As can be seen from Figure 17, scan vector direction of elongated beam can be parallel (b) or perpendicular (c) with the elongation of the spot. Increasing the *LBAI* results in decrease in melt pool depth for both cases. However, when the scan vector direction is perpendicular with the elongation (Figure 17 c), the decrease in melt pool depth is more noticeable. According to Fathi-Hafsejani et al. [14] the parallel scan direction (Figure 17 b) results in increased interaction time between the laser and the material due to the extended area of the spot in the scan path. Increased interaction time will compensate for the loss of power density and the melt pool depth remains almost unaffected. Correspondingly, perpendicular scan direction (Figure 17 c) does not increase the spot area within the scan path, thus there is no

compensation for power density reduction. This will lead to more visible decrease in the melt pool depth, as in Figure 17 d. Figure 17 d also reveals that when the *LBAI* is zero, the scan direction does not affect the melt pool depth, as the spot shape is circular, as in Figure 17 a.

Fathi-Hafshejani et al. [14] concluded that *LBAI* induced laser beam spot variations increase the porosity of manufactured parts. Figure 18 illustrates porosity content of AlSi10Mg with different *LBAI*s [14].

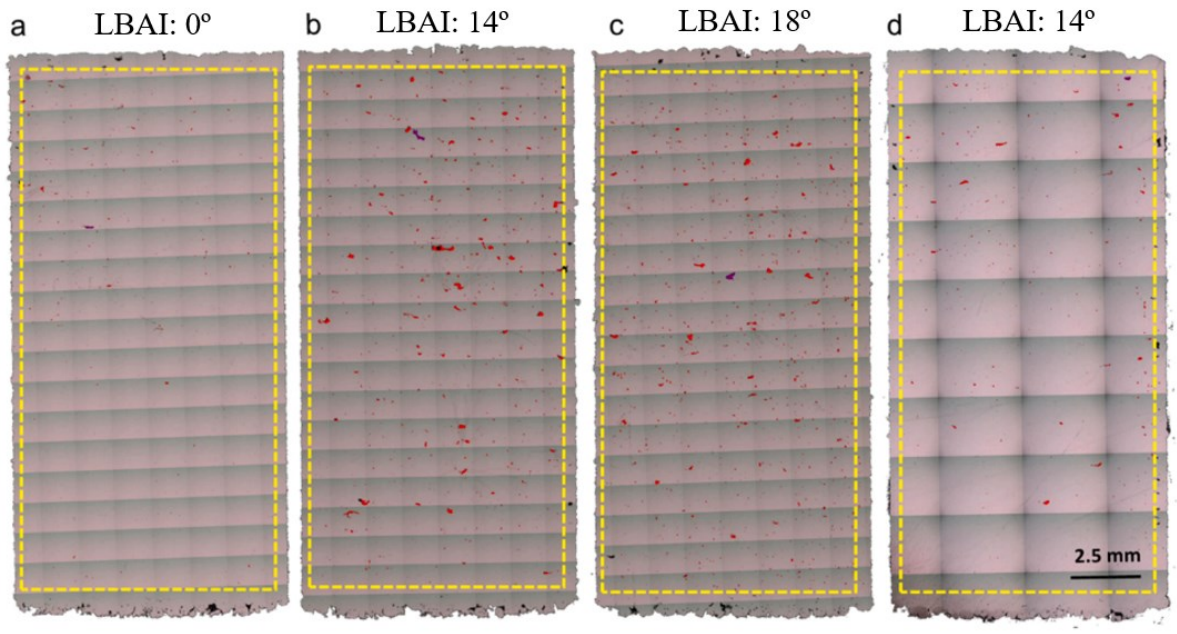


Figure 18 Porosity content of AlSi10Mg manufactured via PBF-LB/M with different *LBAI*s. Reproduced and modified from [14].

As it can be seen from Figure 18 a, *LBAI* of 0º yields low amount of porosity as there is no laser beam spot elongation. Similar amount of porosity was also achieved for *LBAI* of 14º as in Figure 18 d. It was explained that the loss of power density was compensated by scanning the laser beam parallel to the elongation, as described previously. However, in Figure 18 b and c there was no power density compensation as the beam elongation was perpendicular to scan direction, which led to increased amount of irregularly shaped pores, indicating LOF. [14]

Various studies have shown that the *LBAI* together with the part orientation influence the surface roughness [10] [13] [52]. Kleszczynzki et al. [10] concluded that downskin surfaces that are facing away from the laser incidence direction have higher surface roughness than those pointing towards the laser incidence direction. It was suggested that the higher surface

roughness might be due to the presence of melt pool extensions caused by inclined laser beam. These melt pool extensions are further exacerbated by the increased *LBAI*. Chen et al. [13] made similar conclusions about the influence of surface orientation towards the laser incidence direction on the resulting roughness. In the study, the downskin roughness increased for the downskins facing away from the laser origin as the downskins were built further away from the center [13]. With the same *LBAI* the surface roughness can differ depending on the part orientation. Rott et al. [52] introduced surface laser relation angle ζ, which should enhance the comparability of surface roughness data obtained with different process conditions. Figure 19 illustrates the definition of ζ.

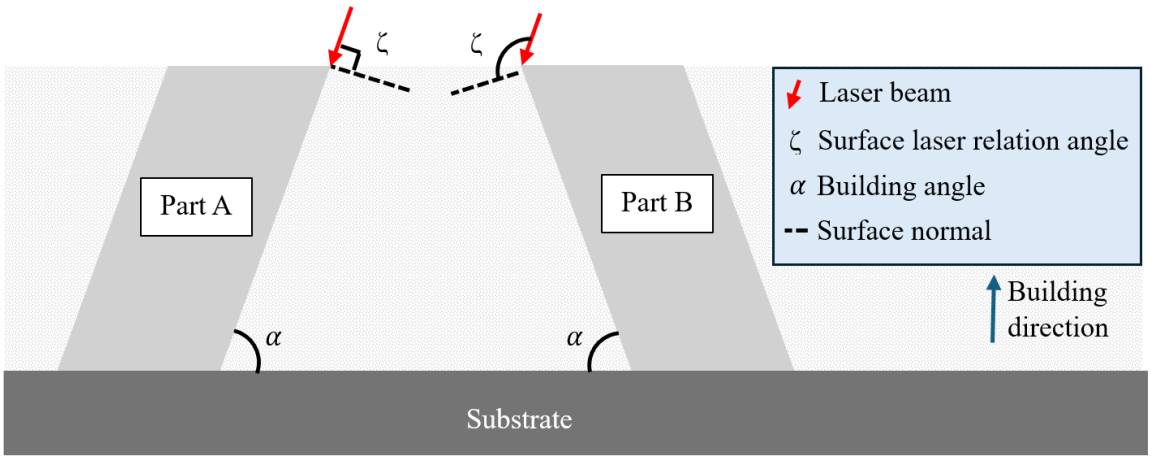


Figure 19 Schematic representation of surface laser relation angle ζ. Adapted from Rott. et al. [52].

As can be seen from Figure 19, ζ can be different depending on the part orientation while the build angle α and laser angle of incidence is the same. Based on the studied literature, the part A, which has ζ of 90° should have smoother surface than the part B where ζ is higher [13] [52]. In the case of part A, the inclined laser beam should not promote the melt pool extensions as the beam is directed to the previously solidified material. On the other hand, the beam that is directed to the loose powder in part B, promotes melt pool extensions as the melt pool penetrates to the powder bed.

## 5.2 Effect of scanning strategy

The definition of scanning strategy in the literature is not standardized, thus it should be clarified in the context of this thesis. In the current work, scanning strategy refers to configuration of scan parameters, which aims to address a certain process related issue. Scanning strategy includes for example the sequence of used scan patterns in the process, as

well as the directions of the scan patterns. E.g. rotating stripe pattern between layers at 90° intervals can be considered a separate scanning strategy compared to just keeping the stripe orientation the same layer after layer.

Scanning strategy controls the path of the laser beam across consecutive layers, i.e. where the energy from the beam is applied. Thus, it affects thermal gradients present within the material, which further influences material properties such as microstructure and formation of defects [47]. Scanning strategy that promotes high heat accumulation can lead to high temperature of the melt pool. As melt pool temperature increases, so does the cooling rate of the material, which promotes formation of finer grains [74]. On the other hand, scanning strategy that does not have sufficient overlapping of scan tracks can lead to LOF defects [75]. Several scanning strategies and their influence on defect formation have been studied in the literature [34] [71] [72] [73].

Rotation of scanning paths after consecutive layers is one of the scanning strategy features which has been studied in the literature [47]. Figure 20 illustrates the scanning paths of 90° interlayer rotating continuous scanning strategy with bi-directional vectors.

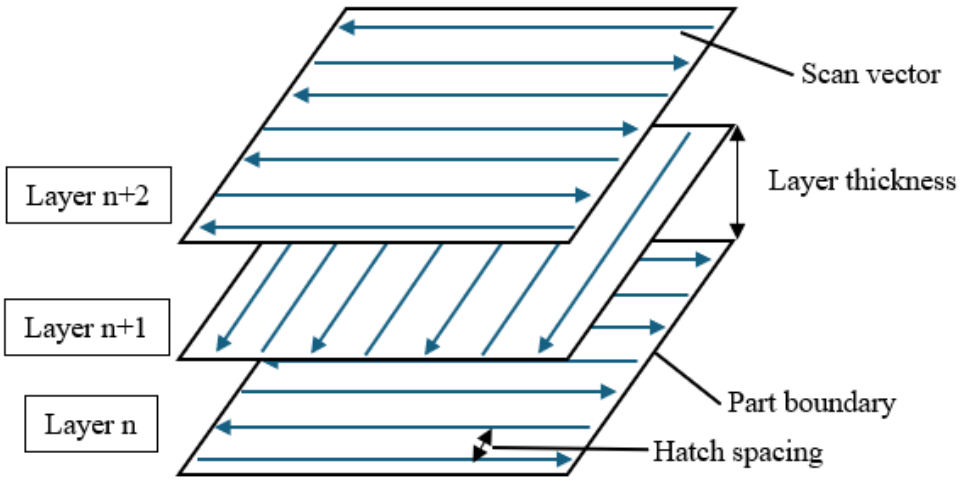


Figure 20 90° interlayer rotating continuous scanning strategy with bi-directional vectors. [47]

As Figure 20 illustrates, the same scan pattern is used in each layer, however the whole array of vectors is rotated 90° after each layer. Many different rotation angles have been studied, such as 90° [76] [71], 67° [77] and 30° [71]. Amirjan & Sakiani [71] concluded that interlayer rotation of scan vectors in continuous scan pattern can reduce porosity of the material. Using

continuous scan pattern without interlayer rotation caused a large number of LOF pores compared to the continuous pattern with interlayer rotation. It was suggested that when scan vector directions are changed in consecutive layers, re-melting of material in previously deposited layers occurs in different directions, which promotes the elimination of LOF porosity as the unmolten material is fused together [71]. Similar conclusions were also made by Bhardwaj & Shukla [76], who studied the effect of 90° rotation scanning strategy on part properties. Lack of interlayer rotation caused LOF porosity to stack layer after layer as the scan direction was kept constant. LOF pores overlapped with the part surface, causing surface irregularities which increased also surface roughness of the part [76].

Dimitrov. et al. [78] compared stripe and chessboard scanning strategy on Ti6Al4V and concluded that chessboard scanning strategy led to lower residual stresses within the manufactured part. It was suggested that it may be due to considerably lower thermal gradient with chessboard scanning strategy [78]. Heat is dissipated across various directions as the individual squares act as radiating unit, which can lead to faster heat dissipation and lower thermal gradient, as suggested by Jia et al. [47]. The size of the squares is an important parameter to consider, as concluded by Lu et al. [72]. Figure 21 illustrates island scanning strategy and the definition of square size.

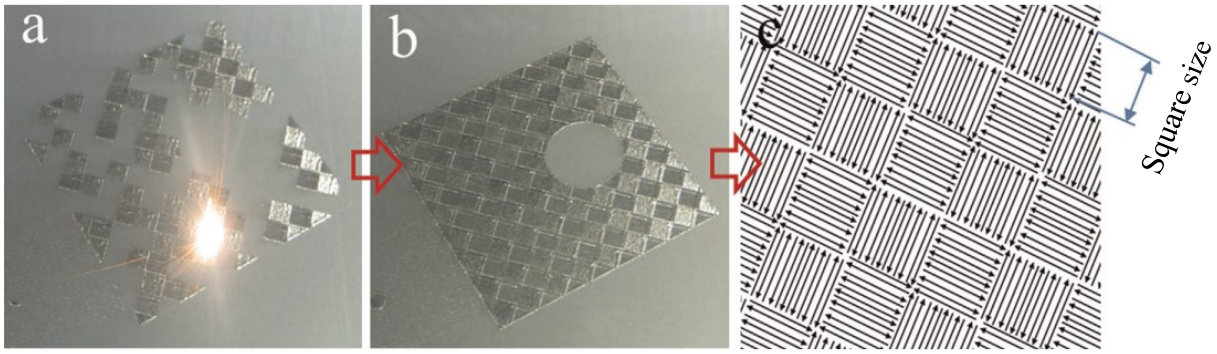


Figure 21 Chessboard scanning during PBF-LB/M process. Reproduced and modified from [72].

As can be seen from Figure 21 a and b, the single squares are randomly scanned until the whole layer has been fused. Square size is directly proportional to the length of the scan vectors, as Figure 21 c illustrates. According to Lu et al. [72], 2x2mm squares resulted in cracking of the material which in turn reduces the mechanical properties and density of the part. It was suggested that short vectors cause more local heat accumulation, as the laser is scanning more rapidly the adjacent tracks. Increasing the square size up to 7x7 mm yielded denser part. It was explained that increasing square size decreases the number of “crisscross”

sites, i.e. the gaps between where four separate squares meet. LOF defects were observed more frequently in these sites, thus restricting them could also reduce LOF [72]. Similar conclusions were also made by Zhang et al. [79] who studied chessboard and stripe scanning strategies with 316L. It was concluded that chessboard scanning strategy yielded more LOF defects, resulting in inferior fatigue strength compared to stripe scanning. It was suggested that chessboard scanning strategy yields more interfaces between scan tracks, which promotes formation of intertrack LOF [79].

Defect reduction can be achieved through introduction of re-melting to the scanning strategy. Re-melting can be achieved for example by scanning previously scanned area again before depositing the next layer [47] or by introducing additional contour scans to the part periphery [73]. Re-melting can mitigate porosity as the material is melted again, which enables more complete fusion of material [80]. Tian et al. [71] concluded that contour scans re-melt the surface irregularities, which improves the surface roughness of the part. However, re-melting is recommended to be carried out with lower energy density to avoid residual stresses or cracks [31]. Drawback of this approach is the decreased productivity due increased production time [31].

During the start of laser scanning in PBF-LB/M, the scanning mirrors require some time to accelerate to the set scanning speed. This leads to non-constant speed of the beam before reaching the target speed. This uneven speed at the start of a scan vector can impair surface roughness and geometrical accuracy [73] [48]. Tian et al. [73] studied the skywriting scanning strategy to tackle the challenges posed by inertia of the scanning mirrors. Skywriting aims to compensate the inertia of the scanning via accelerating and decelerating the scanning mirrors before the laser is turned on. Figure 22 illustrates the skywriting scan paths and the effect of utilizing skywriting on surface roughness.

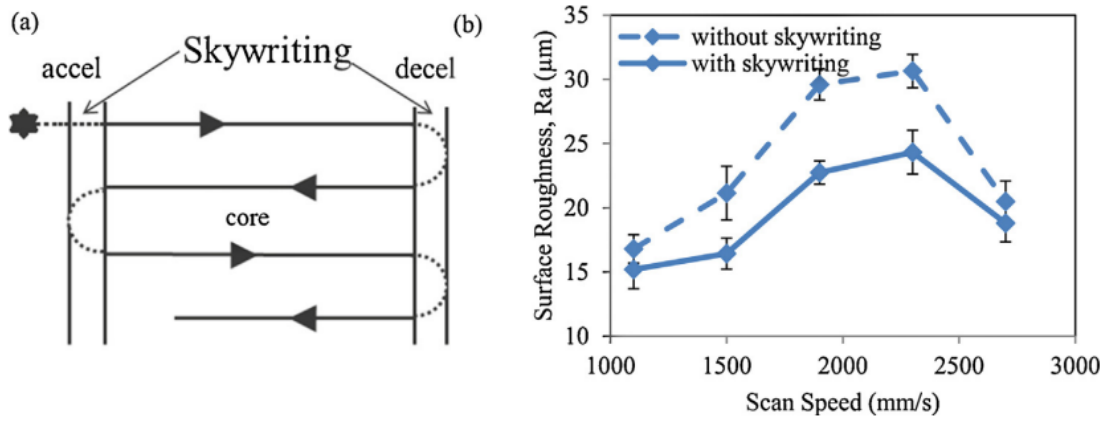


Figure 22 Skywriting scan path and the effect of it on surface roughness. Reproduced from [73].

As can be seen from Figure 22 a, additional acceleration scan paths are added to the ends of the actual scanning vectors. As Figure 22 b illustrates, utilizing skywriting led to lower surface roughness values across variety of scan speeds. It was explained that without skywriting, more heat is applied to the part edges due to slower scan speeds during acceleration and deceleration, which can lead to surface irregularities [73]. Skywriting can be beneficial when utilizing contour scanning for pointy features such as triangles, as suggested by Duong et al. [48]. This may be due to the sharp edges being more prone to heat accumulation, which the skywriting can prevent by stabilizing the scan speed.

Scanning strategy can also be used to tackle spatter induced porosity, as demonstrated by Liu et al. [34], who studied the effect of scan direction on spatter induced defects. Five scanning directions were used, including against the direction of the flow, as well as perpendicular and along the flow direction. Results revealed that the scanning direction along the flow direction leads to worse surface quality and degraded tensile properties due to increased amount of spatter particles on the powder bed. Figure 23 illustrates the suggested spatter particle trajectories in relation to the flow and scanning direction and formation of spatter induced defects.

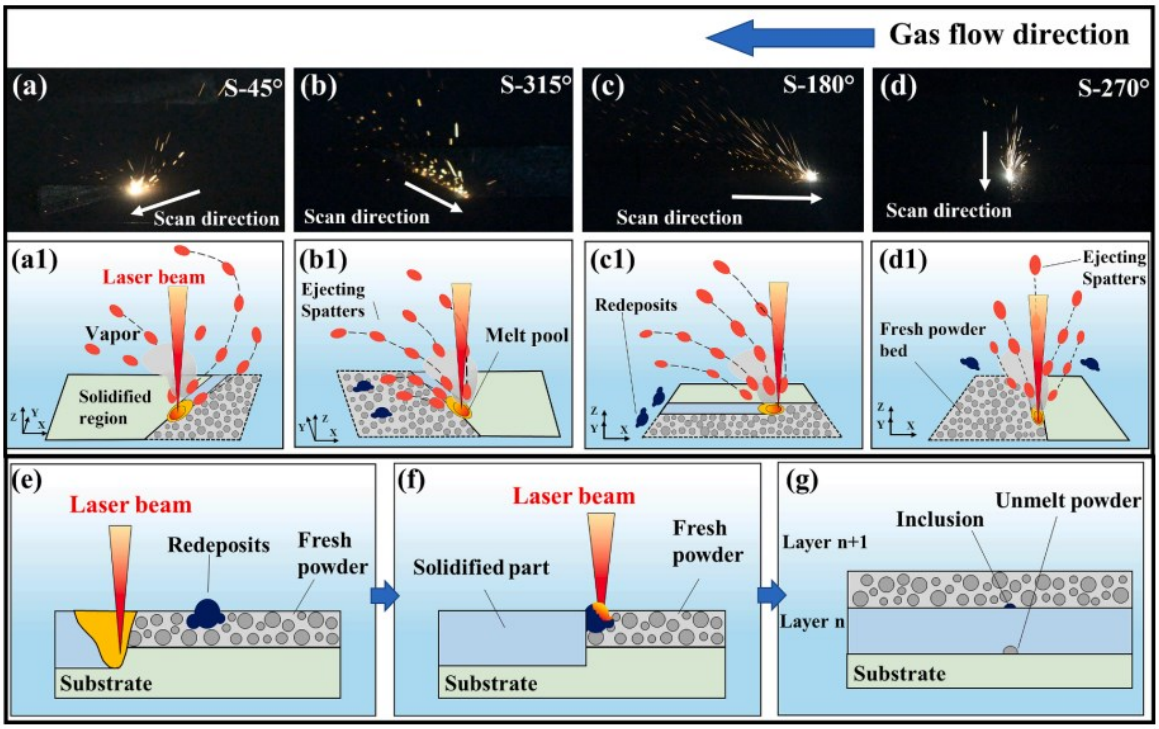


Figure 23 Spatter trajectories in relation to gas flow and scan direction. Reproduced from [34] which is under an open-access Creative Commons CC BY license.

As Figure 23 a-d & a1-d1 shows, the spatter particles tend to initially eject opposite to the scan direction, thus when scan direction is opposite to flow (b & c), the spatter particles are more efficiently transported away from the melting zone. On the other hand, scanning direction along the flow (a) promotes spatter particles to be transported to the zone where powder has not yet been melted. As the laser beam interacts with the spatter particle that is residing on the powder bed, part of the energy is absorbed by the spatter rather than the powder, as in Figure 23 e & f. This results in the spatter remaining as inclusion alongside with unmolten powder (LOF) below it as shown in Figure 23 g. [34]

# 6 Aim and purpose of experiments

The aim of the experimental part is to provide insights on how much the *LBAI* affects the laser beam size and shape and the part properties in EOS M 290 system with IN718. The study aims to support the process development of IN718, as the revealed insights can be used to develop process features to counter the effects of increased *LBAI*. Additionally, these results could be used to further assess the effect of *LBAI* with larger EOS M systems where higher angles are possible due to larger build area.

EOS NickelAlloy IN718 is used in the experiments. Owing to the ability to produce complex parts with PBF-LB/M [81], development efforts has been put in optimizing the process with IN718 in the industry and academia. IN718 is often applied in high-end applications, such as gas turbine components and process industry parts [82]. Low porosity and good surface quality is essential in these applications, thus process development to further enhance these properties is important. The experimental part has been divided into three phases each with their experimental contents, as illustrated in Figure 24

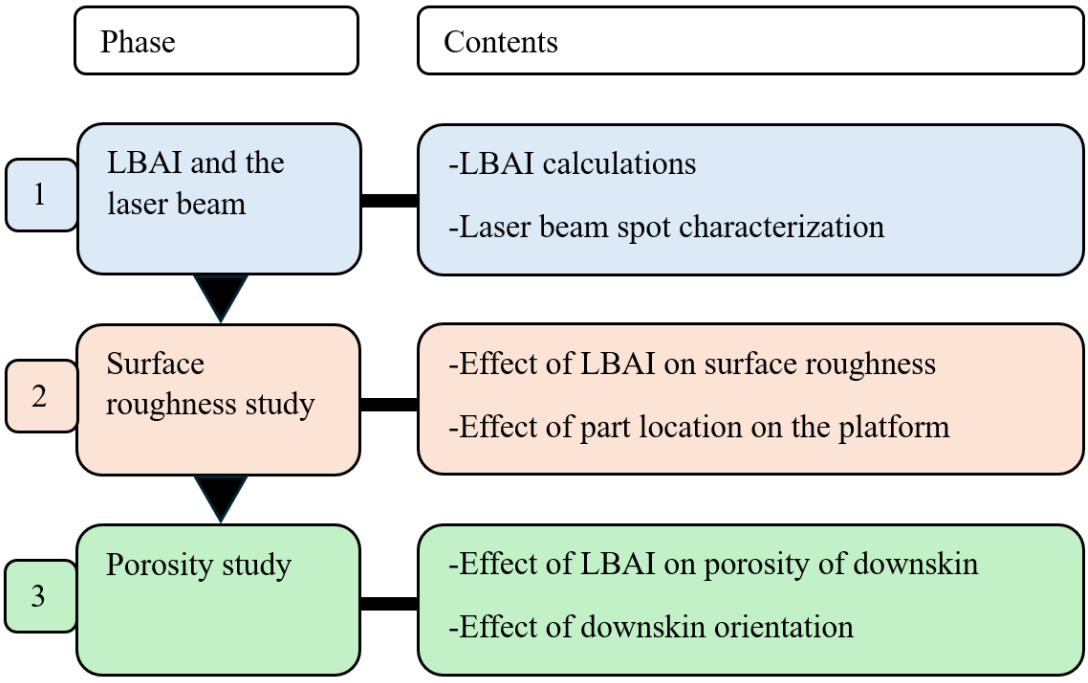


Figure 24 Structure of experimental work.

As can be seen from Figure 24, the first phase includes the definition of *LBAI* in the PBF-LB/M system and laser beam characterization. The goal of this phase is to define the *LBAI* related boundaries of the used equipment and to understand how the laser beam is affected

when these boundaries are approached. Practically, the maximum *LBAI* of the system configuration is determined and the effect on laser beam spot size and shape is investigated. As a result, from this phase there should be an idea of what is the most extreme *LBAI* that can be achieved with the used machine and how does it affect the laser beam spot.

The second phase from Figure 24 includes the study of surface roughness. It involves designing and manufacturing a test print job from which surface roughness data can be acquired. Parts with downskin and upskin regions as well as vertical surfaces are designed to capture surface roughness from various surface types. Additionally, the effect of part location across the platform is studied. Optical profilometry is used to capture the surface roughness of the parts. As a result, there should be insights on how *LBAI* affects the surface roughness of different surfaces.

Porosity is studied in phase three. Porosity study is focused on downskin regions, as those are often manufactured with lower *VED* compared to infill region to avoid excessive heat accumulation. Lower *VED* is more prone to lack of fusion porosity which is expected to yield larger differences between samples to facilitate easier detection of effect of *LBAI*. Print job is designed and manufactured from which porosity at the downskin region with different *LBAI*s is analyzed via optical microscopy. Additionally, the effect of downskin orientation in relation to the laser beam incidence is assessed. As a result, the effect of *LBAI* and downskin orientation on porosity is revealed.

# 7 Experimental set up

## 7.1 Powder material

The experiments are conducted with IN718, a common nickel-chromium based alloy applied in the field of aerospace and energy industry [83]. IN718 features high strength at elevated temperatures and good corrosion resistance. More specific chemical composition of the powder material can be seen in Table 2. Generic particle size distribution is 20-55 µm and particle morphology is spherical, as can be seen from Figure 25. As-built IN718 can be post hardened via precipitation hardening heat treatment to further increase the tensile properties. Typical surface roughness of as-built material at 45° build angle is around 27 µm and for 90° (vertical) surface is below 5 µm. On average, the defect percentage of the material manufactured with process provided by EOS is 0,03%. [82]

Table 2 Nominal chemical composition of IN718 provided by material manufacturer. Reproduced from [82].

| | Element | Fe | Ni | Cr | Nb | Mo | Ti | Al |
|---|---|---|---|---|---|---|---|---|
| Wt.-% | Min. | Balance | 50.00 | 17.00 | 4.75 | 2.80 | 0.65 | 0.20 |
| | Max. | | 55.00 | 21.00 | 5.50 | 3.30 | 1.15 | 0.80 |

| | Element | Co | Cu | Si | Mn | Ta | C | S | P | B | Pb | Se | Bi |
|---|---|---|---|---|---|---|---|---|---|---|---|---|---|
| Wt.-% | Min. | - | - | - | - | - | - | - | - | - | - | - | - |
| | Max. | 1.00 | 0.30 | 0.35 | 0.35 | 0.05 | 0.08 | 0.015 | 0.015 | 0.006 | 0.0005 | 0.0020 | 0.00003 |

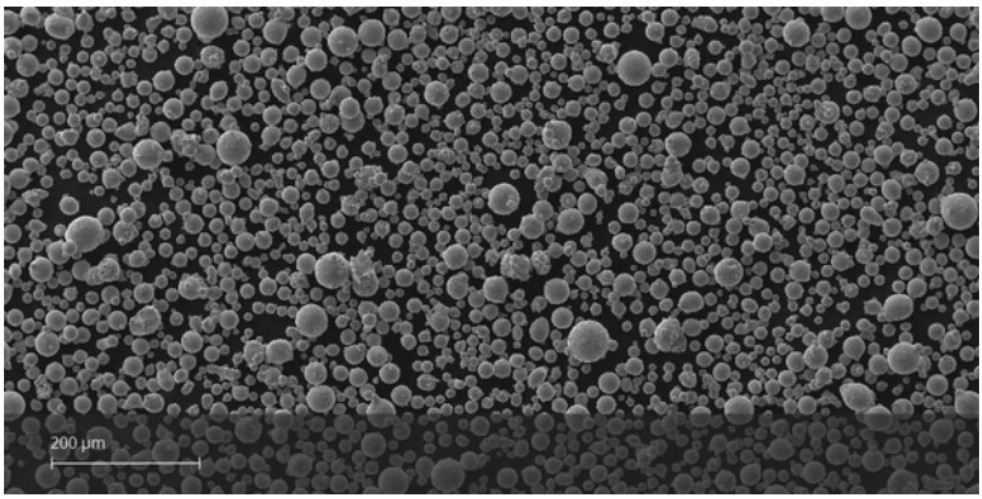


Figure 25 IN718 SEM micrograph. Reproduced from [82].

## 7.2 PBF-LB/M machine

EOS M 290 was used to manufacture the samples. It is a mid-sized PBF-LB/M system by EOS GmbH, featuring a 400W ytterbium-fiber laser, F-theta optics and wide selection of compatible materials [84]. The wavelength of the laser is 1060 – 1100 nm [17]. Total build area of the system is 250 x 250 mm in xy-plane and build height in z-axis is 325 mm. [84] Figure 26 illustrates the process chamber with the inert gas flow, recoating direction and the approximate optical center.

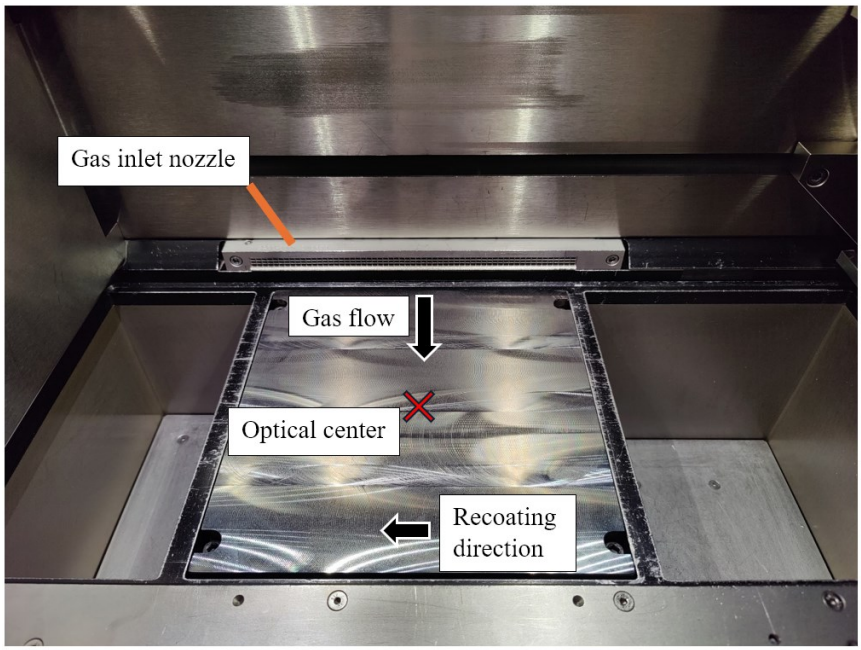


Figure 26 Process chamber as observed from the process window. Steel platform is attached while the powder dispenser and overflow bin are empty of powder.

As can be seen from Figure 26, inert gas is flushed from the back of the process chamber on top of the build area. Gas exits the process chamber from the front where outlet nozzle is located (not installed in Figure 26). This creates a continuous gas flow which removes process by-products that could disturb the process. During the recoating, the recoater arm moves from the right to the left while spreading uniform powder layer onto the build platform with either a hard or soft recoater blade. Optical center is approximately in the middle of the build platform and the laser beam enters the process chamber from top through a protective glass window. [17]

## 7.3 Software

Numerous different software was utilized during the experiments. Software was used for tasks such as print file preparation and data extraction from various measurements. Table 3 collects all the essential software used in the experimental part of the thesis.

Table 3 Essential software used in the experiments.

| Software name | Use |
|---|---|
| **SolidWorks** | -Designing the test geometries. |
| **Materialise Magics** | -Arranging test parts on the build platform. |
| **LaserDiagnosticsSoftware (LDS)** | -Controlling the scan field monitor for laser characterization and extracting the measurement data. |
| **EOSPRINT (v. 1.20)** | -Manual control of the laser and the scanner for laser beam measurements. |
| **EOSPRINT (v. 2.15)** | -Parametrization of print job.<br>-Sending the print job to the machine. |
| **Alicona MeasureSuite 5.3** | -Surface roughness measurement |
| **Olympus Stream motion** | -Microscopical imaging and optical measurement. |

## 7.4 Measurement equipment

Measurement equipment was used for laser beam characterization and for surface roughness and porosity measurement. Table 4 collects details about the used measurement equipment.

Table 4 Measurement equipment used in the experiments.

| Equipment | Use |
|---|---|
| **Scan field monitor (SFM)** | -Laser beam diameter measurement. |
| **Alicona InfiniteFocus G5** | -Optical profilometry for determination of surface roughness. |
| **Olympus GX51** | -Optical porosity analysis from the AMed samples.<br>-Optical measurement of laser mark dimensions. |

As can be seen from Table 4, Scan field monitor (SFM) from PRIMES GmbH was used as one of the methods for laser beam characterization. Laser beam measurement with SFM is based on the detection of scattered light. Inside the SFM there is a scattering structure embedded in a glass plate. When the laser is scanned over the structure, the light scatters and is detected by a photodiode. When the time of detected signals is tracked and the specific

location and dimensions of the scattering structure are known, path and radius of the laser beam can be determined. [85]

# 8 Experimental procedure

## 8.1 *LBAI* and the laser beam

### 8.1.1 *LBAI* calculations

*LBAI* as a function of radial distance from the platform center was calculated to obtain overview on the differences between various platform locations. In the calculations it was assumed that the optical center, where the angle of incidence is 0°, is at the middle of the build platform. EOS GmbH provided necessary dimensions for calculating the approximate *LBAI* in various platform locations. Figure 27 illustrates the necessary dimensions for calculations.

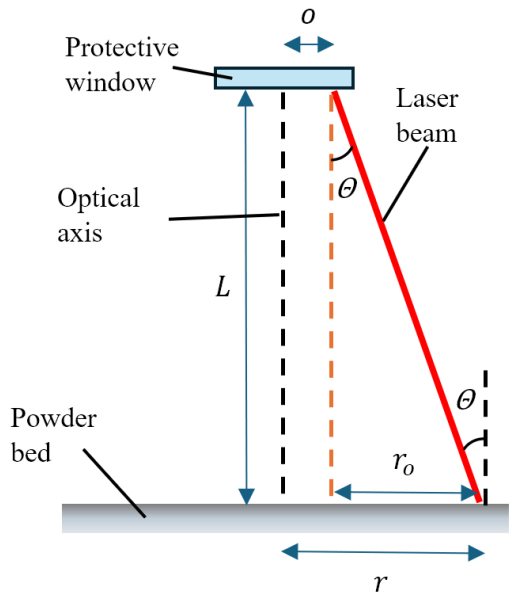


Figure 27 Dimensions for *LBAI* calculation, where *r* is the radial distance of beam spot from the optical center, *o* is the offset of the beam from optical axis entering the process chamber through protective window, *L* is the distance between powder bed surface and protective window and $\Theta$ is the *LBAI*.

As can be seen from Figure 27, when the laser beam is inclined, it does not enter from the optical axis when coming through protective window, but it has a certain offset $o$ (mm). $o$ depends on the radial distance of beam spot from the optical center $r$ (mm); when $r$ is increased $o$ also increases. At the maximum *LBAI*, which is at "$r = 177\ mm$ " (platform corner) $o$ equals 43 mm with this system configuration. In the calculations, $o$ is assumed to increase linearly when the $r$ is increased, thus it can be defined as a function of $r$ as in equation 4.

$$o = r * \frac{43}{177} \tag{4}$$

When both $o$ and $r$ are known, $r_o$ can be calculated, by using equation 5.

$$r_o = r - o \tag{5}$$

By calculating $r_o$ and knowing $L$, which is the distance from powder bed surface to the protective window (481.95 mm), the *LBAI* $\Theta$ can now be calculated by using basic trigonometry, as in equation 6.

$$\Theta = tan^{-1}\left(\frac{r_o}{L}\right) \tag{6}$$

Example calculation is provided in appendix 1.

### 8.1.2 Laser beam spot characterization

Laser beam spot was measured at various locations of the build platform to obtain overview about the effect of *LBAI* on spot size and shape. Two methods were used in laser beam characterization: SFM measurements and optical measurements of laser marks on a steel plate. Figure 28 illustrates the measurement points for SFM and the points where steel plate was exposed. In Figure 28, the measurement points are marked with a cross accompanied by coordinates of the point (x/y) (in mm), while the 0/0 coordinate is at the platform center.

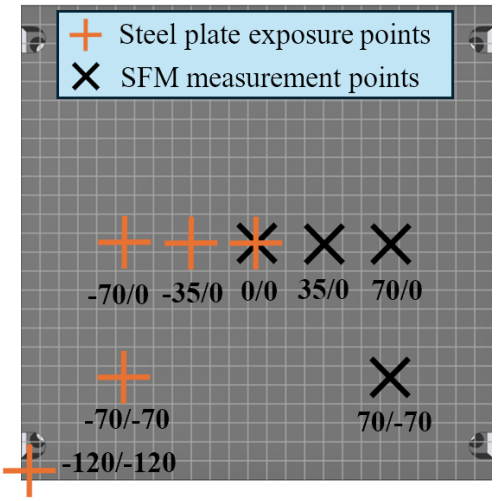


Figure 28 Measurement locations with SFM (black) and points where steel plate was exposed for laser mark measurements (orange).

As can be seen from Figure 28, SFM measurements could be done with limited distance from the center (70/-70) due to the size of the measurement instrument. Steel plate was exposed at the same distances from the platform center and additionally near the platform corner (-120/-120). The *LBAI* of measurement locations was calculated according to equations 4-6 and the calculation results are shown in appendix 1 (Table 7).

SFM was used to measure the spot radius in x and y directions. Build platform of PBF-LB/M machine was leveled so that the platform surface is on the focus field of the beam. The platform was lowered so that the diffraction pattern of the SFM was on the focus plane, to obtain measurements from focused laser beam. SFM device was positioned to correct coordinates at each measurement location by utilizing pilot laser. At each measurement location, the laser beam radius in X and Y direction were measured. Additionally, the measurements were performed while the SFM was rotated 45° clockwise to obtain the radius of the beam at corresponding directions, as can be seen from Figure 29.

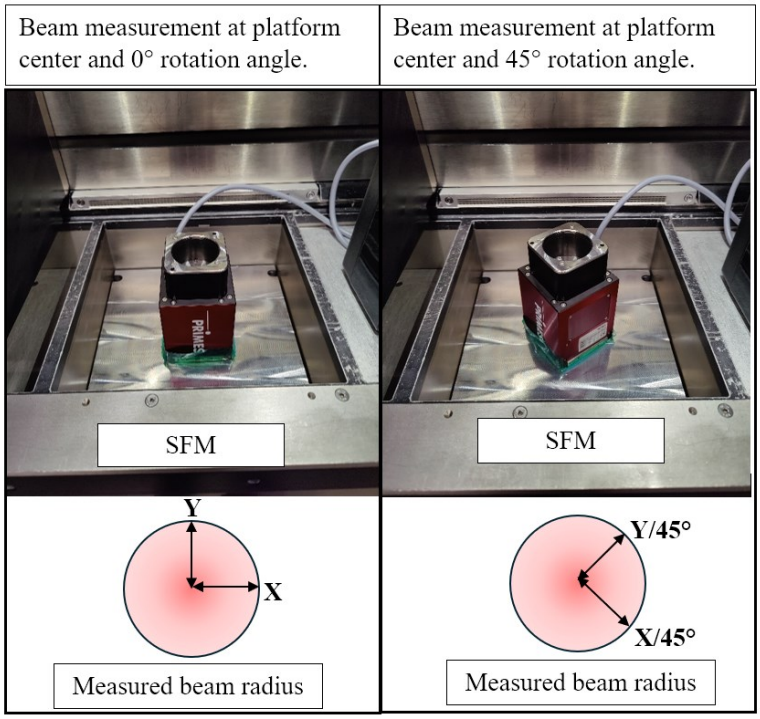


Figure 29 SFM positioning for 0° and 45° beam measurements at the platform center and the corresponding beam radiuses.

As Figure 29 illustrates, the measured beam radius could be adjusted by rotating the SFM device on the build platform. Each measurement was performed 10 times per location and SFM orientation. During the measurement the laser was scanned across the SFM diffraction pattern in x and y directions, with a laser power of 100W and scanning speed of 1000 mm/s.

LDS was used to extract the radius of the beam waist. The acquired radius was multiplied with two to obtain the beam diameter. The average and standard deviation from parallel measurements were calculated.

As the size of SFM limited the *LBAI* at which the measurements could be performed to approximately 8.8°, another measurement method was utilized to capture the effect of *LBAI* on the beam. Steel plate was exposed with the laser at same locations as with the SFM measurements with additional location at the platform corner. The platform height was adjusted so that the surface of the steel plate was at the focus plane of the beam. Interaction time of 1ms and laser power of 40W was used. At each location 3 parallel laser marks were exposed, and the marks were measured with optical microscope. Averages and standard deviations from parallel measurements were calculated. Figure 30 shows the mark diameters which were measured.

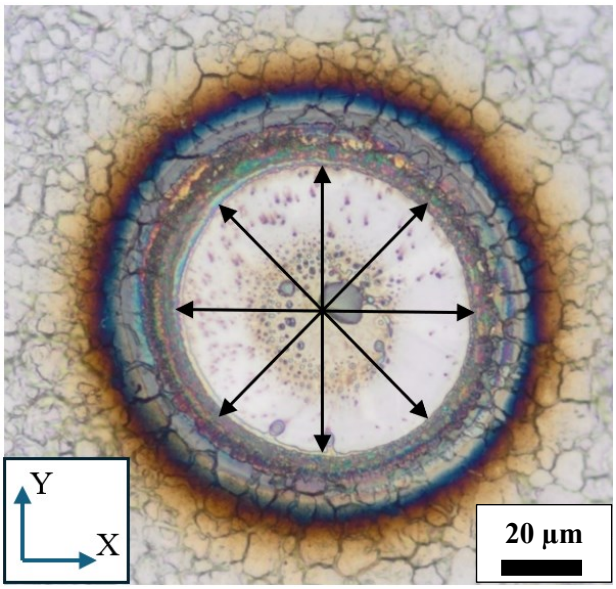


Figure 30 Dimensions that were measured from each laser mark.

As can be seen from Figure 30, the laser mark has a light pit with darker heat affected zone around it. The diameter measurements were taken from the borders of the light pit. Diameter along x- and y-axis was measured as well as along 45° rotated x- and y-axis.

The measurement results for different beam diameters for both measurement methods are presented in relation to the laser beam incidence direction. Different beam diameters in relation to the laser beam direction are illustrated in Figure 31

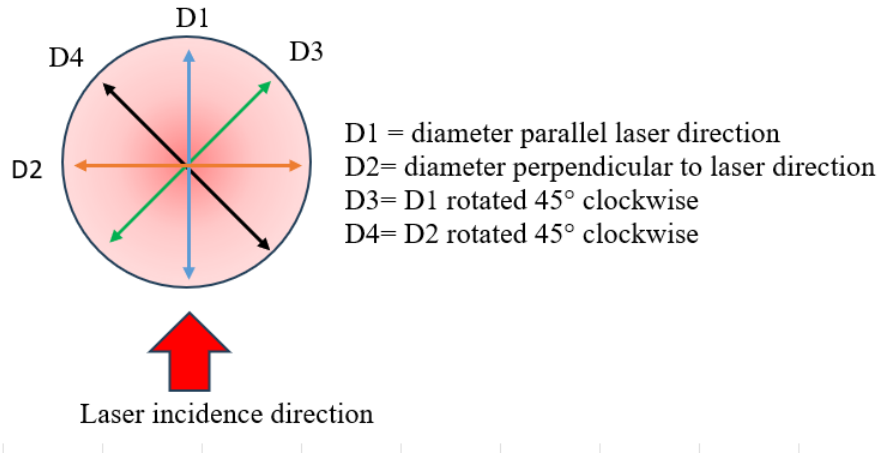


Figure 31 Definition of different beam dimensions D1-D4 in relation to laser beam incidence direction.

As Figure 31 shows, the D1 is the laser spot/mark diameter along the laser incidence direction, which is expected to be the direction where beam is elongated. Thus, it should be the largest diameter while D2 should be the smallest diameter. At *LBAI* of zero, the laser beam does not have incidence direction in relation to the presented beam dimensions, thus the directionality can be ignored for the results at *LBAI* of zero.

## 8.2 Surface roughness study

### 8.2.1 Part design and build platform layout

Three different part geometries were designed to study the surface roughness. Figure 32 shows the test geometries and their dimensions in mm.

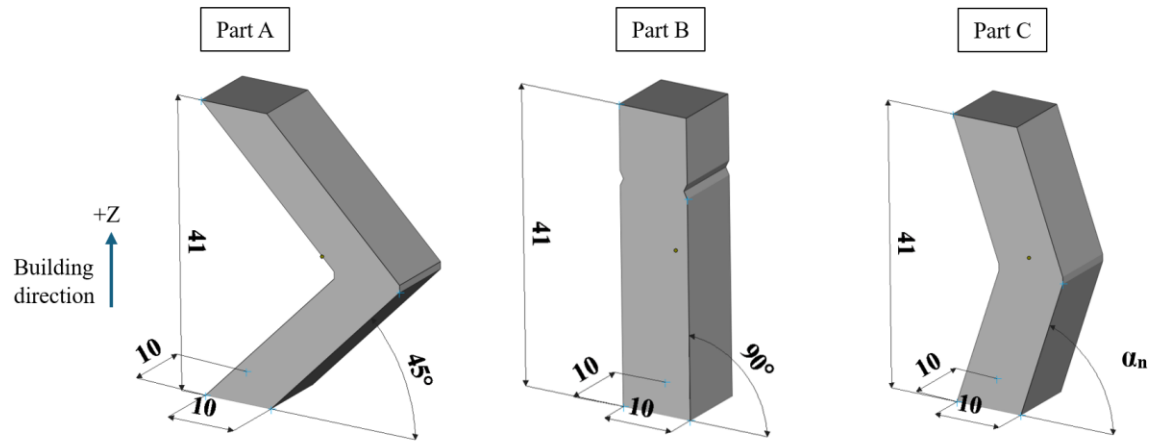


Figure 32 Test parts that were used for investigating the surface roughness (dimensions are in mm, not to scale).

As can be seen from Figure 32, all parts have the same height and the same cross-sectional area (10x10 mm) in horizontal plane. Same cross-sectional area ensures that also the area which is scanned with the laser in each layer is the same for all parts. Thus, the heat input for different test geometries is kept uniform, which is important as increasing the heat input can increase the surface roughness [11]. Part A features inclined surfaces with 45° build angle which are pointed to two opposing directions. Two directions of the surfaces are used to study the effect of laser beam incidence direction on surface roughness. Part B is a simple cuboid to study the surface roughness of vertical surfaces. There are two grooves at the top of part B as originally other test features were intended to be printed on top of the part. The purpose of the grooves was to aid in cutting the top of the part. However, later it was decided that the additional test features on top of part B are excluded from the thesis. Part C features also two inclined surfaces. However, the build angle α of the surfaces is dynamically changed depending on the *LBAI* (i.e. the location of the part in the build platform). The aim of the changing build angle α was to adjust the surface to be more parallel with the laser beam. This is illustrated in Figure 33.

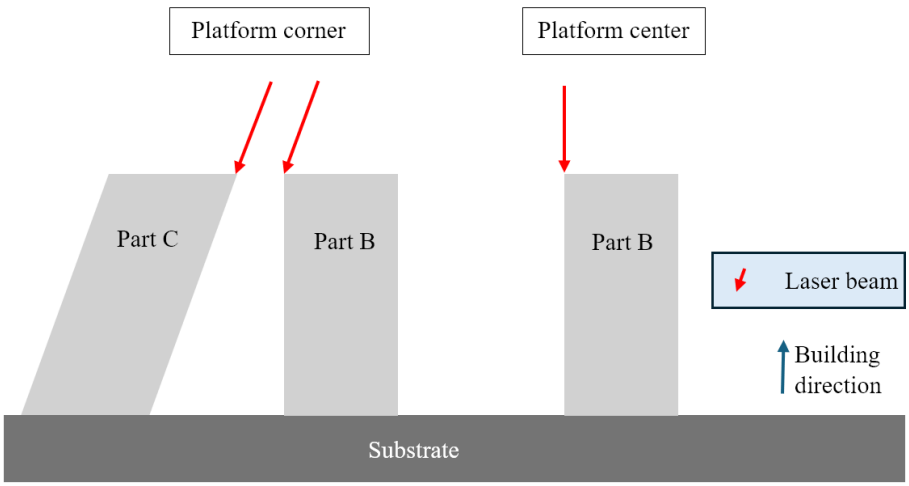


Figure 33 Aim of changing the build angle in part C.

As can be seen from Figure 33, the 90° vertical surface of part B is approximately parallel to the laser beam in the platform center, as the angle of incidence is zero. However, as the angle of incidence increases in the platform corner, the laser beam is not parallel to the 90° surface of part B. Thus, part C was introduced with location dependent build angle α which would

result in nearly parallel laser beam with the part surface. Definition of part C build angles across the platform is described in more detail in appendix 2.

Multiple different surface types can be identified from the test geometries. The surface types are illustrated in Figure 34.

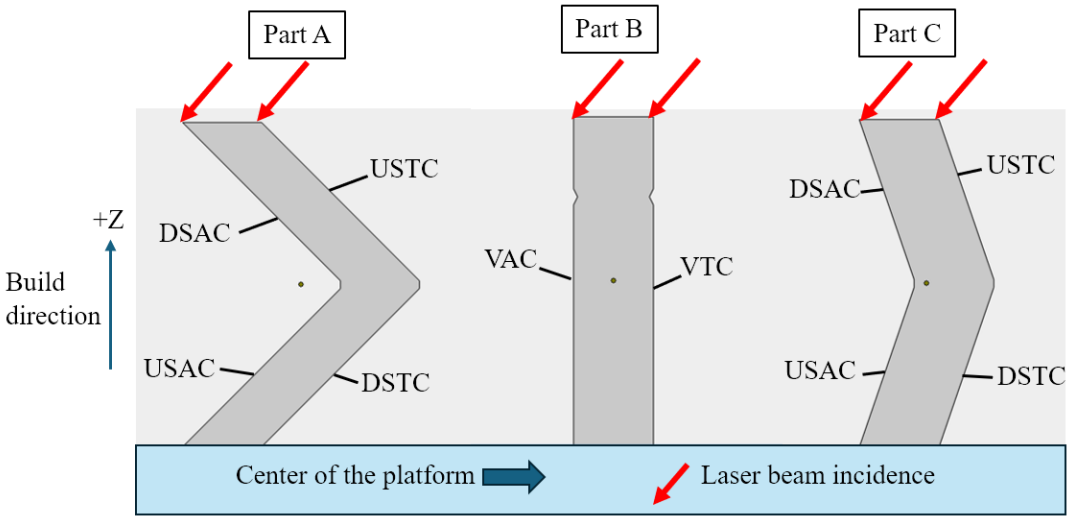


Figure 34 Different surface types that can be identified from the test parts. Note: laser beam incidence is exaggerated for illustrative purposes.

As Figure 34 illustrates, two-fold inclined surface geometries (Part A and Part C) have two types of downskin and upskin surfaces. The top halves of the parts have downskin surfaces that are facing away from the center of the platform (DSAC) and upskin surfaces that are facing towards the center of the platform (USTC). Consequently, the bottom halves of the parts have downskin surface that are facing towards the center of the platform (DSTC) and upskin that is facing away from the center of the platform (USAC). Part B has two vertical surfaces: vertical surface that is facing away from the center of the platform (VAC) and vertical surface that is towards the center of the platform (VTC). Essentially, for each type of surface, there is a reference surface in which the laser beam incidence direction is opposite.

Parts were arranged on the build platform in Materialize Magics print preparation software as illustrated in Figure 35.

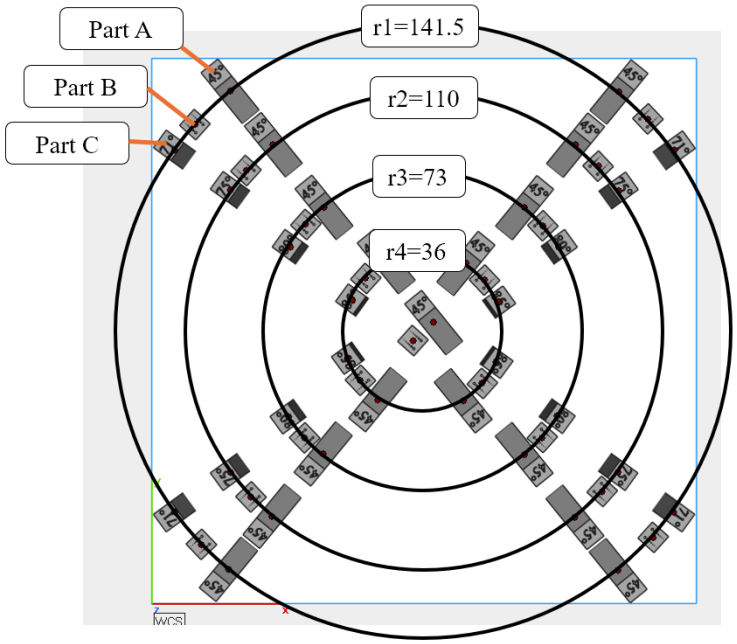


Figure 35 Top view of the layout of surface roughness parts on the build platform. r value indicates the radial distance of the parts from the center in mm.

As can be seen from Figure 35, each type of part was placed on each quadrant of the build platform with four different radial distances from the center, resulting in different *LBAI*s. Additionally, Part A and B were also placed to the middle of the build platform, thus having approximately *LBAI* of zero. *LBAI* for each radial distance was calculated according to equations 4-6, and the calculation results are shown in appendix 1 (Table 8). An additional print job where all the parts were rotated 180° degree around the z-axis was also manufactured. This enabled studying the effect of scan direction on the roughness of the manufactured surfaces. The additional print job is referred as “180° print job” from now on.

### 8.2.2 Part parametrization

Parts were parametrized in EOSPRINT (v 2.15). Standard process parameters optimized by EOS GmbH for IN718 with 40 µm layer height were used. Process parameters are summarized in Table 5 along with the resulting *VED*, which is calculated according to equation 3.

Table 5 Process parameters for surface roughness study.

| **Parameter** | **Value** |
|---|---|
| **Laser power** | 285 W |
| **Scan speed** | 960 mm/s |
| **Hatch spacing** | 0.11 mm |
| **Layer thickness** | 40 µm |
| ***VED*** | 67.47 J/mm$^3$ |
| **Recoater type** | Hard recoater (High speed steel) |
| **Gas** | Argon |
| **Skywriting** | Enabled |
| **Platform** | Stainless steel platform |

Stripe scanning strategy with 67° interlayer rotation and 10 mm stripe width was used. No contour scans were used. Higher surface roughness was expected without contour scans, which should yield more apparent differences between the samples. Additionally, the stripe direction was restricted so that it was approximately against the flow. The allowed range of stripe direction is illustrated in Figure 36 A and the rotation of interlayer stripe direction in Figure 36 B.

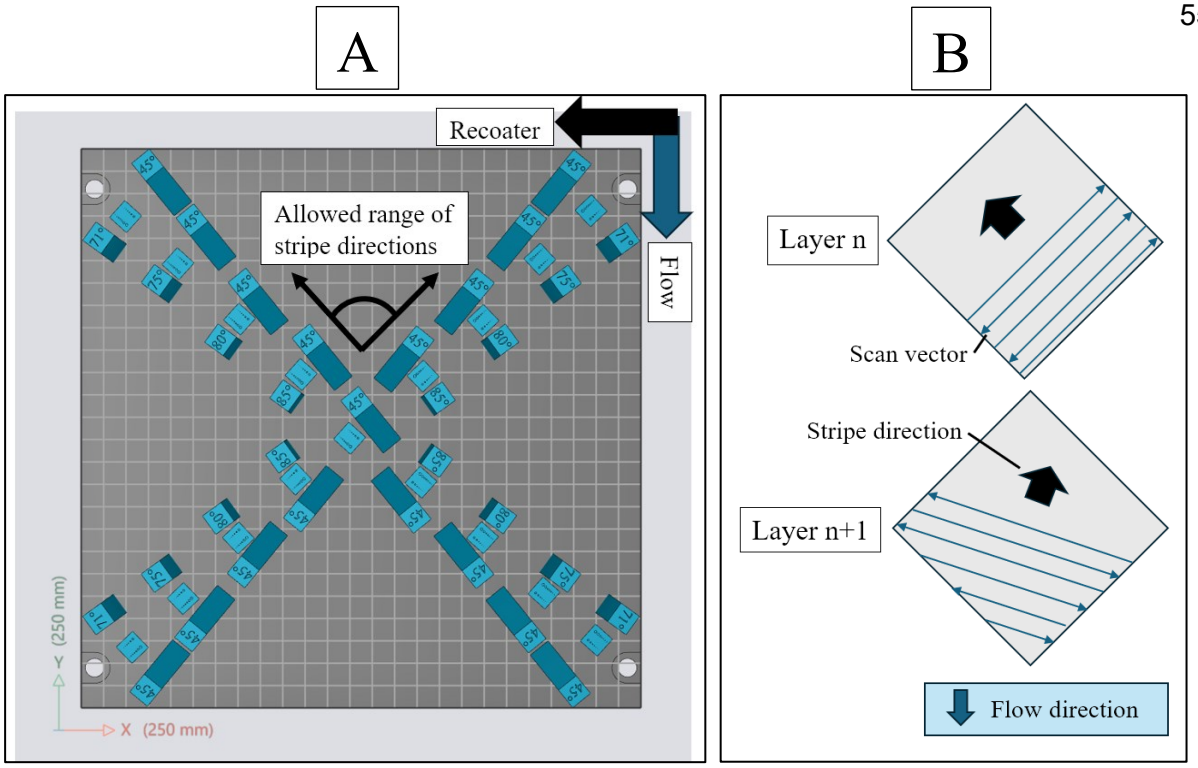


Figure 36 A: Stripe direction range in the used scanning strategy. Only stripes that are scanned against the inert gas flow with certain deviation angle are allowed. B: 67° Interlayer rotation of stripe direction in consecutive layers. Note: the hatch spacing of vectors is not to scale.

### 8.2.3 Surface roughness measurement

AMed parts were cut from the build platform with band saw. Figure 37 shows the manufactured pint job on the build platform (A) and the parts that were taken for further analysis (B) from the print job.

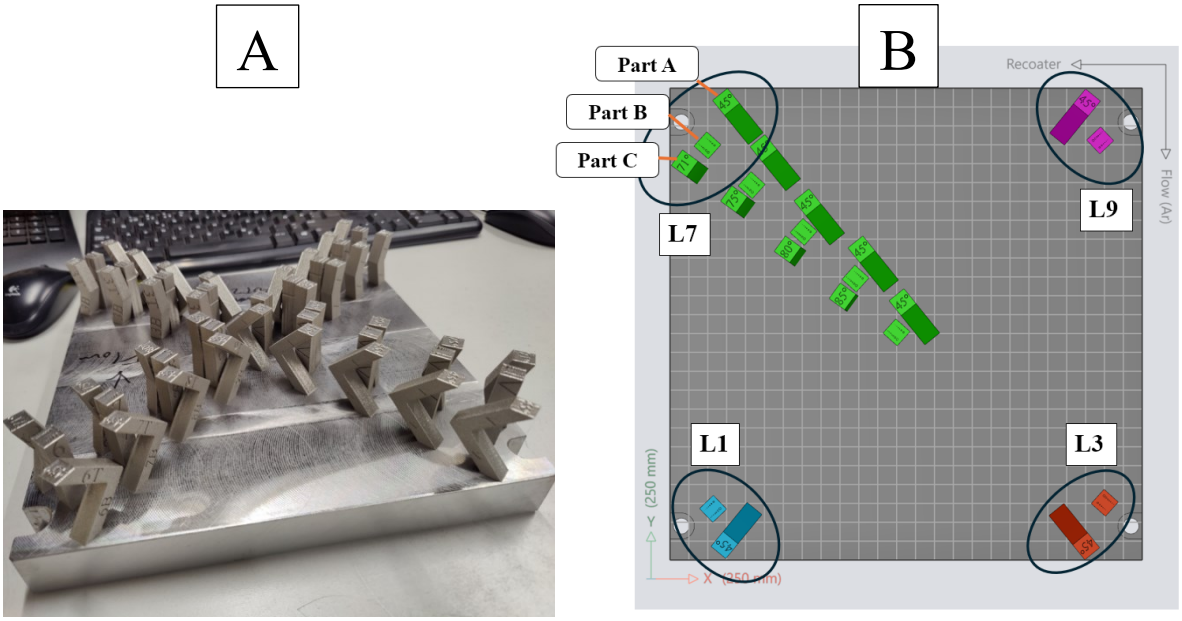


Figure 37 A: manufactured surface roughness print job on the build platform. B: Surface roughness test parts that were analyzed (For illustrative purposes the rest of the parts that were not analyzed are hidden.) Samples at the corners are highlighted and the corresponding platform location is notated with Ln, where n is the location ID number.

As can be seen from Figure 37, all the test parts (green) from top left quadrant were analyzed to study the effect of increasing *LBAI* on surface roughness. Additionally, parts A and B from each corner of the build platform (L1, L3, L7 and L9) were analyzed to study if there are differences across the various platform locations. From the 180° print job only the 45° sample at the center of the build platform was analyzed. The rest of the parts were not analyzed in the scope of this thesis. Part types A and C were cut with disc cutter for easier measurement of the surfaces as illustrated in Figure 38.

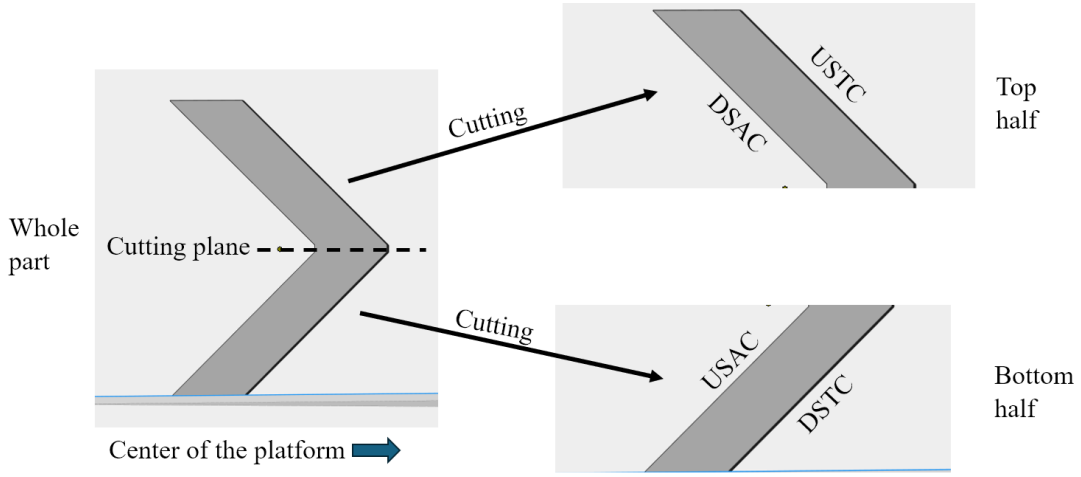


Figure 38 Cutting of two-fold test part A.

Each surface of the samples was imaged by optical profilometry with Alicona InfiniteFocus G5. Each imaged surface resulted in a dataset which contained the topographical data of the whole surface. Areal surface roughness *(Sa)* was determined from each dataset with Alicona MeasureSuite 5.3 software. AMed surfaces can have random irregularities such as un-melted powder particles or melt pool extensions, which can increase the local Ra value significantly (roughness of a profile). Thus, it was anticipated that the areal surface roughness *(Sa)* will capture the surface roughness more accurately. It was observed that some edges of the parts were raised compared to the bulk of the surface. Surface roughness was measured from the bulk of the surface with approximately 1 mm offset from the edges, to exclude the effect of the risen edge, as illustrated in Figure 39.

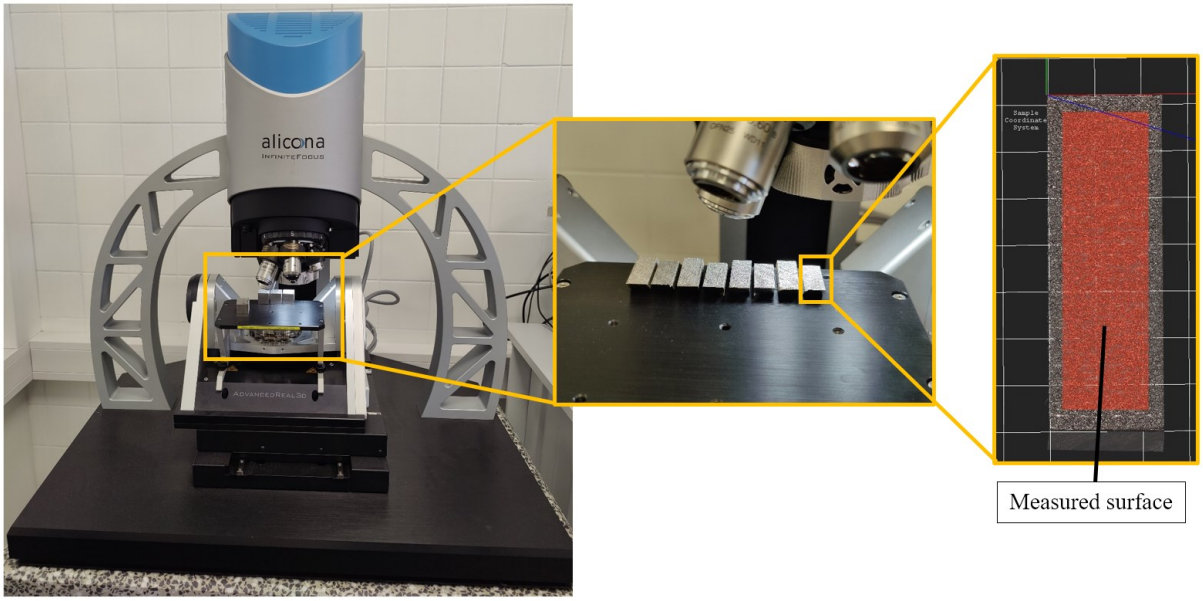


Figure 39 Surface roughness samples on the Alicona InfiniteFocus G5. The rightmost figure shows the dataset of whole surface and the area from which the surface roughness was measured with the software (red area).

## 8.3 Porosity study

### 8.3.1 Part design and build platform layout

Test part used in the porosity study was a 45° chamfered cube, as illustrated in Figure 40.

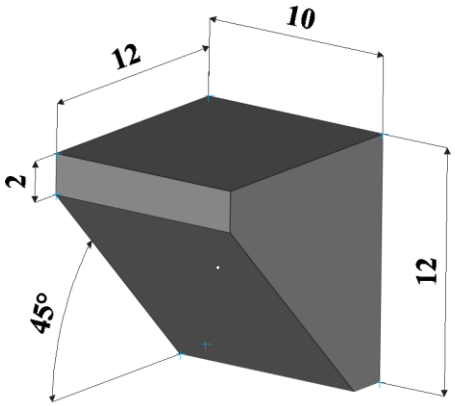


Figure 40 Test part used for the porosity study (dimensions are in mm, not to scale).

Parts were arranged on the build platform similar to the surface roughness test parts, i.e. with same radial distances from the center, resulting in different *LBAI*s. Two sets of print jobs were prepared with the opposite downskin orientations, as illustrated in Figure 41.

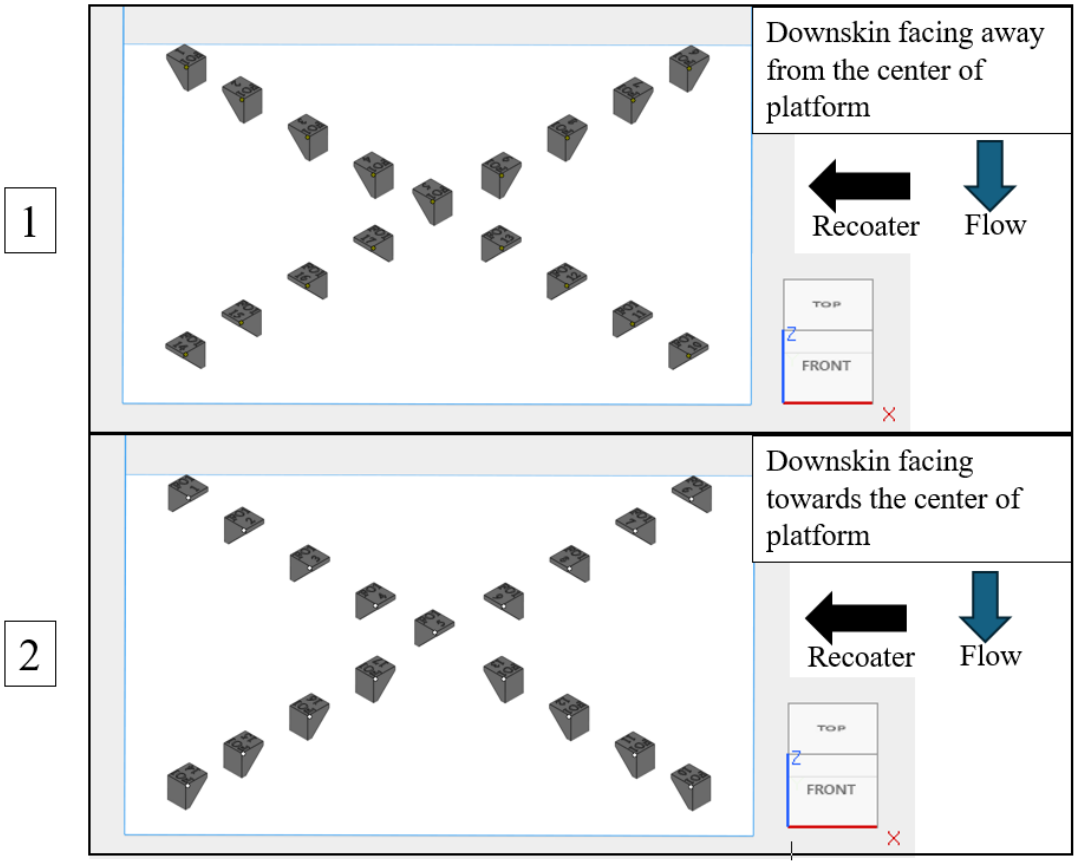


Figure 41 Build platform layout for two porosity print jobs. In layout 1 the downskins are facing away from the center of the platform (DSAC), while in layout 2 the downskin surfaces are facing towards the center of the platform (DSTC).

### 8.3.2 Part parametrization

Parts were parametrized in EOSPRINT (v 2.15) software. Downskin region with lower *VED* was introduced to the parts. Downskin thickness was increased from the standard value to expose resulting porosity more efficiently. Figure 42 illustrates the definition of downskin region.

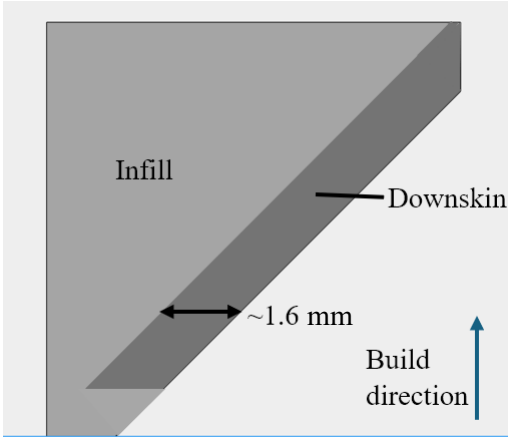


Figure 42 Definition of downskin.

As can be seen from Figure 42, the downskin region has a nominal thickness of 1.6 mm in horizontal plane. Process parameters for infill were the same as for surface roughness parts (as referred in Table 5) except for the stripe width which was set to 1000 mm. This was done to scan each layer in one continuous scan pattern rather than in separate stripes. This approach eliminated the discontinuity caused by interfaces between stripes. It was anticipated that the discontinuity may affect porosity locally. The focus of the porosity study was the effect of *LBAI*; thus, it was essential to eliminate other influential factors that could possibly affect the porosity. The process parameters that were different for the downskin region are shown in Table 6 along with the resulting *VED*.

Table 6 Differing process parameters for the downskin.

| **Parameter** | **Value** |
|---|---|
| **Laser power** | 95 W |
| **Scan speed** | 785 mm/s |
| **Hatch spacing** | 0.10 mm |
| ***VED*** | 30.25 J/mm$^3$ |

The scanning of the layer started from the side which is closer to the center of the platform. When the downskin is towards the center of the platform, it is scanned before the infill and when downskin is away from the center of the platform, infill is scanned first. Figure 43 shows the indicative scan direction for different part orientations.

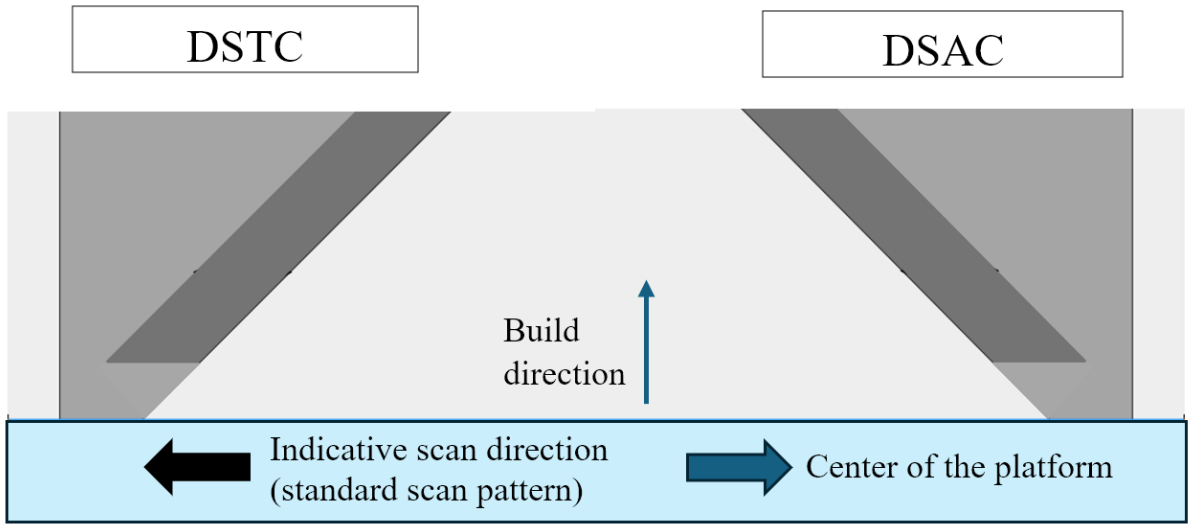


Figure 43 Scan direction for DSTC and DSAC. Note: the scan direction is indicative as it is not actually aligned perfectly along the downskin due to the part orientation on the build platform and the rotation of stripes in consecutive layers.

### 8.3.3 Porosity measurement

The AMed parts were cut from the build platform with a band saw. Figure 44 illustrates the porosity test parts that were analyzed and their *LBAI*s which were calculated according to equations 4-6.

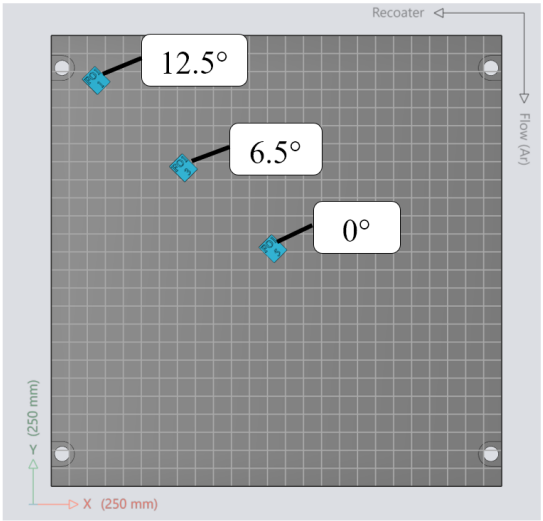


Figure 44 Porosity test parts that were analyzed from both porosity jobs. The rest of the parts that were not analyzed are hidden.

Parts were washed in ultrasound bath to remove any residual powder, after which they were mounted in resin. The mounted samples were ground with #80 silicon carbide (SiC) paper

until approximately 2mm of the material was removed to reveal the subsurface porosity. Rough grinding was followed by fine grinding with #320 SiC paper. Finally, mounted samples were polished in several steps with 9 µm, 3 µm and 1 µm diamond suspension. Polished samples were imaged via optical microscopy to reveal the porosity of the downskin. Image analysis software integrated within the microscope was utilized to define the porosity percentage of the imaged surface. Pores were also classified based on their size in the largest diameter. Size classes were >150 µm and <150 µm.

# 9 Results and discussion

## 9.1 *LBAI* and the laser beam

### 9.1.1 *LBAI* calculations

Figure 45 illustrates the *LBAI* depending on the radial distance from the platform center based on the calculation results. As can be seen from Figure 45, for every 25 mm the *LBAI* increases approximately 2.2° when going further away from the center of the platform. The maximum *LBAI* which is at the platform corners is approximately 15.5°.

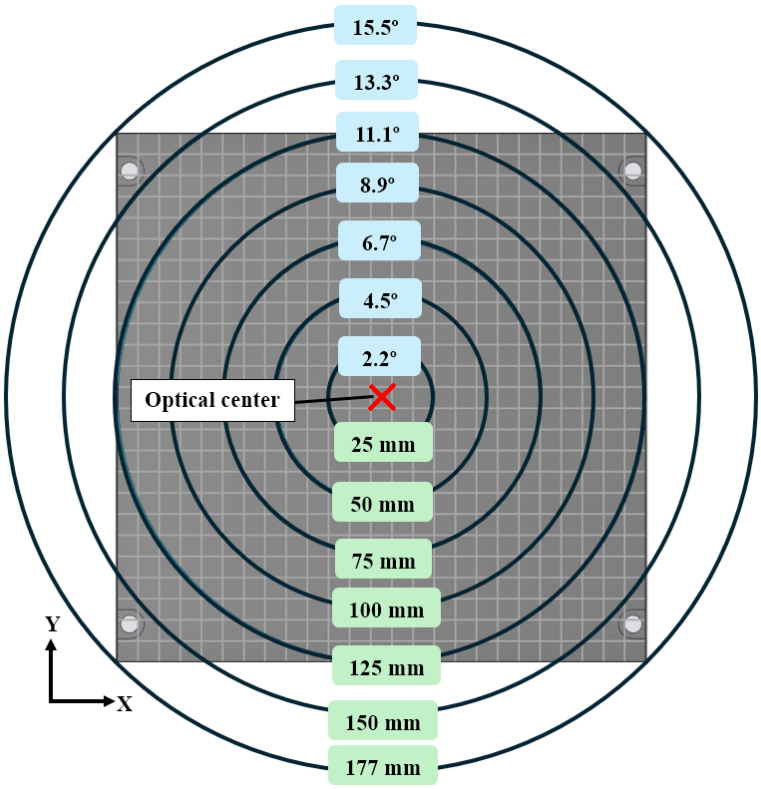


Figure 45 *LBAI* depending on the radial distance from the center of the platform.

### 9.1.2 Laser beam spot characterization

Laser beam spot characterization revealed the effect of *LBAI* on laser beam spot size and the resulting distortion in laser beam-material interaction area. Figure 46 illustrates the beam diameters obtained from SFM measurements.

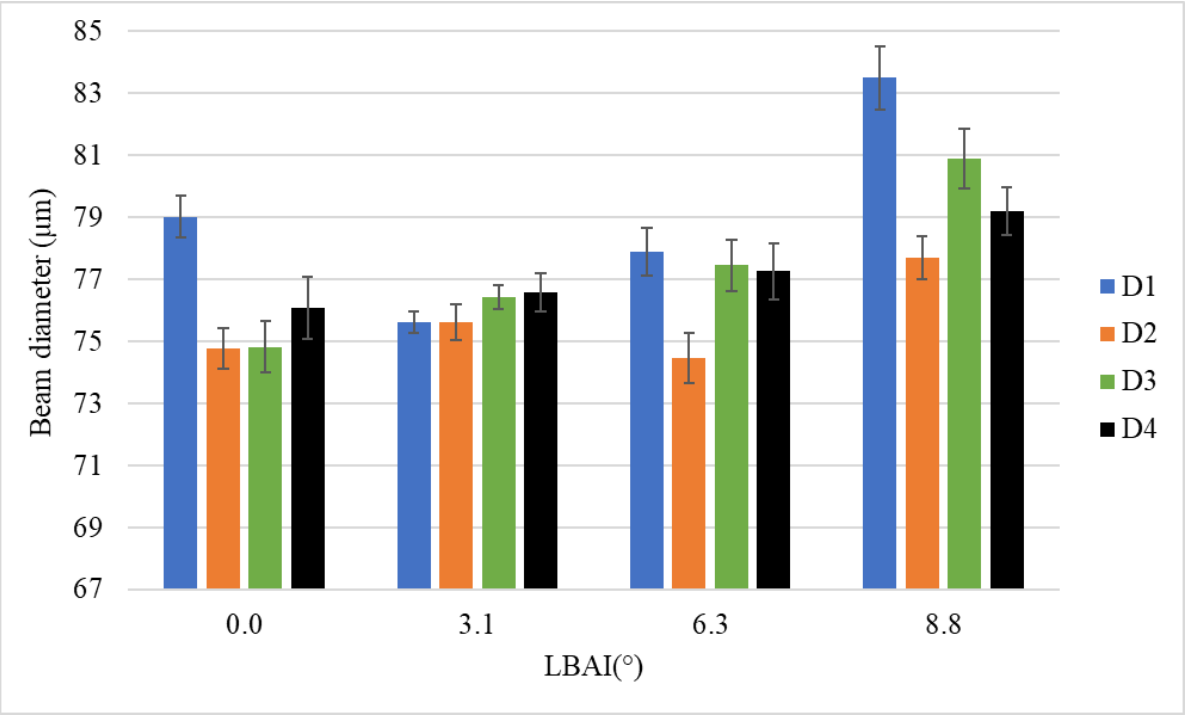


Figure 46 Beam diameter with different *LBAI*s. Error bars show the standard deviation of parallel measurements.

As can be seen from the Figure 46, at zero *LBAI* the beam diameters D2-D4 are similar, which is expected as the beam should be nearly circular at the center. However, D1 is a clear outlier, and it is expected to be a measurement error. Thus, the beam diameter at *LBAI* of zero is approximately 75 µm (average of D2-D4). Beam energy distribution measurement results during periodic maintenance of the used PBF-LB/M machine were reviewed to verify that D1 is a measurement error. Measurement results showed that the beam should be circular at the platform center. There might be debris or stains within the scanning optics or in the optical elements of the measurement device which could disturb the measurement by diffracting the beam. Figure 46 reveals also that when increasing the *LBAI* up to 6.3° there is little increase in the overall beam diameter. There is clear increase in D1 at 8.8°, which was around 83 µm. Moderate increase for D3 (81 µm) and D4 (79 µm) was observed, while D2 (78 µm) increased slightly. A slight increase in D2 might be due to small errors in mechanical levelling of the platform. The results indicate that there is elongation of the laser beam spot along the laser beam incidence direction up to 11% (from 75 µm to 83 µm) at *LBAI* of 8.8°.

Observations comply with the findings of Fathi-Hafsejani et al. [14], who found that the beam spot elongated along the laser beam incidence direction. However, the exact amount of elongation is not comparable as the used PBF-LB/M system in the studies are different.

Optical laser mark measurement results show distortion of the laser beam-material interaction area at the corner of the platform. Figure 47 illustrates the optical measurement results of laser marks with different *LBAI*s.

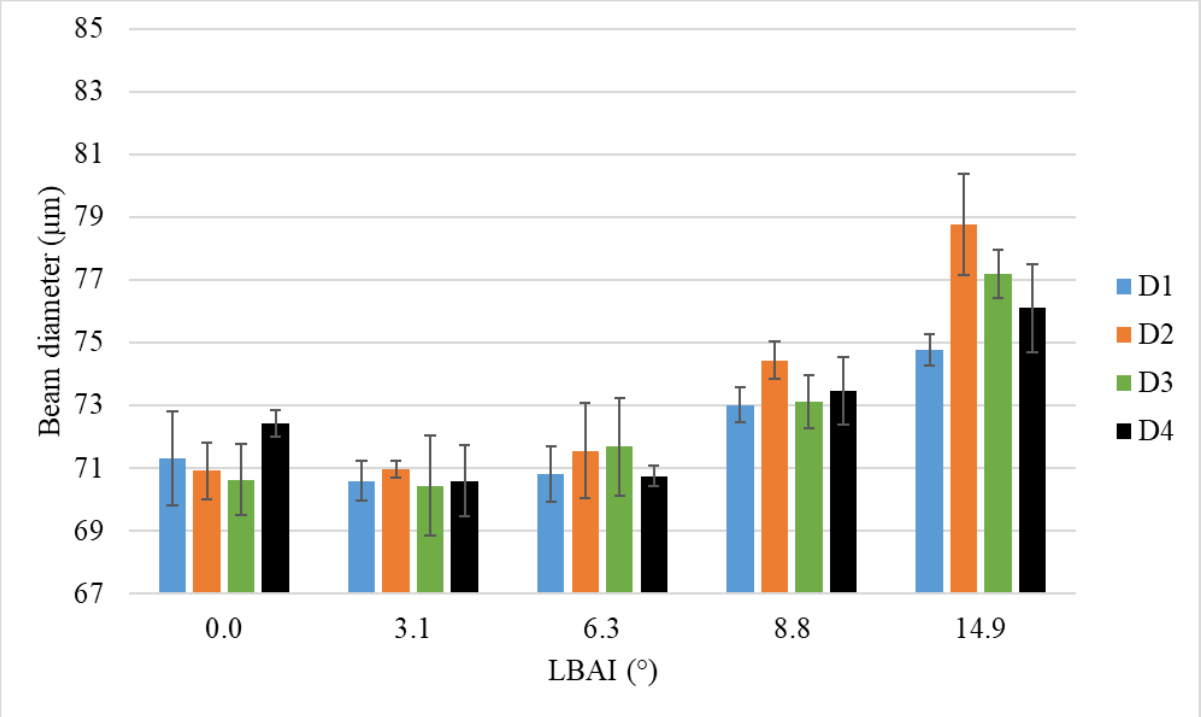


Figure 47 Optically measured laser mark diameters with different *LBAI*s. Error bars show the standard deviation of parallel measurements.

As Figure 47 illustrates, the overall size of the laser marks is practically the same up to *LBAI* of 6.3°, which complies with the findings from SFM measurements. At 8.8° the overall diameter of the laser mark has increased slightly while there is no distinct difference between different diameters (D1-D4). At the platform corner with *LBAI* of 14.9° the D2-D4 of the laser mark increased significantly, while there was only subtle increase in D1. The observation is interesting and counterintuitive as the D1 was expected to be the largest as previously shown in SFM measurements and the literature [14]. Fathi-Hafsejani et al. [14] used much smaller interaction time of 2020 ns and 90W laser power to create the laser marks, which resulted in discolored laser footprint without melting the base material. Comparably the laser marks in the present work indicated melting of the base material during the laser material interaction, as the marks featured distinctive pits in the middle. Further investigations

would be required to fully understand the contradicting results. However, the laser mark measurement results show that increasing *LBAI* beyond 6.3° causes changes in the beam spot as mark diameters were skewed. It should be also noted that the optical measurements of the laser marks do not directly measure the beam, thus clear conclusions about the spot shape cannot be made. Additionally, there might be small differences in the beam shape between the SFM measurements and the optical laser mark measurements, because the experiments were conducted in different sides of the platform. There might be aberrations in the F-theta lens which can lead to differences in the beam shape across the scan field.

Based on the previous SFM measurements it is concluded that the laser beam can be elongated up to 11% with *LBAI* of 8.8°. No exact values about beam elongation beyond *LBAI* of 8.8° could be concluded. However, it is expected that increasing the *LBAI* further will also elongate the spot. Laser mark measurements showed that the laser material interaction area can become distorted near the platform corner.

## 9.2 Surface roughness study

### 9.2.1 Effect of *LBAI* on surface roughness

Surface roughness measurement results reveal the effect of increased *LBAI* on surface roughness of different surfaces. Figure 48 shows the roughness of surfaces from top half of part A.

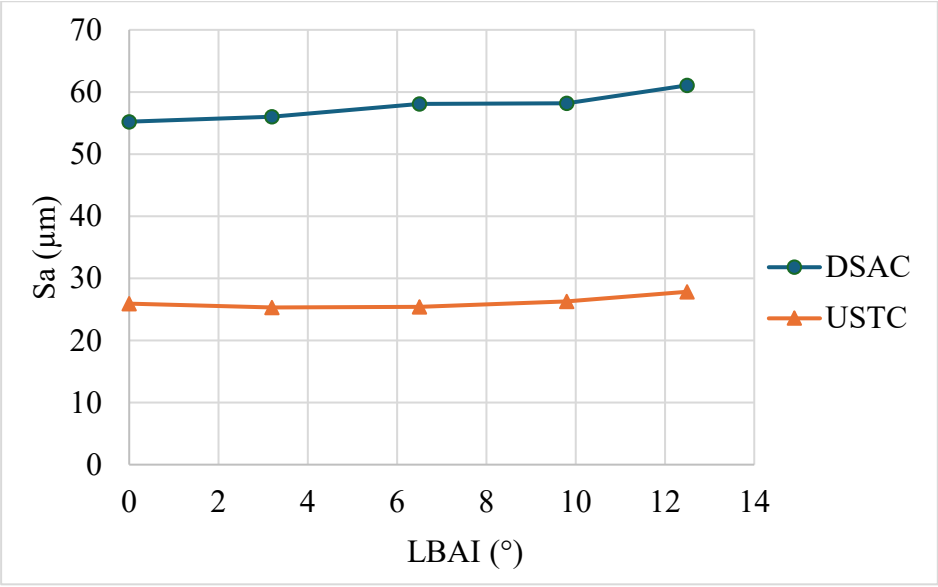


Figure 48 Surface roughness of downskin and upskin of the top half of Part A with different *LBAI*s.

As it can be seen from Figure 48, the surface roughness of DSAC increases from 55 µm to 61 µm when *LBAI* is increased up to 12.5º. Observations comply with the results of Kleszczynski et al. [10], who studied 45° downskin surfaces manufactured from IN718 with similar PBF-LB/M machine. It was found that DSAC surface roughness increased approximately 10-30 µm (Rz) when going from the platform center to the platform corner [10]. However, their values were not directly comparable due to different surface roughness measurement method and process parameters [10].

Figure 48 also shows that surface roughness of upskin is not affected by increasing *LBAI*, as it practically stays the same (approx. 26 µm) throughout the increased *LBAI* range. Surface roughness of the upskin is much lower compared to the downskin, which was expected based on the literature. Similar observations were made by Zhou et al. [51] who characterized surface roughness of 45° inclined IN718 surfaces. In their study, numerous process parameter combinations were used and downskin surface roughness *(Ra)* was approximately 10-50 µm higher compared to upskin [51].

The increasing surface roughness for DSAC can be explained by the tilted laser beam penetrating more severely into the loose powder. Figure 49 illustrates the *LBAI* in relation to DSAC of the top half of the part.

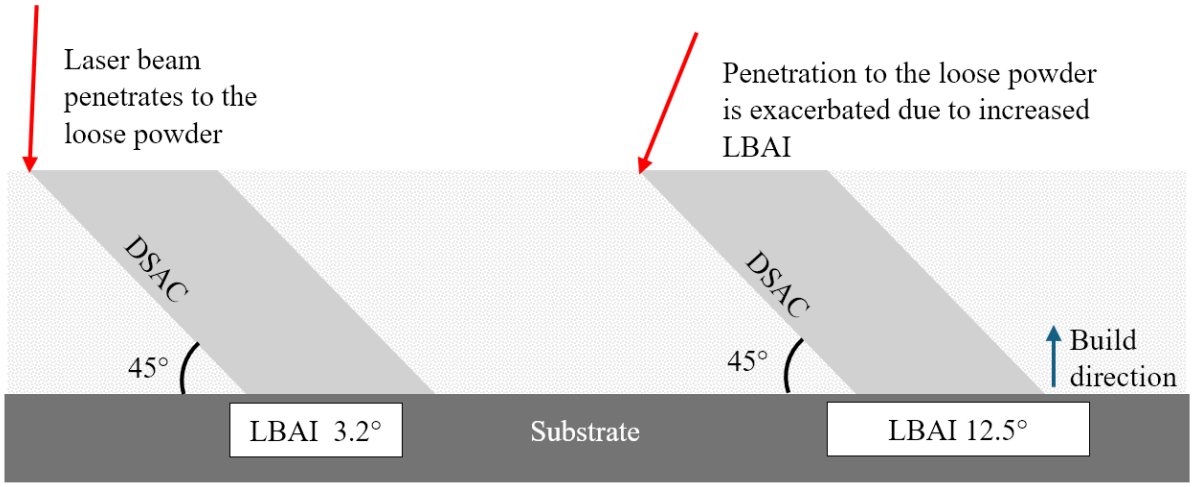


Figure 49 *LBAI* in relation to the DSAC of top half of part A.

As can be seen from Figure 49, laser beam is directed to the loose powder with both *LBAI*s during fabrication of downskin. However, increasing the *LBAI* directs the beam more towards the loose powder. This may lead to melt pool extending further into the powder bed, which

causes increased surface roughness. Similar effect is not observed with the upskin, as the laser beam is directed towards previously solidified material, which explains why upskin roughness did not increase while *LBAI* was increased.

Figure 50 shows the roughness of surfaces from bottom half of part A, i.e. when the surfaces are oriented the opposite direction compared to the top half.

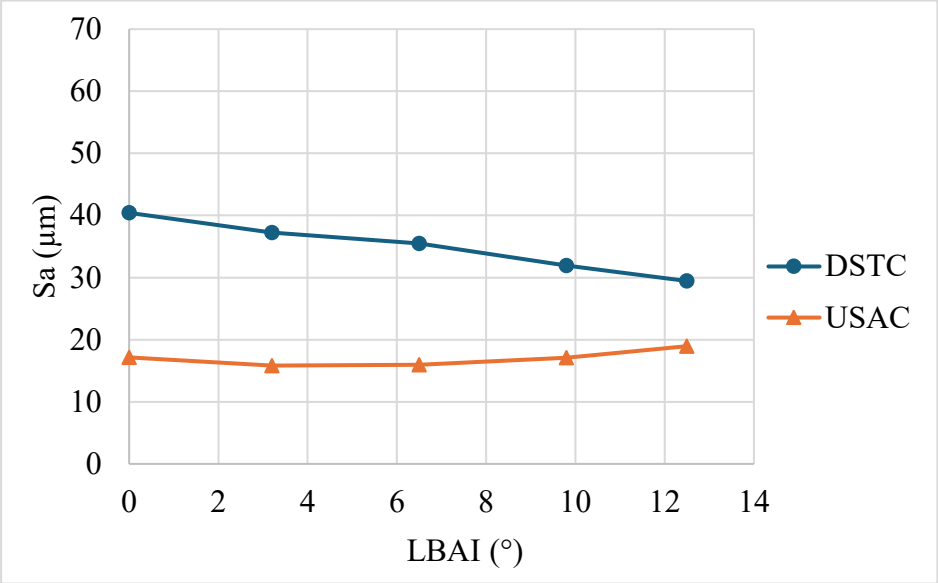


Figure 50 Surface roughness of downskin and upskin of the bottom half of Part A with different *LBAI*s.

As Figure 50 shows, DSTC surface roughness decreases approx. from 40 µm to 30 µm while *LBAI* is increased. This observation is also similar to findings from Kleszczynski et al. [10]. Upskin surface roughness shows a slight U-shaped curve, but no clear trend is visible while *LBAI* is increased. The surface roughness of upskin ranges from 16 µm to 17 µm. These minor variations in upskin surface roughness may be due to other location dependent factors, such as variation in inert gas flow condition across the platform. Figure 51 illustrates the *LBAI* in relation to the surfaces of the bottom half of the part.

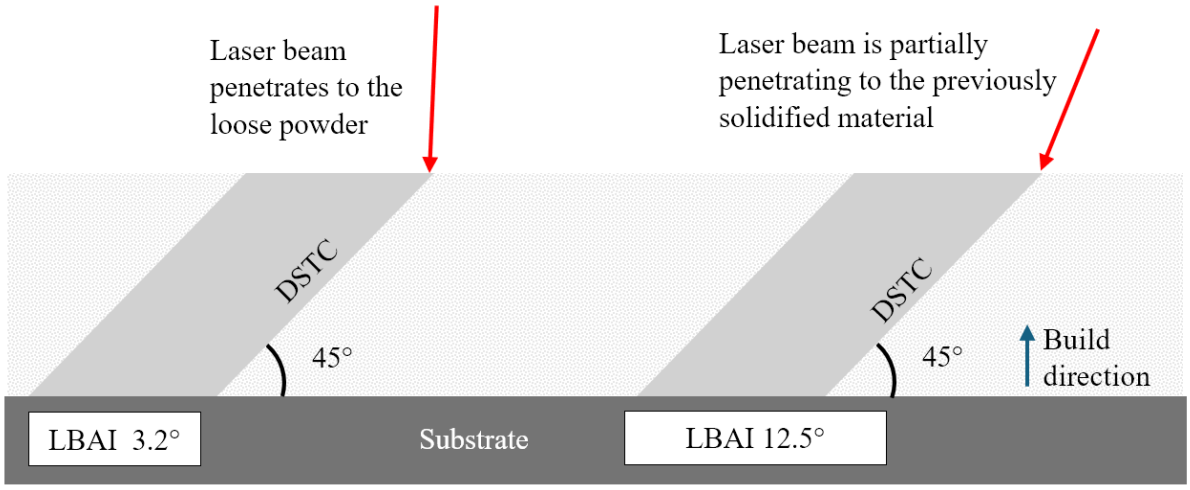


Figure 51 *LBAI* in relation to the downskin surface of bottom half of part A.

As can be observed from Figure 51, now the increasing *LBAI* directs the laser beam to be more parallel with the downskin surface. This may lead to lesser melt pool extensions as the melt pool partially penetrates to the previously solidified material rather than to the loose powder, which would explain the reduction in surface roughness for DSTC surface while *LBAI* is increased.

For 90° vertical surfaces, the effect of *LBAI* on surface roughness is similar compared to 45° surfaces. Figure 52 shows the surface roughness of vertical surfaces of part B.

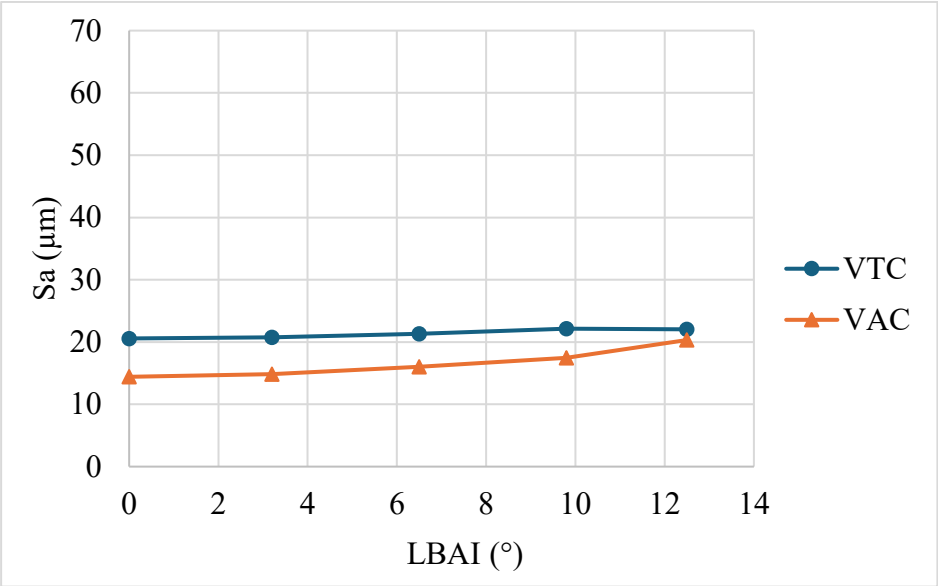


Figure 52 Surface roughness of vertical surfaces of part B with different *LBAI*s.

As Figure 52 shows, surface roughness of VAC surface increases from approximately 14 µm to 20 µm. The increase can be explained by similar effect of tilted laser beam as in top half of part A (Figure 49). Surface roughness of vertical VTC surface remains the same while *LBAI* is increased. Interestingly, VTC surface roughness is distinctly higher than the VAC surface at zero *LBAI*, which should not yield melt pool extension induced surface roughness. VTC surface is located at the side of the flow outlet, i.e. where the inert gas is flowing. It could be possible that the spatter particles land on the side of VTC more likely due to the gas flow direction, which could cause increased surface roughness. However, further studies are needed to conclude why VTC has clearly higher surface roughness than VAC.

It was observed that by aligning the part to be more parallel with the laser beam (Part C), surface roughness can be improved compared to vertical surfaces (Part B). Figure 53 shows the surface roughness of vertical VTC surfaces of part B and the corresponding DSTC surfaces of part C that had *LBAI* dependent build angle.

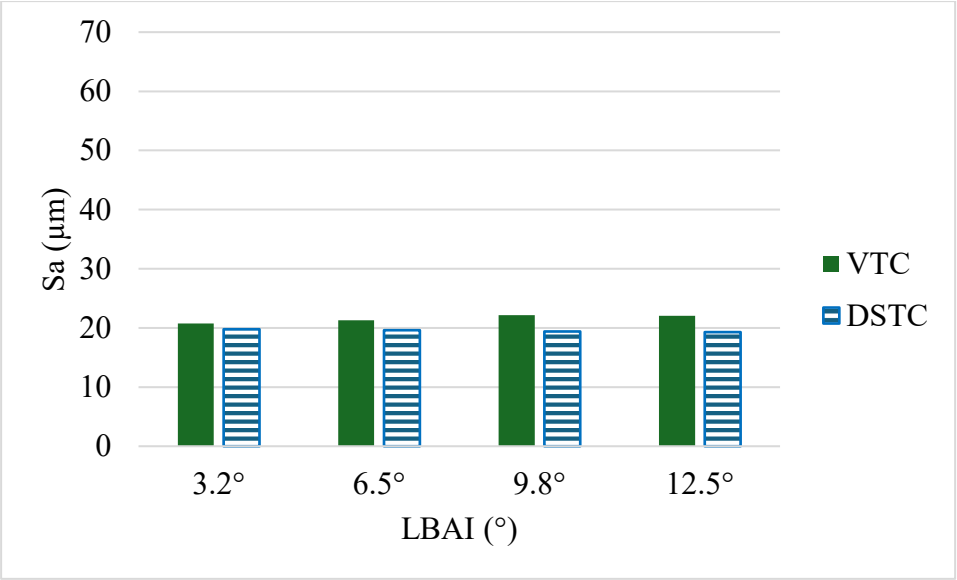


Figure 53 Surface roughness of VTC surface (Part B) and DSTC surface (Part C/bottom half) that had dynamically changing build angle to tilt the surface to be nearly parallel with the laser beam.

As Figure 53 reveals, VTC and DSTC surfaces have similar surface roughness across the *LBAI* range. Neither of the surfaces are effectively subject to the melt pool extension effect due to their orientation. For both surfaces the inclined laser beam is directed towards previously solidified material. Figure 54 shows the surface roughness results for the corresponding surfaces when the surface orientation is the opposite.

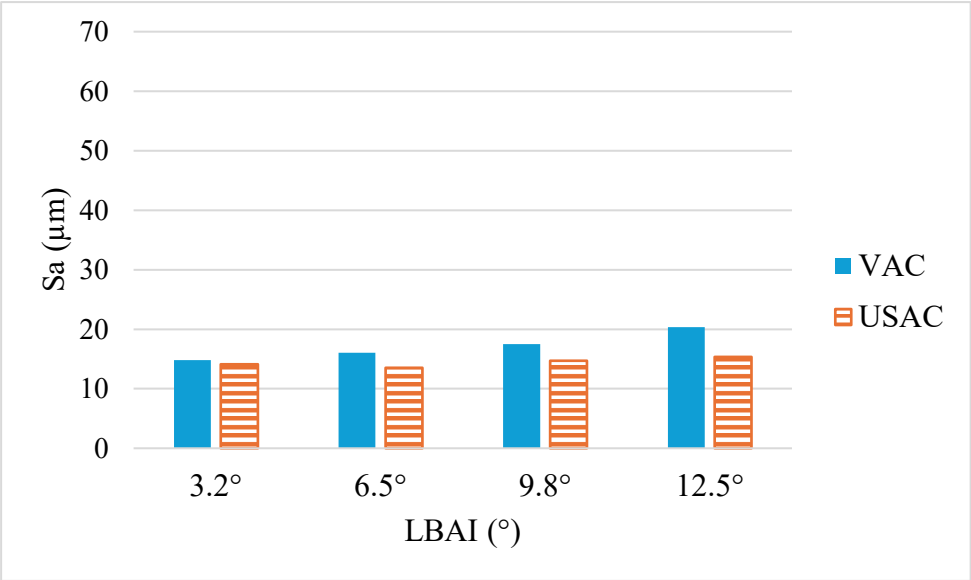


Figure 54 Surface roughness of VAC surface (Part B) and USAC surface (Part C/bottom half) that had dynamically changing build angle to tilt the surface to be nearly parallel with the laser beam.

As can be observed from Figure 54, now there is a distinct difference in surface roughness between VAC and inclined USAC surface. The inclined surface of the bottom half of part C outperforms the VAC in terms of surface roughness. It is presumed that while VAC surface is subject to melt pool extension effect, this is not the case for USAC of part C. The melt pool extension effect is dispelled as the surface is aligned with the laser beam, which results in melt pools extending to previously solidified material, as illustrated in Figure 55. These observations emphasize the effect of *LBAI* on surface roughness, as the inclined surfaces are subject to additional surface roughness inducing effects which are not present for the vertical surfaces. These effects include the staircase effect [13] [51] and localized heat accumulation for downskin surfaces [56] [53]. Thus, it is demonstrated that *LBAI* is a notable source of surface roughness in PBF-LB/M.

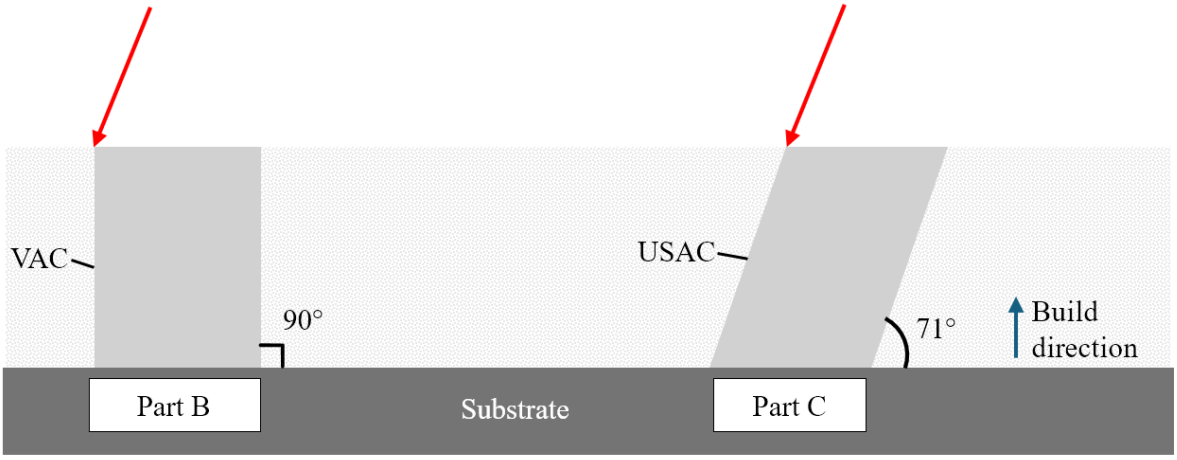


Figure 55 *LBAI* in relation to the VAC surface of part B and USAC surface of part C at the platform corner.

### 9.2.2 Effect of part location on the platform

Measurement results from different locations at the platform corners (*LBAI* of 12.5°) revealed other location dependent variations in the surface roughness in addition to *LBAI*. Figure 56 shows the roughness of different surfaces at different platform locations, where the *LBAI* is the same.

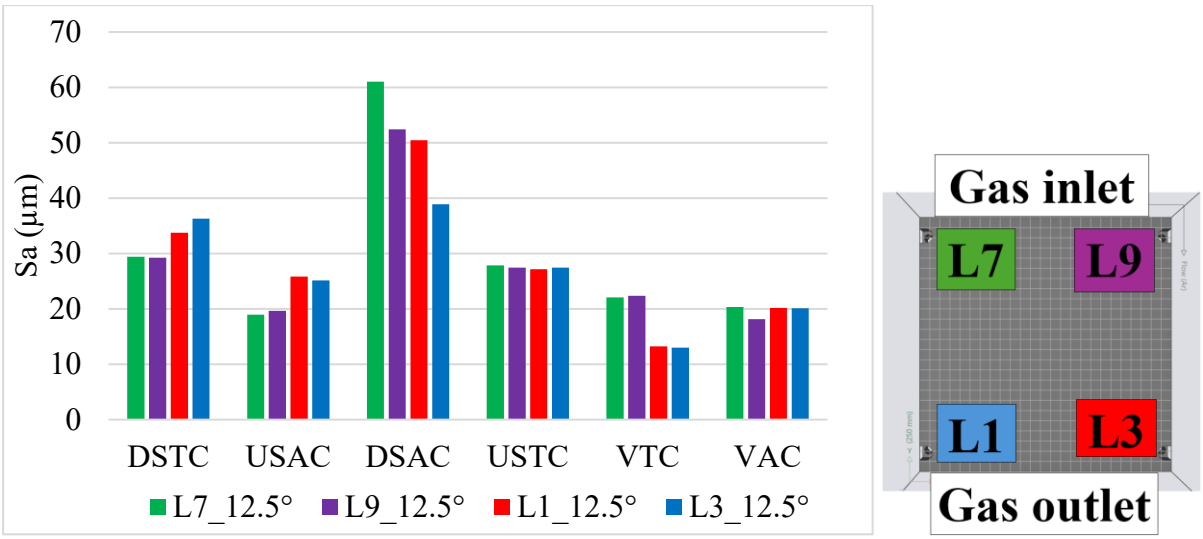


Figure 56 Surface roughness of different surfaces from each part group and the corresponding platform locations for each group.

As can be seen from Figure 56, surface roughness for USTC and VAC surfaces does not vary significantly depending on the platform location. Location dependent variations for other types of surfaces can be observed. Highest location dependent surface roughness variation can be observed for DSAC surfaces. Interestingly, similarities in surface roughness can be observed depending on is the part located at the side of the gas outlet (L1 and L3) or gas inlet (L7 and L9). Ali et al. [70] reported higher spatter particle concentrations on the powder bed near the gas outlet, which resulted in higher surface roughness in AMed parts. DSTC and USAC surfaces near the gas outlet (L1 and L3) have higher surface roughness than near the gas inlet (L7 and L9), which complies with the findings of Ali et al. [70]. Interestingly, VTC surfaces near gas inlet (L7 and L9) have higher surface roughness than near the gas outlet (L1 and L3), which is counterintuitive with the previous observations. The parts at L1 and L3 are oriented the opposite compared to parts at L7 and L9, which results in the opposite scan direction in relation to the measured surfaces. This could cause different heat gradient in the part, which could result in different surface roughness.

Effect of stripe scanning direction can be seen when the surface roughness results of 45° surfaces from the original print job to the 180° print job is compared. Figure 57 illustrates the roughness of different 45° surfaces in relation to general direction of stripes from both jobs at the center of the build platform.

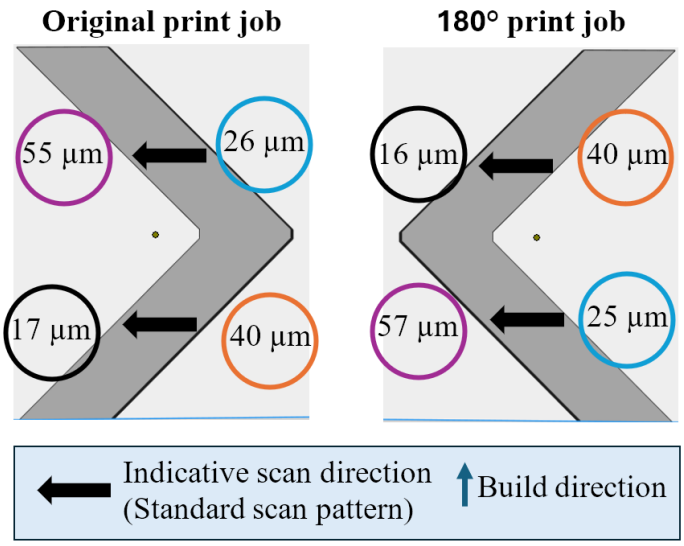


Figure 57 Surface roughness *(Sa)* of 45° surfaces from original and 180° print job. Note: the scan direction is indicative as it is not actually aligned perfectly as illustrated due to the part orientation on the build platform and the rotation of stripes in consecutive layers.

As can be seen from Figure 57, the surface roughness of different surfaces is virtually the same in both print jobs when the surfaces are related to the scan direction. The downskin at the end of the scanned stripes (purple) has considerably higher surface roughness than the downskin at the start of the scanned stripe (orange). For upskin surface the surface roughness in relation to scan direction is the opposite; upskin at the start of the stripe (blue) has higher surface roughness than upskin at the end of the stripe (black). It is anticipated that the heat builds up towards the end of the scanned stripe as the cumulative laser-material interaction time increases during the scanning of a layer. From the literature it was concluded that the downskin is prone to heat accumulation due to limited heat conduction as there is smaller volume of material where the heat can conduct compared to upskin. Heat accumulation may be exacerbated in downskin at the end of the stripe, which further promotes formation of melt pool extensions and increases surface roughness. Interestingly, the surface roughness of upskin is better at the end of the scanned stripe. Surface roughness of DSTC and USAC at L1 and L3 (Figure 56) were higher than at L7 and L9. At L1 and L3 the general scan direction was from the upskin to the downskin, which is considered as bad direction based on previous observations, which could explain the higher surface roughness. However, the observations about relation of surface roughness and scan direction requires further in-depth study to validate the hypothesis.

Observations from the surface roughness study demonstrate the complexity of the surface roughness formation in parts manufactured via PBF-LB/M. While previously it was demonstrated that increasing *LBAI* affects the surface roughness of various surface types, yet there remain other influential factors in the used test setup which led to location dependent variations in surface roughness. It is anticipated that stripe direction has also a notable effect in surface roughness formation. Other location dependent phenomena can also affect the surface roughness, such as different spatter particle concentration on the powder bed or different flow conditions.

## 9.3 Porosity study

### 9.3.1 Effect of *LBAI* on porosity of downskin

Micrographs of the samples revealed that the porosity was concentrated in the downskin region in all the samples. Micrographs of all porosity samples can be seen in appendix 3. Figure 58 shows the micrograph of DSTC sample at 0° *LBAI*.

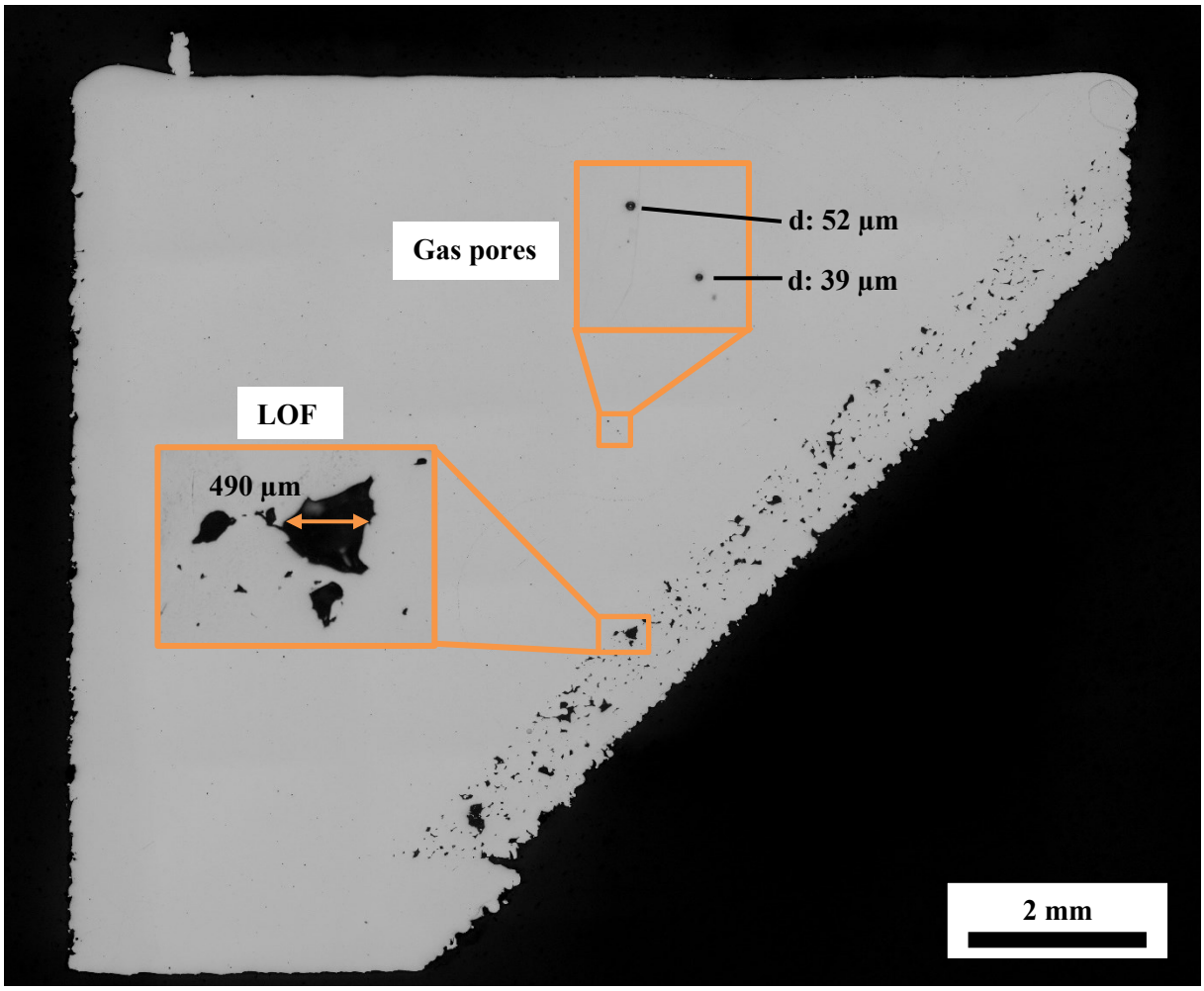


Figure 58 Micrograph of the DSTC sample at *LBAI* of 0° with magnified images of gas pores and LOF.

As can be seen from Figure 58, large irregular pores exist in large quantities at the downskin, while infill is almost free of porosity, with just small number of spherical gas pores. Large irregular pores indicate LOF, which can be explained by the lower *VED* in the downskin. Further analysis of porosity percentage by pore size complies with the visual observations as illustrated in Figure 59.

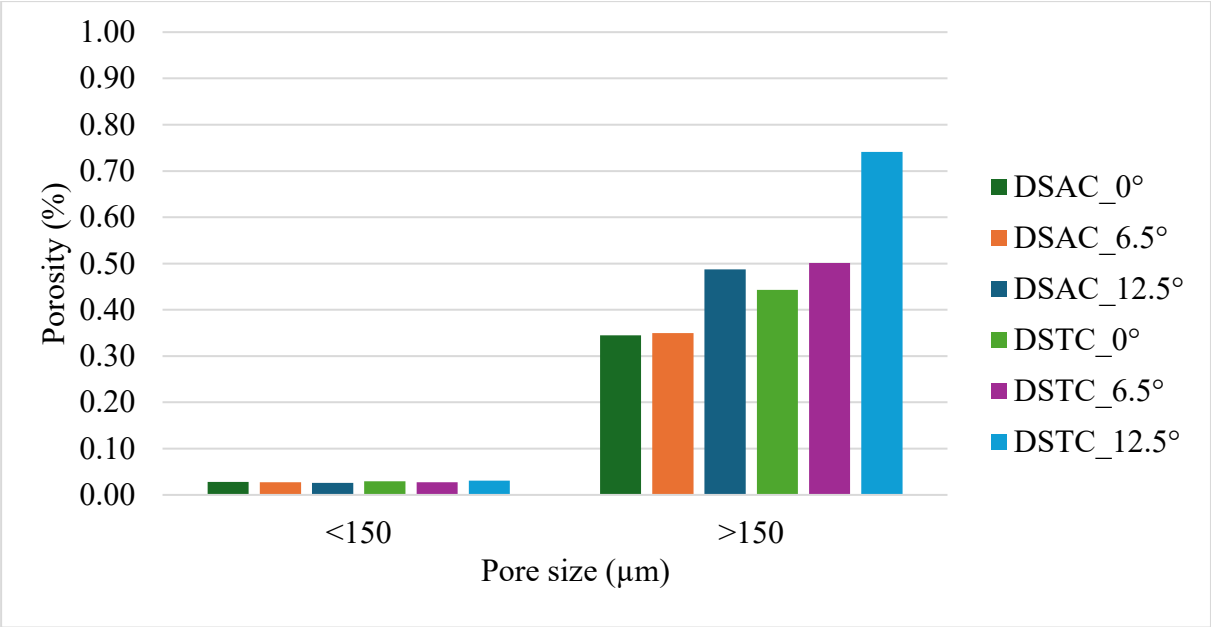


Figure 59 Porosity percentage for different pore sizes at different *LBAI*s and part orientations.

As Figure 59 shows, porosity percentage is high for >150 µm pores, while for <150 µm pores the porosity percentage is negligible (approx. 0.03% for each sample). Additionally, porosity percentage of <150 µm pores is unaffected by *LBAI* or part orientation. Based on these observations, it can be stated that porosity exists almost exclusively in the downskin in the form of large LOF pores. Figure 60 shows the total porosity percentage with different *LBAI*s for both part orientations.

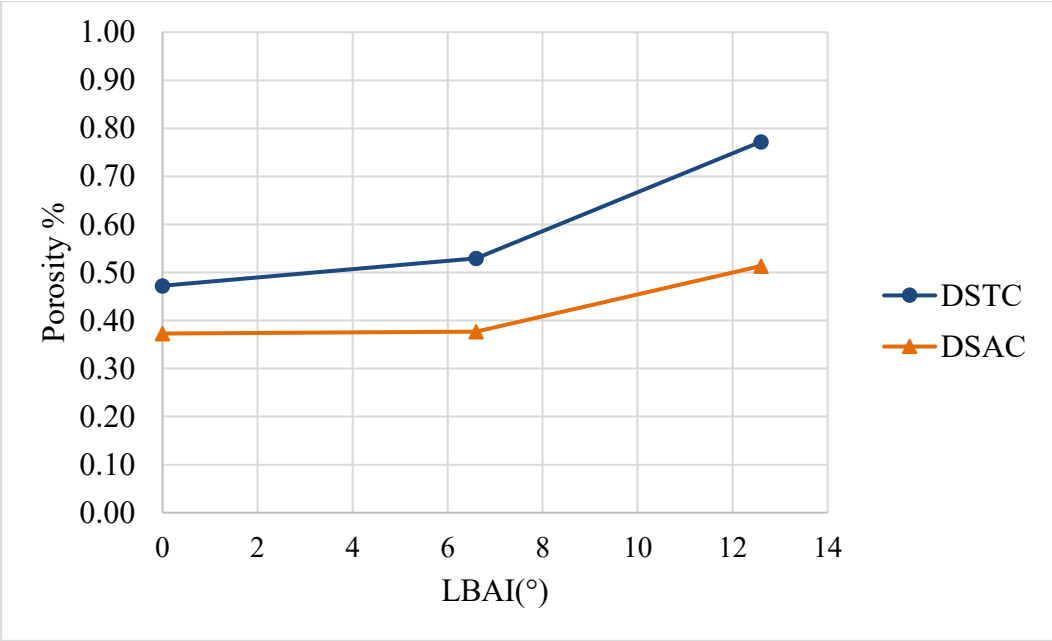


Figure 60 Effect of *LBAI* on porosity percentage.

As Figure 60 shows, the porosity percentage remains almost unaffected for both part orientations up to *LBAI* of 6.5°. The porosity has notably increased for both part orientations at *LBAI* of 12.5°. The findings comply with the laser beam spot characterization results, as it was found that beam spot was practically unaffected up to *LBAI* of 6.3°. It is anticipated that the energy density of the beam at *LBAI* of 12.5° is reduced as the spot radius has increased. The loss of energy density reduces the ability to completely melt the powder, which causes increased amount of LOF. Similar conclusions were made by Fathi-Hafshejani et al. [14], who reported increased LOF porosity for AMed AlSi10Mg, while distance from the platform center (i.e. *LBAI*) was increased.

### 9.3.2 Effect of downskin orientation

Figure 60 also reveals that DSAC has lower porosity percentage compared to DSTC. It is anticipated that this is a result of heat building towards the end of the scanned stripe as proposed in surface roughness study. This causes “healing” effect of LOF, where LOF pores are closed during re-melting of the material. Figure 61 illustrates this hypothesis with both part orientations.

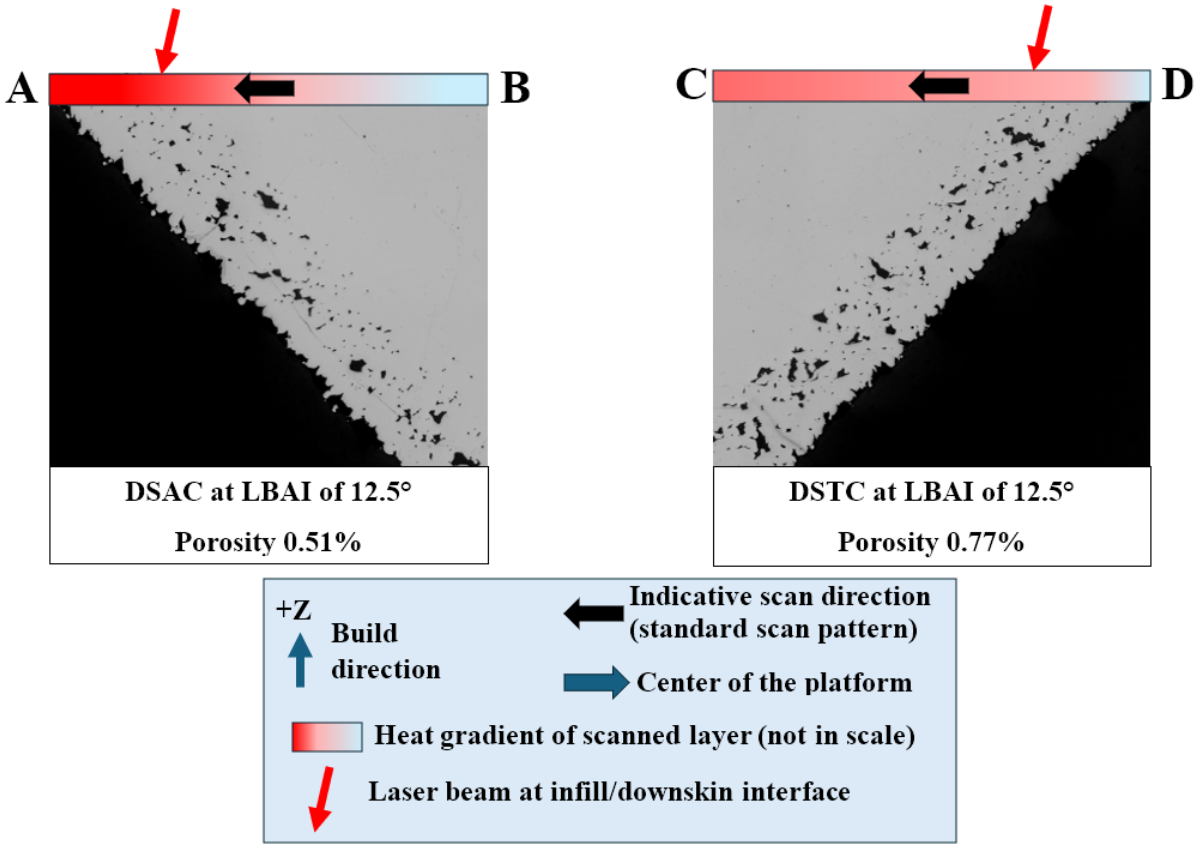


Figure 61 Proposed downskin LOF healing effect during re-melting. A is the end and B is the start of the scanned stripe for DSAC, while C is the end, and D is the start of the scanned layer for DSTC. Note: the scan direction is indicative as it is not actually aligned perfectly along the downskin due to the part orientation on the build platform and the rotation of stripes in consecutive layers.

As can be seen from Figure 61 A, it is anticipated that the heat builds up towards the end of the scanned stripe as the cumulative laser-material interaction time increases during the scanning of a layer. Heat accumulation at the end of the scanned stripe promotes re-melting at the downskin for DSAC and reduces the amount of LOF. The heat accumulation is also promoted at the downskin as the heat conduction is limited due to the inclined surface. The heat accumulation at the downskin of DSTC is not as high, as the downskin is located at the start of the scanned stripe (Figure 61 D) where the cumulative laser-material interaction time is lower. This might lead to less re-melting and LOF healing which could explain the difference between porosity percentage of DSAC and DSTC. It is also anticipated that the melt pool orientation might have an effect on the LOF healing. As can be seen from Figure 61, the laser beam is directed more towards the LOF in the downskin in DSAC part than in DSTC part. This might align the melt pool according to the laser beam direction, which enhances the healing effect as the melt pool reaches LOF in downskin of DSAC more efficiently. Sendino et al. [6] reported that the melt pool orientation was aligned along the

laser beam incidence direction in PBF-LB/M processed IN718, which supports the assumption of melt pool orientation. Further studies are needed in order to confirm this hypothesis about the LOF healing effect at downskin with different part orientations.

# 10 Conclusions

The aim of the thesis was to study the effect of *LBAI* on surface roughness and porosity of IN718 parts manufactured via PBF-LB/M. Research gap about comprehensive study of *LBAI* induced defect formation on inclined IN718 surfaces was identified. Literature review was conducted to familiarize with the optical components of PBF-LB/M system and the PBF-LB/M process parameters. It was revealed that due to the configuration of optical components in the commercial PBF-LB/M systems, the laser beam is directed on the powder bed at an angle in the build platform periphery. Inclination of laser beam can cause distortion of the beam spot which can result in loss of energy density. Additionally, the formation mechanisms of surface roughness and porosity were reviewed. It was concluded that surface roughness and porosity formation is a complex entity, which is affected by many variables, such as laser and scan parameters, part geometry and *LBAI*.

The experimental part was performed to capture the effect of *LBAI* on the laser beam and on the defect formation of AMed IN718. Two distinct print jobs were designed and manufactured to capture the effect of *LBAI* on surface roughness of various surface types and on the downskin porosity. Surface roughness was measured via optical profilometry, and porosity was analyzed from ground and polished sections of AMed samples via optical microscopy.

It was observed that the circular laser beam spot starts to elongate along the incidence direction of the tilted beam. Elongation of the beam spot was seen when the *LBAI* reached 6.3°, while the spot elongated up to 11% at *LBAI* of 8.8°. Additionally, increased distortion of laser beam-material interaction area was observed at the corner of the build platform.

Surface roughness study revealed that the downskin surfaces and vertical surfaces that are facing away from the center of the platform are prone to increased surface roughness when the *LBAI* is increased. It was anticipated that the increase in surface roughness is due to tilted laser beam promoting melt pool extending further to the loose powder. On the other hand, surface roughness of upskin and vertical surfaces facing towards the center of the platform is not affected by increased *LBAI*. Interestingly, the downskin surfaces facing towards the center of the platform have reduced surface roughness when *LBAI* is increased, as the surface is aligned more parallel with the laser beam. While the effect of *LBAI* on surface roughness was captured, there yet remained some variations in surface roughness in different corners of the

build platform due to other location dependent factors. It was anticipated that these variations might be due to different stripe directions in relation to the measured surfaces or due to different inert gas flow conditions across the build platform.

Concluding the porosity study, it was observed that increasing the *LBAI* beyond 6.6° caused more LOF in the downskin which was manufactured with lowered *VED*. The infill region, which was manufactured with higher *VED*, was practically porosity free with negligible amount of gas pores with all *LBAI*s and part orientations. Thus, it can be suspected that parameters that do not yield fully dense parts are more prone to *LBAI* induced LOF formation. Differences in porosity percentage were observed with different part orientations as the part that had downskin facing away from platform center (DSAC) had lower porosity percentage. It was anticipated that the heat accumulation is higher towards the end of the scanned stripe, which led to LOF healing via re-melting more efficiently in the DSAC part.

In its entirety, the thesis showed that *LBAI* has prominent impact on AMed IN718 surface roughness, while porosity was affected only with LOF sensitive parameters. The findings from the thesis do not solve the issue of increased *LBAI* as such, but rather act as groundwork for further process development. The proposed methodology for the *LBAI* induced surface roughness and porosity characterization could be used as a tool for benchmarking new process features, which aim to mitigate *LBAI* induced defects.

# 11 Further studies and future development

A few opportunities for further studies were identified during the experimental part of the thesis. The present study mainly focuses on 45° and 90° surfaces, hence the conclusions might not apply with different geometries, such as surfaces with well below 45° build angle. Thus, the research should be extended to geometries with reduced build angle to study how much *LBAI* affects the surface roughness. Additionally, the experiments were conducted with EOS M 290 system, where the maximum *LBAI* that is practically achievable is around 12.5°. Research could be extended to larger EOS M systems where more extreme *LBAI*s are possible.

Porosity study showed differences in porosity percentage for different part orientations. It was anticipated that it might be caused by LOF healing due to the heat accumulation towards the end of the scanned stripe. Further investigations are needed to validate if the hypothesis is correct. For example, test pieces with LOF sensitive parameters (lowered *VED*) could be manufactured and the local porosity across the stripe longitudinal direction could be characterized. Additionally, numerical simulations on the matter could be performed to obtain supplementary information.

Surface roughness study showed that there are platform location dependent variations with the same *LBAI*. Cause for *LBAI* independent variations in defect formation should be investigated in a separate in-depth study. Furthermore, porosity was studied from a single quadrant of the build platform. Thus, the porosity study should be similarly extended to other platform locations to see if there are similar variations in the porosity percentage.

The present study was conducted with a Gaussian beam which is the current industry standard for PBF-LB/M. Based on engineering guess, it is hypothesized that more even intensity profile could decrease the loss of energy density at the beam periphery when *LBAI* is increased. Further studies with different beam intensity profiles, such as donut or flat top profile, could be conducted to investigate if the *LBAI* induced porosity could be decreased.

# References


[1] A. Vafadar, F. Guzzomi, A. Rassau and K. Hayward, "Advances in Metal Additive Manufacturing: A Review of Common Processes, Industrial Applications, and Current Challenges," *Applied Sciences,* vol. 11, 2021.

[2] E. Fereiduni, A. Ghasemi and M. Elbestawi, "Selective Laser Melting of Aluminum and Titanium Matrix Composites: Recent Progress and Potential Applications in the Aerospace Industry," *Aerospace,* 2020.

[3] L. C. Zhang and H. Attar, "Selective Laser Melting of Titanium Alloys and Titanium Matrix Composites for Biomedical Applications: A Review," *Advanced Engineering Materials,* vol. 18, pp. 463-475, 2016.

[4] E. Bassoli, S. Defanti, E. Tognoli, N. Vincenzi and D. Esposti, "Design for Additive Manufacturing and for Machining in the Automotive Field.," *Appl. Sci.,* vol. 11, 2021.

[5] E. M. Sefene, "State-of-the-art of selective laser melting process: A comprehensive review," *Journal Of Manufacturing Systems,* vol. 63, pp. 250-274, 2022.

[6] S. Sendino, M. Gardon, F. Lartategui, S. Martinez and A. Lamikiz, "The Effect of the Laser Incidence Angle in the Surface Of L-PBF Processed Parts," *coatings,* vol. 10, 2020.

[7] L. Cao, J. Li, J. Hu, H. Liu, Y. Wu and Q. Zhou, "Optimization of surface roughness and dimensional accuracy in LPBF additive manufacturing," *Optics & Laser Technology,* vol. 142, 2021.

[8] C. Du, Y. Zhao, J. Jian, Q. Wang, H. Wang, N. Li and J. Sun, "Pore defects in Laser Powder Bed Fusion: Formation mechanism, control method, and perspectives.," *Journal of Alloys and Compounds,* vol. 944, 2023.

[9] J. P. Oliveira, A. LaLonde and J. Ma, "Processing parameters in laser powder bed fusion metal additive manufacturing," *Materials and Design,* vol. 193, 2020.

[10] S. Kleszczynski, A. Ladewig, K. Friedberger, J. Jacobsmühlen, D. Merhof and G. Witt, POSITION DEPENDENCY OF SURFACE ROUGHNESS IN PARTS FROM LASER BEAM MELTING SYSTEMS, 2015.

[11] Z. Chen, X. Wu, D. Tomus and C. Davies, "Surface roughness of Selective Laser Melted Ti-6Al-4V alloy components," *Additive Manufacturing,* vol. 21, pp. 91-103, 2018.

[12] A. Ladewig, G. Schlick, M. Fisser, V. Schulze and U. Glatzel, "Influence of the shielding gas flow on the removal of process by-products in the selective laser melting process," *Additive Manufacturing,* vol. 10, pp. 1-9, 2016.

[13] Z. Chen, X. Wu and C. H. Davies, "Process variation in Laser Powder Bed Fusion of Ti-6Al-4V," *Additive Manufacturing,* vol. 41, 2021.

[14] P. Fathi-Hafshejani, A. Soltani-Tehrani, N. Shamsaei and N. Mahjouri-Samani, "Laser incidence angle influence on energy density variations, surface roughness, and porosity of additively manufactured parts," *Additive Manufacturing,* vol. 50, 2022.

[15] E. Li, H. Shen, L. Wang, G. Wang and Z. Zhou, "Laser shape variation influence on melt pool dynamics and solidification," *Additive Manufacturign Letters,* 2023.

[16] R. M. Mahamood, Laser Metal Deposition Process of Metals, Alloys, and Composite Materials, Springer International Publishing, 2018.

[17] EOS, *EOS M 290 Operating instructions,* n.d..

[18] EOS, *EOS M 290 Training System Operation and Maintenance,* 2022.

[19] J. O. Milewski, Additive Manufacturing of Metals, vol. 258, Springer International Publishing AG, 2017.

[20] C. DeCusatis and C. J. S. DeCusatis, "Optical Fiber principles," in *Fiber optic essentials*, 2010, pp. 4-13.

[21] R. Paschotta, "RP Photonics Encyclopedia," [Online]. Available: https://www.rp-photonics.com/beam_collimators.html. [Accessed 10 04 2024].

[22] R. Paschotta, "RP Photonics Encyclopedia," [Online]. Available: https://www.rp-photonics.com/fiber_collimators.html. [Accessed 10 04 2024].

[23] R. Paschotta, "RP Photonics Encyclopedia," [Online]. Available: https://www.rp-photonics.com/beam_expanders.html. [Accessed 10 04 2024].

[24] N. D. Dejene and H. G. Lemu, "Current Status and Challenges of Powder Bed Fusion-Based Metal Additive Manufacturing: Literature Review," *metals,* vol. 13, 2023.

[25] Nikon SLM, "SLM®125," n.d.. [Online]. Available: https://www.slm-solutions.com/products-and-solutions/machines/slm-125/. [Accessed 24 04 2024].

[26] EOS, "EOS M290," n.d.. [Online]. Available: https://www.eos.info/en-us/metal-solutions/metal-printers/eos-m-290#key-features. [Accessed 24 04 2024].

[27] C. Ozga, "Unseen Possibilities of F-Theta Lenses," *Optik&Photonik,* vol. 13, pp. 48-51, 2018.

[28] Thorlabs, "F-Theta Scan Lenses," [Online]. Available: https://www.thorlabs.com/newgrouppage9.cfm?objectgroup_id=6430. [Accessed 24 04 2024].

[29] OFH, "The Role of F-theta Lenses in Laser Scanning," n.d.. [Online]. Available: https://www.opticsforhire.com/blog/intro-to-f-theta-lenses/. [Accessed 24 04 2024].

[30] Z. Y. Chua, I. H. Ahn and S. K. Moon, "Process Monitoring and Inspection Systems in Metal Additive Manufacturing: Status and Applications," *INTERNATIONAL JOURNAL OF PRECISION ENGINEERING AND MANUFACTURING-GREEN TECHNOLOGY,* vol. 4, pp. 235-245, 2017.

[31] S. Chowdhury, N. Yadaiah, C. Prakash, S. Ramakrishna, S. Dixit, L. R. Gupta and D. Buddhi, "Laser powder bed fusion: a state-of-the-art review of the technology, materials, properties & defects, and numerical modelling," *jmr&t,* vol. 20, pp. 2109-2172, 2022.

[32] F. Caiazzo, V. Alfieri and G. Casalino, "On the Relevance of Volumetric Energy Density in the Investigation of Inconel 718 Laser Powder Bed Fusion," *materials,* vol. 13, 2020.

[33] K. Moussaoui, W. Rubio, M. Mousseigne, T. Sultan and F. Rezai, "Effects of Selective Laser Melting additive manufacturing parameters of Inconel 718 on porosity, microstructure and mechanical properties," *Materials Science & Engineering A,* vol. 735, pp. 182-190, 2018.

[34] Z. Liu, Y. Yang, D. Wang, Z. Chen and W. Yan, "Correlation between the scan strategy, residing spatter distribution, and parts quality in laser powder bed fusion," *Materials & Design,* vol. 234, 2023.

[35] J. Reijonen, A. Revuelta, S. Metsä-Kortelainen and A. Salminen, "Effect of laser focal point position on porosity and melt pool geometry in laser powder bed fusion additive manufacturing," *Additive Manufacturing,* vol. 85, 2024.

[36] S. Patel, H. Chen, M. Vlasea and Y. Zou, "The influence of beam focus during laser powder bed fusion of a high reflectivity aluminium alloy — AlSi10Mg," *Additive Manufacturing,* vol. 59, 2022.

[37] M. Vänskä, F. Abt, R. Weber, A. Salminen and T. Graf, "Effects of welding parameters onto keyhole geometry for partial penetration laser welding," in *Lasers in Manufacturing Conference*, 2013.

[38] L. R. Goossens, Y. Kinds, J. P. Kruth and B. Hooreweder, "ON THE INFLUENCE OF THERMAL LENSING DURING SELECTIVE LASER MELTING," in *Solid Freeform Fabrication 2018: Proceedings of the 29th Annual International Solid Freeform Fabrication Symposium*, 2018.

[39] R. Paschotta, "Beam Quality," n.d.. [Online]. Available: https://www.rp-photonics.com/beam_quality.html. [Accessed 15 08 2024].

[40] R. Paschotta, "Beam Parameter Product," n.d.. [Online]. Available: https://www.rp-photonics.com/beam_parameter_product.html. [Accessed 15 08 2024].

[41] J. Grünewald, F. Gehringer, M. Schmöller and K. Wudy, "Influence of Ring-Shaped Beam Profiles on Process Stability and Productivity in Laser-Based Powder Bed Fusion of AISI 316L," *metals,* vol. 11, 2021.

[42] F. Galbusera, L. Caprio, B. Previtali and A. G. Demir, "Analytical modeling and characterization of ring beam profiles for high-power lasers used in industrial manufacturing," *Journal of Manufacturing Processes,* vol. 117, pp. 387-404, 2024.

[43] T. M. Wischeropp, H. Tarhini and C. Emmelmann, "Influence of laser beam profile on the selective laser melting process of AlSi10Mg," *Journal of Laser Applications,* vol. 32, 2020.

[44] A. A. Okunkova, P. Y. Peretyagin, P. A. Podrabinnik, I. V. Zhirnov and A. V. Gusarov, "Development of laser beam modulation assets for the process productivity improvement of selective laser melting," *Procedia IUTAM,* vol. 23, pp. 177-186, 2017.

[45] J. D. Perez-Ruiz, F. Galbusera, L. Caprio, B. Previtali, L. N. Lacalle, A. Lamikiz and A. G. Demir, "Laser beam shaping facilitates tailoring the mechanical properties of IN718 during powder bed fusion," *Journal of Materials Processing Tech.,* vol. 328, 2024.

[46] L. E. Loh, Z. H. Liu, D. Zhang, M. Mapar, S. L. Sing, C. K. Chua and W. Y. Yeong, "Selective Laser Melting of aluminium alloy using a uniformbeam profile," *Virtual and Physical Prototyping,* vol. 9, pp. 11-16, 2014.

[47] H. Jia, H. Sun, H. Wang, Y. Wu and H. Wang, "Scanning strategy in selective laser melting (SLM): a review," *The International Journal of Advanced Manufacturing Technology,* vol. 113, pp. 2413-2435, 2021.

[48] E. Duong, L. Masseling, C. Knaak, P. Dionne and M. Megahed, "Scan path resolved thermal modelling of LPBF," *Additive Manufacturing Letters,* vol. 3, 2022.

[49] U. S. Bertoli, A. J. Wolfer, M. J. Matthews, J. R. Delplanque and J. M. Schoenung, "On the limitations of Volumetric Energy Density as a design parameter for Selective Laser Melting," *Materials and Design,* vol. 113, pp. 331-340, 2017.

[50] Olympus, "Surface Roughness Measurement," n.d.. [Online]. Available: https://www.olympus-ims.com/en/metrology/surface-roughness-measurement-portal/?utm_source=bing&utm_medium=cpc&creative=&keyword=surface%20roughness%20definition&matchtype=e&network=o&device=c&campaignid=627057698&adgroupid=1296324654525953&msclkid=274bddc. [Accessed 14 08 2024].

[51] H. Zhou, H. Su, Y. Guo, Y. Liu, D. Zhao, P. Yang, Z. Shen, L. Xia and M. Guo, "Formation and Evolution of Surface Morphology in Overhang Structure of IN718 Superalloy Fabricated by Laser Powder Bed Fusion," *Acta Metallurgica Sinica,* vol. 36, pp. 1433-1453, 2023.

[52] S. Rott, A. Ladewig, K. Friedberger, J. Casper, M. Full and J. H. Schleifenbaum, "Surface roughness in laser powder bed fusion – Interdependency of surface orientation and laser incidence," *Additive Manufacturing,* vol. 36, 2020.

[53] Z. c. Oter, M. Coskun, Y. Akca, O. Surmen, M. S. Yilmaz, G. Ozer, G. Tarakci, H. M. Khan and E. Koc, "Support optimization for overhanging parts in direct metal laser sintering," *Optik,* vol. 181, pp. 575-581, 2019.

[54] A. Bhatt, Y. Huang, C. L. Leung, G. Soundarapandiyan, S. Marussi, S. Shah, R. C. Atwood, M. E. Fitzpatrick, M. K. Tiwari and P. D. Lee, "In situ characterisation of surface roughness and its amplification during multilayer single-track laser powder bed fusion additive manufacturing," *Additive Manufacturing,* vol. 77, 2023.

[55] S. Elder, "The Basics of Surface Finish," 6 1 2021. [Online]. Available: https://www.gdandtbasics.com/basics-of-surface-finish/. [Accessed 2 9 2024].

[56] V. Viale, J. Stavridis, A. Salmi, F. Bondioli and A. Saboori, "Optimisation of downskin parameters to produce metallic parts via laser powder bed fusion process: an overview," *The International Journal of Advanced Manufacturing Technology,* vol. 123, pp. 2159-2182, 2022.

[57] S. Patel and M. Vlasea, "Melting modes in laser powder bed fusion," *Materialia,* vol. 9, 2020.

[58] T. Reiber, J. Rüdesheim, M. Weigold, E. Abele, J. Musekamp and M. Oechsner, "Influence of contour scans on surface roughness and pore formation using Scalmalloy® manufactured by laser powder bed fusion (PBF-LB)," *Materialwiss. Werkstofftech,* vol. 52, pp. 468-481, 2021.

[59] G. Chen, S. Y. Zhao, P. Tan, J. Wang, C. S. Xiang and H. P. Tang, "A comparative study of Ti-6Al-4V powders for additive manufacturing by gas atomization, plasma rotating electrode process and plasma atomization," *Powder Technology,* vol. 333, pp. 38-46, 2018.

[60] S. Tammas-Williams, H. Zhao, F. Léonard, F. Derguti, I. Todd and P. B. Pragnell, "XCT analysis of the influence of melt strategies on defect population in Ti–6Al–4V components manufactured by Selective Electron Beam Melting," *Materials Characterization,* vol. 102, pp. 47-61, 2015.

[61] R. Cunningham, A. Nicolas, J. Madsen, E. Fodran, E. Anagnostou, M. D. Sangid and A. D. Rollet, "Analyzing the effects of powder and post-processing on porosity and properties of electron beam melted Ti-6Al-4V," *Materials Research Letters,* vol. 5, pp. 516-525, 2017.

[62] C. Weingarten, D. Buchbinder, N. Pirch, W. Meiners, K. Wissenbach and R. Poprawe, "Formation and reduction of hydrogen porosity during selective laser melting of AlSi10Mg," *Journal of Materials Processing Technology,* vol. 221, pp. 112-120, 2015.

[63] Y. Huang, T. G. Fleming, S. J. Clark, S. Marussi, K. Fezzaa, J. Thiyagalingam, C. L. A. Leung and P. D. Lee, "Keyhole fluctuation and pore formation mechanisms during laser powder bed fusion additive manufacturing," *NATURE COMMUNICATIONS,* vol. 13, 2022.

[64] C. Panwisawas, C. L. Qiu, Y. Sovani, J. W. Brooks, M. M. Atallah and H. C. Basoalto, "On the role of thermal fluid dynamics into the evolution of porosity during selective laser melting," *Scripta Materialia,* vol. 105, pp. 14-17, 2015.

[65] M. Xia, D. Gu, G. Yu, D. Dai, H. Chen and Q. Shi, "Porosity evolution and its thermodynamic mechanism of randomly packed powder-bed during selective laser melting of Inconel 718 alloy," *International Journal of Machine Tools & Manufacture,* vol. 116, pp. 96-106, 2017.

[66] L. Cao, "Mesoscopic-scale simulation of pore evolution during laser powder bed fusion process," *Computational Materials Science,* vol. 179, 2020.

[67] C. Schwerz, A. Raza, X. Lei, L. Nyborg, E. Hryha and H. Wirdelius, "In-situ detection of redeposited spatter and its influence on the formation of internal flaws in laser powder bed fusion," *Additive Manufacturing,* vol. 47, 2021.

[68] R. Esmaeilizadeh, U. Ali, A. Keshavarzkermani, Y. Mahmoodkhani, E. Marzbanrad and E. Toyserkani, "On the effect of spatter particles distribution on the quality of Hastelloy X parts made by laser powder-bed fusion additive manufacturing," *Journal of Manufacturing Processes,* vol. 37, pp. 11-20, 2019.

[69] M. Laleh, A. E. Hughes, S. Yang, J. Wang, J. Li, A. M. Glenn, W. Xu and M. Y. Tan, "A critical insight into lack-of-fusion pore structures in additively manufactured stainless steel," *Additive Manufacturing,* vol. 38, 2021.

[70] U. Ali, R. Esmaeilizadeh, F. Ahmed, D. Sarker, W. Muhammad, A. Keshavarzkermani, Y. Mahmoodkhani, E. Marzbanrad and E. Toyserkani, "Identification and characterization of spatter particles and their effect on surface roughness, density and mechanical response of 17-4 PH stainless steel laser powder-bed fusion parts," *Materials Science & Engineering A,* vol. 756, pp. 98-107, 2019.

[71] M. Amirjan and H. Sakiani, "Effect of scanning strategy and speed on the microstructure and mechanical properties of selective laser melted IN718 nickel-based superalloy," *The International Journal of Advanced Manufacturing Technology,* vol. 103, pp. 1769-1780, 2019.

[72] Y. Lu, S. Wu, Y. Gan, T. Huang, C. Yang, L. Junjie and J. Lin, "Study on the microstructure, mechanical property and residual stress of SLM Inconel-718 alloy manufactured by differing island scanning strategy," *Optics & Laser Technology,* vol. 75, pp. 197-206, 2015.

[73] Y. Tian, D. Tomus, P. Rometsch and X. Wu, "Influences of processing parameters on surface roughness of Hastelloy X produced by selective laser melting," *Additive Manufacturing,* vol. 13, pp. 103-112, 2017.

[74] Q. Li, X. Li, B. Dong, S. Shu, F. Qiu, L. Zhang and Z. Zhang, "Metallurgy and Solidifcation Microstructure Control of Fusion-Based Additive Manufacturing Fabricated Metallic Alloys: A Review," *Acta Metallurgica Sinica,* vol. 37, pp. 29-53, 2024.

[75] N. T. Aboulkhair, N. M. Everitt, I. Ashcroft and C. Tuck, "Reducing porosity in AlSi10Mg parts processed by selective laser melting," *Additive Manufacturing,* pp. 77-86, 2014.

[76] T. Bhardwaj and M. Shukla, "Effect of laser scanning strategies on texture, physical and mechanical properties of laser sintered maraging steel," *Materials Science & Engineering A,* vol. 734, pp. 102-109, 2018.

[77] I. Serrano-Munoz, A. Ulbricht, T. Fritsch, T. Mishurova, A. Kromm, M. Hofmann, R. C. Wimpory, A. Evans and G. Bruno, "Scanning Manufacturing Parameters Determining the Residual Stress State in LPBF IN718 Small Parts," *Advanced Engineering materials,* vol. 23, 2021.

[78] D. Dimitrov, T. H. Becker, I. Yadroitsev and G. Booysen, "ON THE IMPACT OF DIFFERENT SYSTEM STRATEGIES ON THE MATERIAL PERFORMANCE OF SELECTIVE LASER MELTING- MANUFACTURED TI6AL4V COMPONENTS," *South African Journal of Industrial Engineering,* vol. 27, pp. 184-191, 2016.

[79] J. Zhang, M. Zeißig, R. Dörfert, F. Jablonski, R. Kienzler, J. Schumacher, B. Clausen, P. Woizeschke and F. Vollertsen, "Influence of laser beam scanning pattern and polar angle on the fatigue behavior of additively manufactured specimens made of steel 316L," *Materials Science & Engineering A,* vol. 886, 2023.

[80] E. Yasa, J. Deckers and J. Kruth, "The investigation of the influence of laser re-melting on density, surface quality and microstructure of selective laser melting parts," *Rapid Prototyping Journal,* vol. 17, pp. 312-327, 2011.

[81] A. Marques, Â. Cunha, M. R. Silva, M. I. Osendi, F. S. Silva, Ó. Carvalho and F. Bartolomeu, "Inconel 718 produced by laser powder bed fusion: an overview of the influence of processing parameters on microstructural and mechanical properties," *The International Journal of Advanced Manufacturing Technology,* vol. 121, pp. 5651-5675, 2022.

[82] EOS, "EOS NickelAlloy IN718," n.d.. [Online]. Available: https://www.eos.info/en-us/metal-solutions/metal-materials/data-sheets/mds-eos-nickelalloy-in718. [Accessed 19 08 2024].

[83] D. Deng, R. L. Peng, H. Brodin and J. Moverare, "Microstructure and mechanical properties of Inconel 718 produced by selective laser melting: Sample orientation dependence and effects of post heat treatments," *Materials Science & Engineering A,* vol. 713, pp. 294-306, 2018.

[84] EOS, "EOS M 290," n.d.. [Online]. Available: https://www.eos.info/en-us/metal-solutions/metal-printers/eos-m-290#key-features. [Accessed 19 08 2024].

[85] PRIMES, "Manual," n.d.. [Online]. Available: https://www.primes.de/en/products/custom-solutions/focus-and-scanner-movement.html?file=files/userFiles/downloads/handbuecher-anleitungen%20EN/SFM_Rev.%2001%20EN%20-%2005_2021.pdf. [Accessed 19 08 2024].

[86] C. DeCusatis and C. J. S. DeCusatis., Fiber Optic Essentials. 1st edition., Amsterdam: Elsevier/Academic Press, 2006.

[87] Z. Zheng, B. Sun and L. Mao, "Effect of Scanning Strategy on the Manufacturing Quality and Performance of Printed 316L Stainless Steel Using SLM Process," *materials,* vol. 17, 2024.

[88] Y. Liu, J. Li, K. Xu, T. Cheng, D. Zhao, W. Li, Q. Teng and Q. Wei, "An optimized scanning strategy to mitigate excessive heat accumulation caused by short scanning lines in laser powder bed fusion process," *Additive Manufacturing,* vol. 60, 2022.

[89] R. Paschotta, "Scanning Lenses," [Online]. Available: https://www.rp-photonics.com/scanning_lenses.html. [Accessed 24 04 2024].

[90] U. Ali, Y. Mahmoodkhani, S. I. Shahabad, R. Esmaeilizadeh, F. Liravi, E. Sheydaeinan, K. Y. Huang, E. Marzbanrad, M. Vlasea and E. Toyserkani, "On the measurement of relative powder-bed compaction density in powder-bed additive manufacturing processes," *Materials and Design,* vol. 155, pp. 495-501, 2018.

[91] C. Li, Z. Y. Liu, X. Y. Fang and Y. B. Guo, "On the Simulation Scalability of Predicting Residual Stress and Distortion in Selective Laser Melting," *J. Manuf. Sci. Eng.,* vol. 140, 2018.

[92] R. Paschotta, "Laser Optics," n.d.. [Online]. Available: https://www.rp-photonics.com/laser_optics.html. [Accessed 24 08 2024].

[93] L. Parry, I. Ashcroft and R. Wildman, "Understanding the effect of laser scan strategy on residual stress in," *Additive Manufacturing,* vol. 12, pp. 1-15, 2016.

# Appendices

## Appendix 1 *LBAI* for different radial distances from center of the platform

*LBAI* can be calculated when the radial distance *r* of the beam spot from the center of the building platform is known.

**Example calculation of *LBAI* at *r* = 100 mm**

First, *o* is calculated according to equation 4

$$o = 100 \text{ mm} * \frac{43\ mm}{177\ mm} = 24.29 \ldots\ mm \quad (4)$$

Then, $r_o$ can be calculated with equation 5

$$r_o = 100\ mm - 24.29 \ldots\ mm = 75.70 \ldots mm \quad (5)$$

Then, *LBAI* can be calculated with equation 6

$$\theta = tan^{-1}\left(\frac{75.70 \ldots mm}{481{,}95\ mm}\right) \approx 8{,}9° \quad (6)$$

***LBAI*s for different laser beam characterization measurement points.**

The resulting *LBAI* of different measurement points can be calculated by using equations 4-6 when the radial distance *r* from the center of the platform is known. Radial distance from the center for measurement locations are calculated according to equation 7 based on Pythagorean theorem, where x is the x-coordinate of the measurement point and y is the y-coordinate of the measurement point.

$$r = \sqrt{x^2 + y^2} \quad (7)$$

Figure 62 illustrates *r* at measurement point 70/-70.

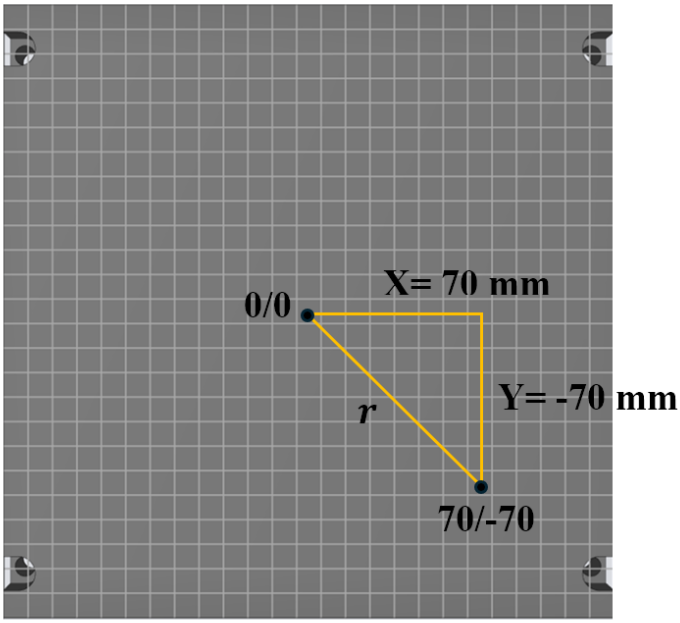


Figure 62 Illustration of *r* at measurement point 70/-70

Calculating *r* for measurement point 70/-70 mm according to equation 7

$$r = \sqrt{70^2\ mm + (-70)^2\ mm} \approx 99\ mm \quad (7)$$

*LBAI*s for different measurement locations are shown in Table 7.

Table 7 *LBAI* at different measurement points.

| **Measurement point** | **Radial distance from the center (r) (mm)** | ***LBAI* (°)** |
|---|---|---|
| **0/0** | 0 | 0 |
| **35/0 & -35/0** | 35 | 3.1 |
| **-70/0 & 70/0** | 70 | 6.3 |
| **-70/-70 & 70/-70** | 99 | 8.8 |
| **-120/-120** | 170 | 14.9 |

***LBAIs* for different test geometries arranged on the build platform.**

Test parts in surface roughness study and porosity study were arranged on the build platform with known radial distances from the center. Table 8 shows the *LBAI*s for different test part radial distances, which were calculated according to equations 4-6.

Table 8 *LBAI* for each radial distance from the center.

| **Radial distance from the center (*r*)** | ***LBAI*** |
|---|---|
| ***r1*= 141,5 mm** | 12.5° |
| ***r2*= 110 mm** | 9.8° |
| ***r3*= 73 mm** | 6.5° |
| ***r4*= 36 mm** | 3.2° |

## Appendix 2 Definition of build angle of Part C

Originally it was intended that surfaces in lower half of part C were always approximately parallel with the laser beam. This was done to study if the surface roughness could be enhanced by tilting the part when the *LBAI* is increased. Figure 63 illustrates the relation of *LBAI* and build angle when the laser beam is parallel with the part surface.

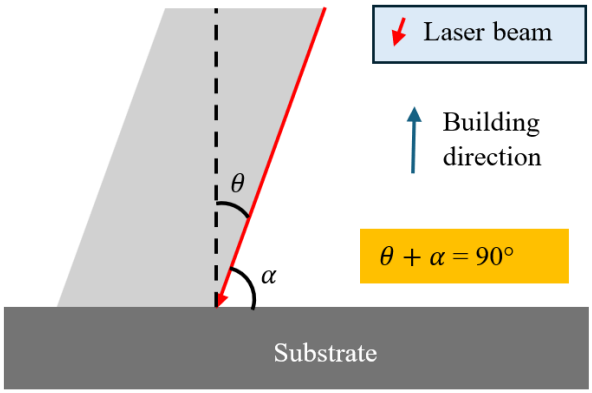


Figure 63 Relation between *LBAI* θ and build angle α when the laser beam is parallel with the surface

As Figure 63 reveals, the sum of *LBAI* and build angle should equal to 90° for the laser beam to be parallel with the surface. However, *LBAI* values were calculated incorrectly when the parts were designed, which led to faulty build angles in part C to facilitate parallel surface with the laser beam. The approximate deviation $d_e$ of the *LBAI* from being parallel with the surface can be calculated with equation 8, where $\theta$ is the *LBAI* and α is the build angle. The beam is parallel with the surface when $d_e$ is zero.

$$d_e = 90° - (\theta + \alpha) \quad (8)$$

The used build angles for part C and B with different radial distances is shown in Table 9 alongside with the approximate deviation $d_e$ of the *LBAI* from being parallel with the surface. As can be seen from Table 9, at each radial distance from the center the surface of lower half of part C has $d_e$ value closer to zero than Part B. Thus, it can be stated that surfaces of lower half of part C are more parallel with the laser beam than surfaces of Part B.

Table 9 Used build angles for part C with different radial distances and the deviation of the *LBAI* from the build angle.

| Part | Radial distance | $LBAI\ \theta$ | build angle α | $d_e$ |
|---|---|---|---|---|
| Part C (lower half) | r1 | 12.5° | 71° | 6.5° |
| | r2 | 9.8° | 75° | 5.2° |
| | r3 | 6.5° | 80° | 3.5° |
| | r4 | 3.2° | 85° | 1.8° |
| Part B | r1 | 12.5° | 90° | -12.5 |
| | r2 | 9.8° | 90° | -9.8° |
| | r3 | 6.5° | 90° | -6.5° |
| | r4 | 3.2° | 90° | -3.2° |

**Appendix 3 Micrographs of the porosity samples.**

| | *LBAI* 0° | *LBAI* 6.5° | *LBAI* 12.5° |
|---|---|---|---|
| **DSAC** | 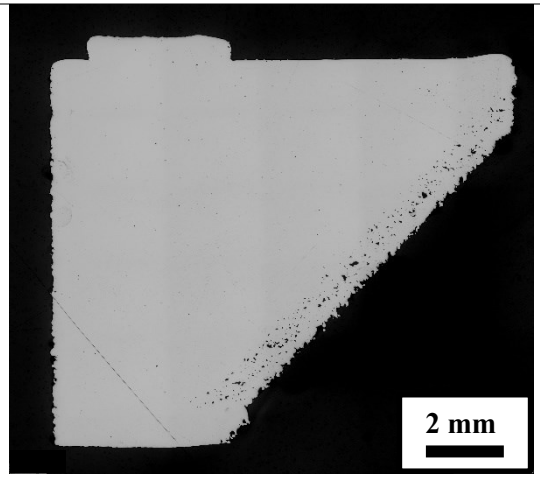  | 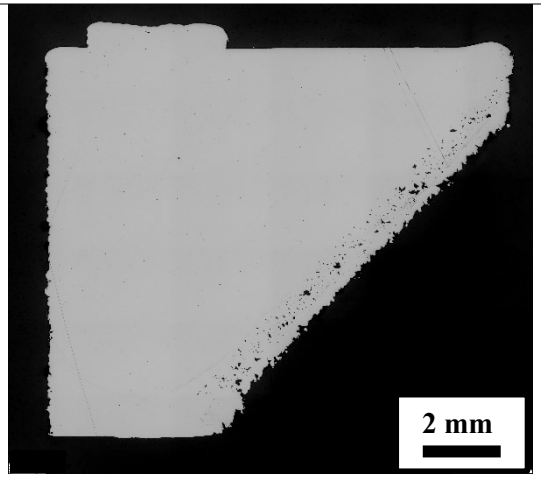  | 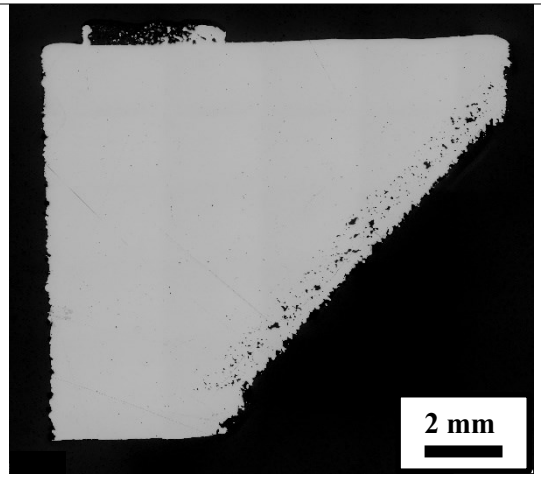  |
| **DSTC** | 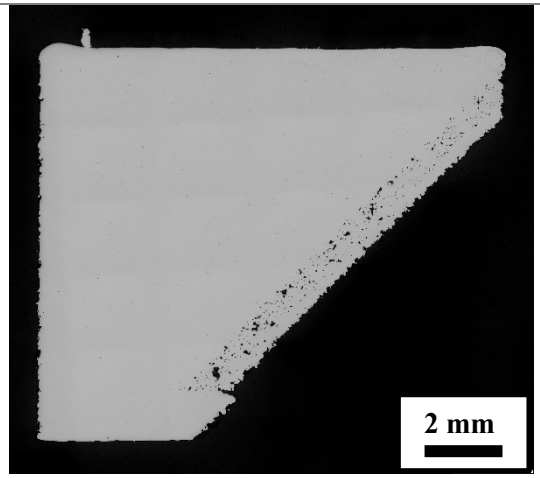  | 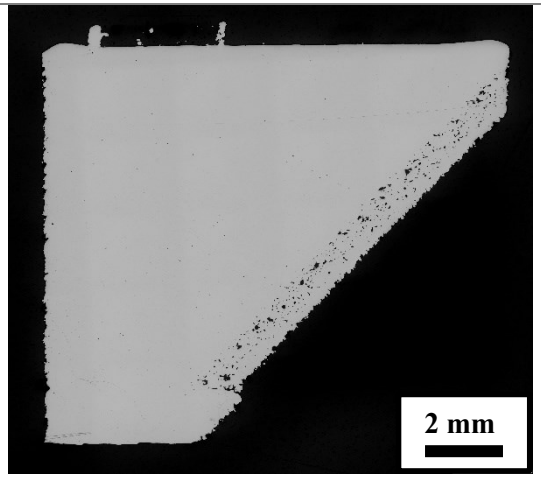  | 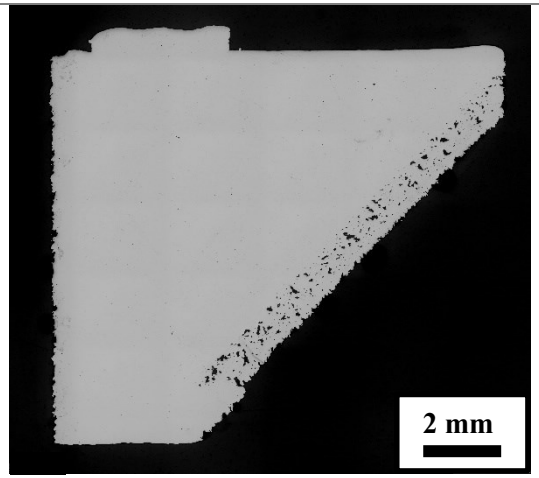  |